ASSESMENT OF THE PREDICTIVE CAPABILITY OF EULERIAN-EULERIAN MODELING APPROACH FOR THE SPOUTED BED THERMAL RECEIVERS

EULER-EULER MODELLEME YÖNTEMİNİN TAŞKIN YATAK ISIL ALICILARI İÇİN KESTİRİM YETENEĞİNİN DEĞERLENDİRİLMESİ

CANKUT ERKAYA

PROF. DR. MURAT KÖKSAL

Supervisor

Submitted to

Graduate School of Science and Engineering of Hacettepe University

as a Partial Fulfilment to the Requirements

for the Award of the Degree of Master of Science

in Mechanical Engineering.

2024

ABSTRACT

ASSESMENT OF THE PREDICTIVE CAPABILITY OF EULERIAN-EULERIAN MODELING APPROACH FOR THE SPOUTED BED THERMAL RECEIVERS

Cankut ERKAYA

Master of Science, Department of Mechanical Engineering

Supervisor: Prof. Dr. Murat KÖKSAL

August 2024, 117 pages

Directly irradiated fluidized/spouted particle receivers can potentially store thermal energy at higher temperatures than 1100 °C in concentrated solar power (CSP) applications. Therefore, these types of thermal receivers are good candidates for the next-generation CSPs. Furthermore, particles suggested for CSP applications such as carboHSP and olivine have high density (larger than 2500 kg/m^3) and for particles sizes of 1 mm or more, spouted beds are usually preferred over fluidized beds due their low bed pressure drop characteristics.

The number of thermal numerical studies on the spouted beds for CSP applications are limited in the literature. One commonly used modeling approach is the Eulerian-Eulerian approach (also known as TFM) where both solid phases is defined as a continuum similar to gas phase. Most TFM studies in the spouted literature investigates the gas-solid flow

dynamics whereas available thermal studies do not address the gas-solid flow dynamics in detail. Furthermore, TFM approach needs various constitutive equations and adjustment of hydrodynamic and thermal properties for which a comparative assessment is needed to develop reliable models. Therefore, the aim of this thesis is to investigate the prediction performance of TFM for the CSP thermal storage applications in spouted beds assessing the hydrodynamic and thermal performance simultaneously. The scope of the thesis is limited to discharge behaviour of the thermal storage system by convective cooling. The radiative heating has not been considered. In this context, there different data sets were selected (He *et al*. (1994a; 1994b), Patil *et al*. (2015) and Ozdemir (2024)) for validation. While He *et al*.'s (1994a; 1994b) data set is strictly for gas-solid flow dynamics, Patil *et al*. (2015) and Ozdemir (2024) provide thermal data sets for convective cooling simulating the discharge behaviour in CSP systems. For the simulations, ANSYS FLUENT was used and interphase heat transfer and different effective thermal conductivity models were implemented using user defined functions.

The results indicate that amongst the hydrodynamic TFM parameters the drag model and the restitution coefficient are the most critical ones from hydrodynamics perspective to obtain reasonably accurate solutions. On the thermal side, the gas-solid interphase heat transfer coefficient, the effective thermal conductivity of the solid phase, and the appropriate definition of the wall boundary conditions are essential for accurate modeling of the cooling or thermal energy discharge behavior of the bed. The correlation of Gunn (1978) for the interphase heat transfer coefficient result in particle Nusselt numbers (Nu_p) consistent with the measurements in the fluidized bed literature and the model of Zehner and Schlunder (1970) for the solids phase effective conductivity perform better than the kinetic theory approach. The energy balance and thermal mesh sensitivity are two important points which are often overlooked in the literature. Obtaining a mesh sensitive solution based on hydrodynamic parameters does not guarantee mesh sensitivity for thermal simulations. Thermal simulations require finer mesh sizes. Finally, comparison of the results with the Ozdemir's (2024) data set for the discharge behaviour of carboHSP particles indicate that the TFM can capture the general trends of the cooling behaviour for the first 100 s for which the simulations were run. The maximum temperature difference between the simulation and experimental results based on the data obtained from three locations in the bed is 7-8 °C and the cooling rates are reasonably similar.

Furthermore, TFM simulations provide some physical insight on the cooling behaviour of the CarboHSP particles.

Keywords: Spouted Bed Receiver, Concentrated Solar Power, CFD, Two-Fluid Model, Transient Cooling

ÖZET

EULER-EULER MODELLEME YÖNTEMİNİN TAŞKIN YATAK ISIL ALICILARI İÇİN KESTİRİM YETENEĞİNİN DEĞERLENDİRİLMESİ

Cankut ERKAYA

Yüksek Lisans, Makina Mühendisliği Bölümü

Tez Danışmanı: Prof. Dr. Murat KÖKSAL

Ağustos 2024, 117 sayfa

Konsantre güneş enerji (KGE) uygulamalarında, doğrudan ışıma ile ısınan akışkan/taşkın yataklı parçacık alıcılarının 1100 °C'den daha yüksek sıcaklıklarda termal enerjiyi depolayabilme potansiyelleri vardır. Bu nedenle, akışkan/taşkın parçacık alıcıları gelecek nesil KGE sistemlerine entegre edilebilecek en iyi alıcılar olarak göze çarpmaktadır. Ayrıca, KGE uygulamaları için önerilen carboHSP ve olivin gibi parçacıklar yüksek yoğunluğa (2500 kg/m³'ün üzerinde) ve 1 mm veya daha büyük parçacık boyutlarına sahip olduklarından, akışkan yataklar yerine daha az yatak basınç düşüş özelliğine sahip olan taşkın yataklarda kullanılmaları tercih edilmektedirler.

Literatürde KGE uygulamaları kapsamındaki taşkın yatakların sayısal termal modelleme çalışmaları sınırlı sayıda bulunmaktadır. Eulerian-Eulerian yaklaşımı, katı fazının gaz fazı gibi sürekli akışkana göre tanımlanabildiği, yaygın olarak kullanılan bir modelleme

tekniğidir. Aynı zamanda çok fazlı akış (ÇFA) modeli olarak da bilinir. Literatüründeki çoğu taşkın yataklar için yapılan ÇFA model çalışmaları gaz-katı akış dinamiklerini incelemelerine karşın mevcut termal çalışmalarında gaz-katı akış dinamiklerinden kaynaklı etkileri detaylı bir şekilde ele almamışlardır. Ayrıca, ÇFA yaklaşımı ile güvenilir modeller geliştirmek için çeşitli tamamlayıcı denklemler kullanılarak hidrodinamik ve termal özelliklerin karşılaştırılmasına ve değerlendirilmesine ihtiyaç duyulmaktadır. Bu yüzden, hidrodinamik ve termal performanslarının eşzamanlı değerlendirerek ÇFA'nın tahmin yeteneğinin araştırılması bu tezin amacını oluşturmaktadır. Termal enerji depolama sisteminin yalnızca taşınımla soğutma ile enerjisini boşaltma davranışlarının araştırılması bu tezin kapsamını oluşturmaktadır. Radyasyon ile ısıtma tez kapsamına alınmamıştır. Bu kapsamda, farklı veri setleri (He vd. (1994a; 1994b), Patil vd. (2015) ve Özdemir (2024)) doğrulama için seçilmiştir. He vd.'nin (1994a; 1994b) veri seti sadece gaz-katı akış dinamikleri içindir. Patil vd. (2015) ve Özdemir 2024 ise KGE sistemlerindeki termal enerjiyi taşınımla soğutma davranışını modellemeye yardımcı olacak termal veri setleri sunmaktadırlar. Modelleme çalışmalarında ANSYS FLUENT yazılımı kullanılmıştır. Fazlar arası ısı transferi ile farklı etkin termal iletkenlik modelleri kullanıcı tanımlı fonksiyonlar yardımıyla yazılımın içine eklenmiştir.

Sonuçlara göre hidrodinamik ÇFA parametrelerinden sürüklenme modelinin ve parçacıların elastik çarpışma oranının, kabul edilebilir derecede doğru çözümler elde etmek için hidrodinamik açıdan en kritik parametreler olduğu gösterilmiştir. Diğer taraftan, fazlar arası ısı transfer katsayısının, katı fazın etkin termal iletkenliğinin ve duvar sınır koşullarının uygun tanımlanması ile yatağın soğutma veya termal enerjiyi boşaltma davranışlarının doğru modellenmesi için gerekli olduğu termal taraftaki sonuçlara göre gösterilmiştir. Gunn (1978) tarafından önerilen fazlar arası ısı transfer katsayı korelasyonuna göre parçacığa ait Nusselt sayısı (Nu_p) akışkan yatak literatüründeki ölçümlerle tutarlılık sağlarken, Zehner ve Schlunder (1970) modelinin katı fazın etkin termal iletkenliği, kinetik teori yaklaşımından daha iyi performans gösterdiği bulunmuştur. Modelleme çalışmaları kapsamında enerji dengesinin incelenmesi ve modele ait ağ hassasiyet çalışmalarının yapılması literatürde genellikle göz ardı edilen iki önemli konudur. Hidrodinamik parametreler kapsamında elde edilen bir ağ hassasiyet çözümü, termal analiz çalışmaları için ağ hassasiyetini garanti etmemektedir. Termal modelleme çalışmaları, daha küçük ağ boyutlarında yapılması gerekebilir. Son olarak, carboHSP parçacıklarının termal enerjilerini boşaltma davranışlarına ait modelleme

çalışma sonuçları, Özdemir (2024) veri seti ile karşılaştırılmıştır. ÇFA yaklaşımı ile gerçekleştirilen 100 saniyelik modelleme çalışması sonuçlarına göre soğutma davranışlarının deneyin sonuçlarına ait genel eğilimleri yakalayabildiği görülmüştür. Yataktaki üç yerden elde edilen verilere dayanarak modelleme ile deneysel sonuçlar arasındaki maksimum sıcaklık farkının 7-8 °C olduğu gözlenmiştir. Diğer taraftan ise soğutma hızları oldukça benzerlik göstermektedir. Ayrıca, ÇFA modelleme çalışmaları kapsamında carboHSP parçacıklarının soğutma davranışı hakkında bazı fiziksel öngörüler sağlanmıştır.

Anahtar kelimeler: Taşkın yataklı alıcılar, Konsantre güneş enerjisi, Hesaplamalı akışkanlar dinamiği, Çok Fazlı Akış, Zamana bağlı soğuma

ACKNOWLEDGMENTS

I would like to thank my advisor, Prof. Dr. Murat Köksal, for his support of the thesis. He helped me prepare my thesis with his valuable comments and guidance.

I would also like to thank Assoc. Prof. Dr. Özgür Ekici, Prof. Dr. Görkem Külah, Prof. Dr. Nimeti Döner, and Assist. Prof. Dr. Ramin Barzegar, who were on my thesis committee. Their comments made my thesis clearer and more comprehensible.

I would also like to thank Arif Eren Özdemir for sharing his experimental results.

I also thank Meteksan Savunma Sanayii A.Ş. for supporting graduate education.

This work was carried out with the financial support of the Scientific and Technological Research Council of Turkey (Project No.: MAG 122M514).

CONTENTS

LIST OF FIGURES

LIST OF TABLES

NOMENCLATURE

Symbols

A_i Specific interfacial exchange area (1/m)

C_D Drag coefficient (-)

c_p Specific heat (J/kgK)

d_s Particle diameter (m)

e_{ss} Restitution coefficient for particle-particle collisions (-)

g_0 Radial distribution function (-)

H Specific enthalpy (J/kg)

I Internal energy (J/Kg)

K_{gs} Gas-solid momentum exchange coefficient (kg/ $\mathrm{m}^3 s$)

p Pressure (Pa)

q Heat flux (W/ m^2)

S Source term (W)

$\vec{\mathrm{u}}$ Velocity vector(m/s)

U_{ms} Minimum spouting velocity (m/s)

U_{mf} Minimum fluidization velocity (m/s)

U Superficial velocity (m/s)

$v_{r,s}$ Terminal velocity correlation of solid phase (-)

T Temperature (K)

Re_s Solid Reynolds number (-)

Nu_p Particle Nusselt number (-)

Pr	Prandl number (-)

Constants

g	Gravity constant (m/s^2)
π	Pi number

Greek Symbols

α	Volumetric interphase heat-transfer coefficient (W/m^{3}K)
α_{qp}	The q^{th} and p^{th} phases heat-transfer coefficient (W/m^{2}K)
ε	Volume fraction
$\kappa_{f,o}$	True fluid thermal conductivity (W/m K)
$\kappa_{s,o}$	True solid thermal conductivity (W/m K)
κ_b	Bulk thermal conductivity (W/m K)
$\kappa_{b,f}$	Fluid phase bulk thermal conductivity (W/m K)
$\kappa_{b,s}$	Solid phase bulk thermal conductivity (W/m K)
$\kappa_{eff,f}$	Fluid phase effective thermal conductivity (W/m K)
$\kappa_{eff,s}$	Solid phase thermal conductivity (W/m K)
ρ	Density (kg/ m^3)
θ	Granular temperature (m^2/ s^2)
γ	Dissipation rate resulting from inelastic particle-particle collisions (Kg/m s^3)
φ	Wall specularity coefficient (m^2/ s^2)
$\overline{\overline{\tau}}$	Shear stress tensor (N/m^2)
λ	Bulk viscosity (Kg/m s)
μ	Shear viscosity (Kg/m s)

Subscripts

b	Bulk
f	Fluid phase
g	Gas phase
s	Solid phase
w	Wall

Abbreviations

CSP	Concentrated solar power
CFD	Computational fluid dynamics
DEM	Discreet Element Method
HTM	Heat transfer medium
LFR	Linear Fresnel reflector
TES	Thermal energy storage
TFM	Two fluid model
PV	Photovoltaic
PDC	Power dish collector
PTC	Parabolic trough collector
SPT	Solar power tower
KTGF	Kinetic theory of granular flow

1. INTRODUCTION

The adverse effects of energy crises and climate change on the earth are increasing year by year due to the use of fossil energy. Therefore, the transition to renewable energy has become even more critical. The leading renewable energy types are wind and solar. However, renewable energy technologies of wind and solar can only be supported to generate intermittent electrical energy. So, the renewable energy technologies must be more flexible and more stable. They must be able to provide electrical energy at night or in unfavourable weather [1].

Two main methods convert solar energy to electrical energy. The first method is photovoltaic (PV) technology. It directly produces electricity. However, PV technology cannot provide energy at night or in cloudy weather.

Another method is concentrated solar power (CSP). This technology produces electrical energy indirectly. Firstly, in CSP systems, solar radiation energy converts to thermal energy. After that, the thermal energy is either delivered to a heat engine to produce electrical energy or kept in a thermal energy storage (TES) used in the future. Annual solar-electric efficiency of CSPs with the TES is in the range of 10-20% [1]. Meanwhile, commercial PV models have efficiencies ranging from 17% to 24% [2]. However, CSPs with the TES can stabilize fluctuations in power supply due to night or under cloudy weather. Furthermore, large-scale electricity generation is more feasible for CSPs integrated with TES.

On the other hand, the average cost of electricity of CSPs in 2022 is 0.118 $/kWhe, which is significantly higher than the costs of onshore wind power (0.033 $/kWhe) and photovoltaics (0.049 $/kWhe) [1, 3]. Hence, the installed capacities of wind and photovoltaic technologies include most of the total capacity. As a result of increasing investment in CSP, technologies can improve the cost of installation and operation efficiency to reduce the average electricity costs.

1.1. Concentrated Solar Power (CSP)

A CSP system generally contains three subsystems: heliostat mirrors, a receiver unit, and a heat engine. Heliostat mirrors help to collect solar energy. The primary duty of the mirrors is to track and reflect incident sunlight to a receiver unit. Additionally, solar energy converts to thermal energy in the receiver unit. A working fluid or a heat transfer medium (HTM) is used inside the receiver unit to collect heat energy. The working fluid, such as steam, can be used directly in a heat engine to produce electrical energy. Besides, the HTM can be transferred to a thermal energy storage, also known as TES. The receiver unit is also connected with TES which stores thermal energy on behalf of later use. Meanwhile, a heat exchanger carries the thermal energy to a different working fluid used in the heat engine to produce electrical energy for later usage [4]. Figure 1.1 represents a schematic image of a CSP's subsystems.

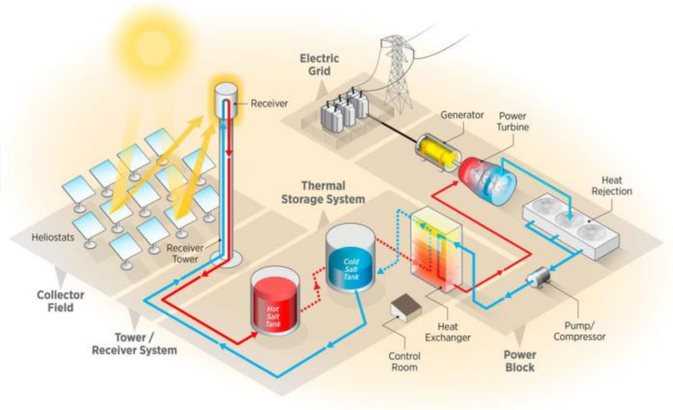

Figure 1.1 A schematic image of a CSP's subsystems [5].

1.1.1. Historical overview of CSP

According to the collector types for the heliostat mirrors, CSPs are classified into four main categories. The first collector type is linear fresnel reflectors (LFR). The second and third mirror types are parabolic trough collectors (PTC), and solar power towers (SPT). Furthermore, the final collector type is power dish collector (PDC). All collector types are demonstrated in Figure 1.2.

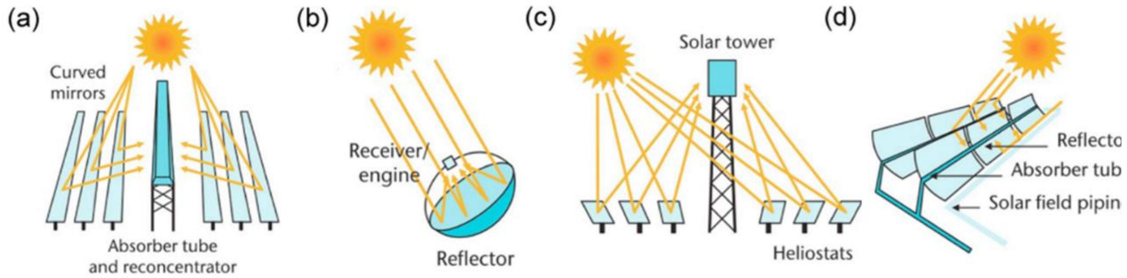

Figure 1.2 Images of CSP's collector types: a) Linear Fresnel (LFC) b) Parabolic dish (PDC), c) Solar power towers (SPT), and d) Linear fresnel reflectors (LFR) [6].

In 1978, a SPT system integrated into a central receiver was built as a test facility at Sandia National Laboratories. Different receiver technologies and materials were tested there. Moreover, in the 1980s, two SPT systems were built at Daggett in the USA. One of the systems used direct steams, and the other used molten salt as an HTM. They had a capacity of 10MWe. Their central receivers are the first pilot-scale. Additionally, a parabolic trough collector system was constructed in 1980 in southern California. This facility is still in operation today and is also the first commercial plant for the PTC system. 2007–2009, two SPT systems were constructed near Seville in Spain. These systems are the first commercial plants that use saturated steam as an HTM. Also, they have a capacity of 10 MWe and 20 MWe, respectively. Near Seville, another SPT system was constructed in 2011. It has been the first commercial facility that uses molten salt. It is also known as the Gemasolar Project. Meanwhile, in 2010, the first commercial power dish collector, with a capacity of 1.5 MWe, was built in Arizona. Besides being competitive with fossil fuels, the U.S. Energy Department started the SunShot program in 2011. They aimed to reduce costs of electricity under $0.06/kWh with unsubsidized. Hence, three SPT systems were built at Ivanpah in the USA in 2014. They have a total capacity of 390 MWe. They also use superheated steam as an HTM. In 2015, another SPT system was built at Tonopah in the USA in 2015. It uses a molten salt as an HTM and has a capacity of 110 MWe. A timeline of significant events related to CSP is given in Figure 1.3 [7].

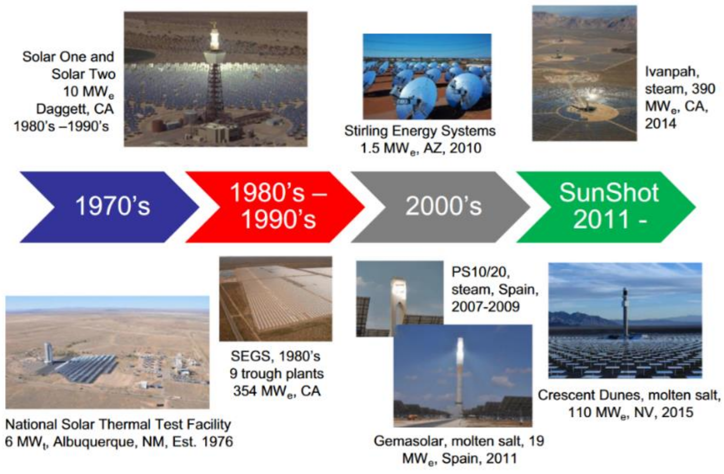

Figure 1.3 Timeline of key events in CSP [7].

1.1.2. Current and Future Reviews of the CSP Technologies

The CSP technologies have three generations based on thermodynamic cycle types and their cycle efficiency (Figure 1.4). The Rankine cycle is used in the first generation of CSPs and is operated with around 28-38% cycle efficiency. Moreover, they have around 240-440 °C of the peak cycle temperature. In addition, the first generations are usually operated with LFR, SPT, and PTC collector types. Their early design is not integrated with the TES. Hence, they cannot be used at night or in bad weather conditions. Annual solar-electric efficiency is in the range of 9-16% because they have low cycle efficiency.

The second generation of CSPs also utilizes the Rankine cycle. They are operated with around 38-44% cycle efficiency because their highest cycle temperature is around 475-555 °C. In addition, the second generations are usually operated with LFR, SPT, and PTC collector types. Furthermore, newly built facilities are integrated with the TES. Therefore, the plants can operate without daytime and sunny conditions. Annual solar-electric efficiency is in the range of 10-20%.

Moreover, some second-generation CSPs collect solar energy with the PDC and work with direct steam. They also operate with the Stirling cycle. Their cycle efficiency is around 38%. However, CSP with the PDS plants were installed with small capacity because the heat engines of the systems have reliability problems such as gas leaks. Also, the TES is not integrated with these plants.

First-generation CSP systems currently include 80% of the total installed capacity. Conversely, the second generation of CSP with SPT plants will plan to build in the future, including 61% of the capacity.

The cycle efficiency of CSP must be improved for lower operation and installation costs. Hence, third-generation CSPs have started to develop to enhance solar-electric efficiency. Their peak cycle temperature is targeted to rise above 700 °C to increase their cycle efficiency, which is estimated to be higher than 50%. Recently, they are only in the research and development phase. Besides, the USA, EU, and China support them financially and technologically. Therefore, heliostat, solar receiver, and thermal energy storage, the subsystems of next-generation CSPs, must be designed better and require optimization study to obtain above 700 °C for the peak cycle temperature.

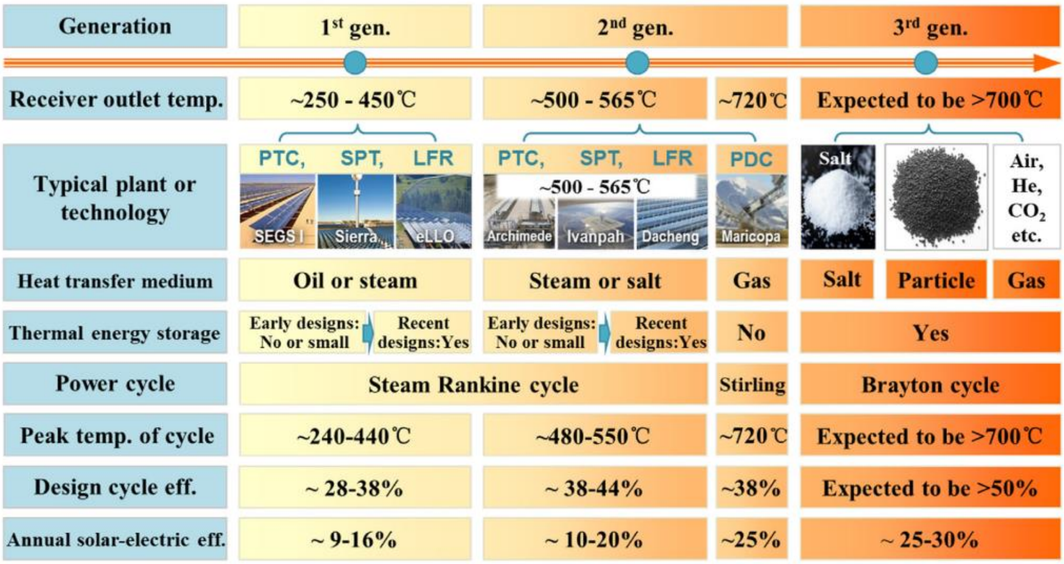

Figure 1.4 Different generations of CSP technologies [1].

Molten salt, gas, and particles are suggested as HTM in the solar receiver of the third-generation CSPs. However, they are under development because their material compatibility and efficiency reduction under high temperatures still need to be solved. Therefore, material selection and receiver design are essential to solving these problems.

Molten salt, a key component in current CSP with TES plants, holds significant potential as a candidate for future CSPs. However, when operated above 700 °C, significant challenges can be observed, such as material decomposition and receiver corrosion, which cause reduced efficiency of the plants.

Another candidate can be a gas receiver. It operates at a higher 700 °C. However, gases have poor thermal properties, which cause a low heat transfer rate in the receiver. Hence, they have low receiver efficiency.

Another essential receiver type is the particle receiver. It can operate safely at temperatures above 700 °C. Different particle materials, such as silica sand, silicon carbide, and ceramic particles, can be utilized in the particle receiver to absorb solar energy [5]. The properties of the particles should be more stable, abundant, inexpensive, and have high solar absorptance, which is necessary to increase efficiency and reduce operating costs. Table 1.1 demonstrates material properties of suggested solid particles for the next generation CSPs.

Table 1.1 Material properties that are suggested solid particles on behalf of the next generation CSPs [8].

Material	**Specific Heat (J/kgK)**	**a (Absorptance)**	**e (Emissivity)**	**Thermal Conductivity (W/mK)**	**Melting Point (°C)**	**Density (g/cm^3)**
Silica sand (SiO_2)	742-1175	0.44-0.66	0.59-0.9	1.14	1200-1400	2.1-2.65
Silicon Carbide (SiC)	663-677	N/A	0.83-0.96	90-110	2150-2250	3-3.2
Alumina (Al_2O_3)	790-800	0.1-0.25	0.3-0.5	20-25.6	2050	3.94-3.96
Olivine	700-900	N/A	N/A	8–10	1870-1950	2.8-3.37
CarboHSP	1275	0.934	0.843	2	N/A	3.56
CarboProp	1175	0.89-0.93	0.75-0.80	N/A	N/A	1.56
Accucast ID	1175	0.906	0.754	0.7	N/A	N/A

1.1.3. Particle Receiver in CSP

Solar energy in the particle receivers can heat the particles directly or indirectly. Therefore, they are divided into two subcategories according to heating techniques: direct receivers and indirect receivers. In the indirect receivers, solar radiation directly irradiates opaque tubes filled with particles. The irradiated tubes get heat. Then, their heat energy transfers to the particles indirectly.

Furthermore, the indirect receivers protect the mass of the particles when transferring or heating because their design stores the particles in enclosures. Hence, the particle loss problem is not observed in the indirect receivers. However, they can decrease receiver efficiency because the existing tube wall increases resistance of heat transfer to the particles.

On the contrary, in the direct receivers, solar radiation directly irradiates the particles. Therefore, the direct particle receivers operate at much higher temperatures and have better receiver efficiency [9]. Table 1.2 presents the summary of particle receivers. Furthermore, Figure 1.5 demonstrates schematic views of different particle receivers.

Table 1.2 Overview of designs of particle receivers [9].

	Design Type	**Reached Highest Temperature/ Thermal Efficiency**
Direct Particle Receivers	Free-Falling	>700 °C / ~50%-70%
	Obstructed	>700 °C / ~50%-70%
	Rotating Kiln/ Centrifugal	900 °C / 75%
	Fluidized Bed	>1000 °C / ~20%-40%
Indirect Particle Receivers	Particle flow by gravity-driven in enclosures	N/A
	Particle flow that is fluidized in tubes	>1000 °C / Thermal efficiency is not reported

One of the direct particle receivers is a free-falling receiver. The receiver thermal efficiency is below 70%. An obstructed receiver can be used as another direct particle receiver. They have small barriers to improve efficiency because the particles spend more time in the receiver. Therefore, they are exposed to more solar energy, which enhances absorption. The outlet temperature of the free-falling and obstructed particle receiver can reach over 700 °C. The other two direct receivers are rotating kilns and fluidized bed receivers. The rotating kiln receiver can reach over 900 °C. On the other hand, a fluidized bed receiver can reach over 1000 °C [9].

The fluidized bed receiver can reach higher peak temperatures than other particle receivers, gas receivers, and molten-salt receivers because the fluidized bed provides unique properties, including excellent heat transfer, adequate particle mixing, and flexible reactor design and operation [10]. However, they use gases to mix the particles and generally operate openly. So, the particle can be spilled out of the receiver. It causes a particle loss problem, which results in increased heat loss and operating costs.

In addition, the fluidized particle receiver can be installed on the ground using beam-down concentrate technology, which focuses solar radiation downward by a secondary mirror. As a result, a fluidized bed receiver integrated into a beam-down CSP can be built at a lower investment cost [11].

Direct Particle Receivers

Free-Falling [12]	Obstructed [8]	Rotating Kiln [9]	Fluidized Bed [13]
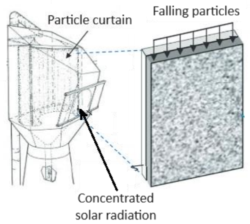	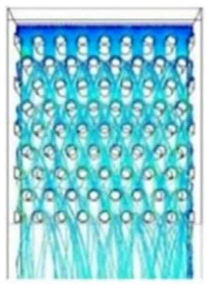	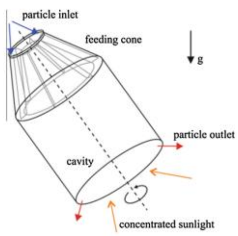	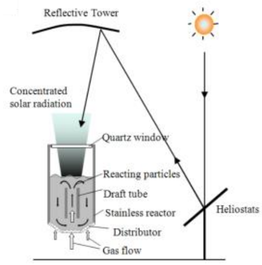

Indirect particle Receivers

Fluidized flow in tubes [4]	Gravity-driven flow in enclosures [9]
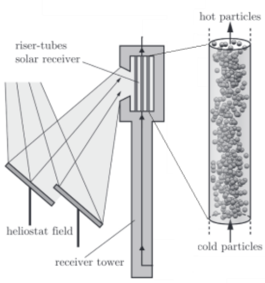	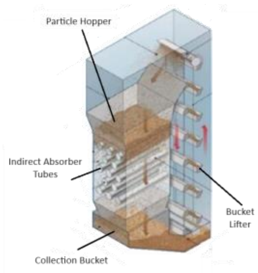

Figure 1.5 Schematic views of different particle receivers.

In summary, numerous novel technologies are suggested to decrease the installation and operation costs of the next-generation CSPs. Significantly, the fluidized particle receivers can reach peak temperatures higher than 1000 °C. On the other hand, none of the other technologies can reach 1000 °C. So, the fluidized particle receivers are better candidates than others as novel receivers for the next-generation CSPs. However, they are limited to lab- and pilot-scales. Therefore, they must be researched more to scale up applications that are essential to compete with other renewable energy technologies.

1.2. Fluidized and Spouted Beds

A fluidized bed is usually a cylindrical vessel filled with solid particles. The bottom and top sides of the vessel are open to the outside. The bottom side usually has a perforated flat plate or multiple orifices to prevent solid particles from falling. A gas phase enters vertically from the bottom and exits from the top. The vertical motion of the gas phase helps to fluidize the particles that are moving randomly in the vessel. Therefore, the fluidized beds have unique solid mixing characteristics. Many industries can use them as combustors, mixers, coaters, or dryers. The bubble and emulsion phases are two main fluidized bed regions [14]. Figure 1.6 demonstrates these regions.

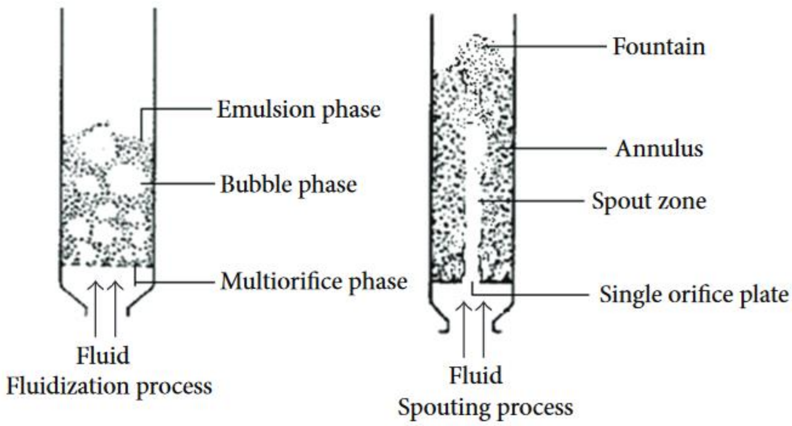

Figure 1.6 Fluidized and spouted bed's various regions [15].

On the other hand, the fluidized beds have operation limitations. They cannot fluidize coarse and heavy particles, especially. Therefore, spouted beds, which were modified from fluidized beds, were developed to handle coarse and heavy particles [16].

A spouted bed, usually like a fluidized bed, is a cylindrical vessel filled with solid particles. However, unlike the fluidized beds, the gas phase enters vertically like a jet from a single orifice at the bottom center of the vessel. This jet vertically creates a hollowed central cylinder in the bed. Moreover, the cylinder boundary is surrounded by the particles in the bed. The gas moves along and transfers the particles to the upward movement in the hollowed cylinder, and the particles exit vertically at the center of the upper bed; then, they slowly fall downward around the bed wall onto the bed's top surface. The particles move downward at the outer of the hollowed cylinder and enter upward movement again in the base of the hollowed cylinder. Consequently, in the spouted bed, the particles have a systematic circulation movement.

Figure 1.7 shows three main regions of a spouted bed. The first region where the particles vertically transfer in the middle of the cylinder is called the spout region. Moreover, the second region is the fountain region where the particles exit from the upper bed surface and fall again on the same surface. Meanwhile, the final region is the annulus region where the motion of the particles is downward from the outer spout region. Furthermore, the dilute phase is seen not only in the spout region but also in the fountain region. Otherwise, the denser phase is found in the annulus region.

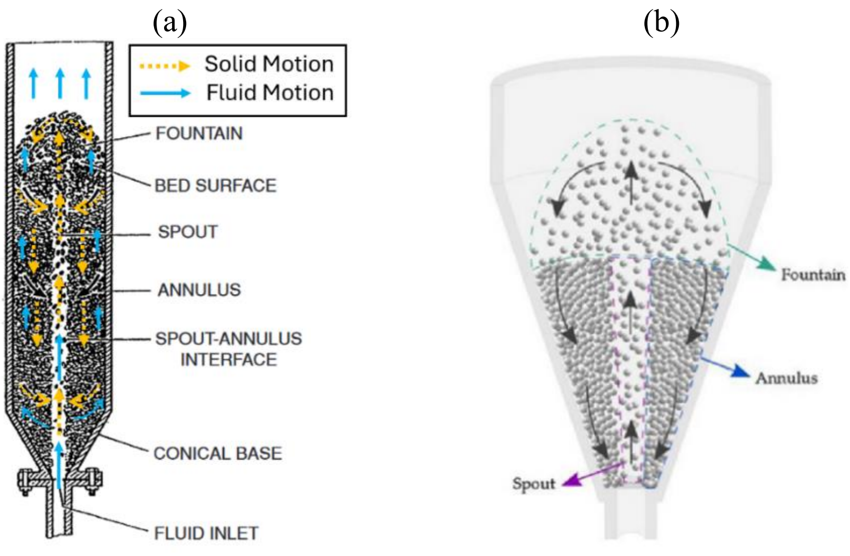

Figure 1.7 Schematic diagrams belonging to the spouted bed with a) conical–cylindrical, and b) conical shape [17].

The geometric shape of the base of spouted beds usually has a conical–cylindrical or conical shape. They are located like a reverse conical, so a dead zone does not occur in the bed, and all particles can be effectively involved in the movement. Figure 1.7 presents schematic diagrams belonging to the spouted bed with a conical–cylindrical and conical shape.

1.2.1. Differences Between Fluidized and Spouted beds

The superficial minimum fluidization velocity is at which fluidization is initiated. It is shown with U_{mf} as the symbol. It is also independent of bed height. In contrast, an external spout with a stable form begins when the superficial minimum spouting velocity is exceeded, shown with U_{ms} as the symbol. It is also dependent on bed height, unlike the fluidized beds. Both velocities are an important property of particles and fluidizing fluid. Moreover, there are many methods to measure the minimum fluidization and spouting velocities. Most commonly, the pressure drop technique is utilized to acquire the velocities.

The fluidized bed is in the packed bed position at the beginning of the pressure drop method. After that, gas starts to enter from the inlet with a slow velocity. Its velocity slowly increases until the bed is fluidized. Furthermore, the velocity of the inlet gas is related to the volumetric flow ratio is calculated from the area of the inlet. It can be also described as the superficial velocity, U. Simultaneously, the pressure drop rises until the velocity achieves the minimum fluidization velocity. After exceeding U_{mf}, the pressure drop becomes stable at almost a constant value. As indicated in Figure 1.8, fluidization initiates at the intersection between the increased and stabilized pressure lines [18].

Fluidized beds have different flow regimes, which depend only on the various superficial velocities. Each regime has its own hydrodynamics and thermal characteristics. Increasing the superficial velocity, fluidized beds are observed different flow regimes. Firstly, fixed beds, and delayed bubbling regimes are observed. When the superficial velocity continues to increase bubbling, slugging, and turbulent regimes, known as dense fluidization, are observed. Finally, fast fluidization, and pneumatic conveying regimes are observed, respectively. Figure 1.9 shows various flow regimes.

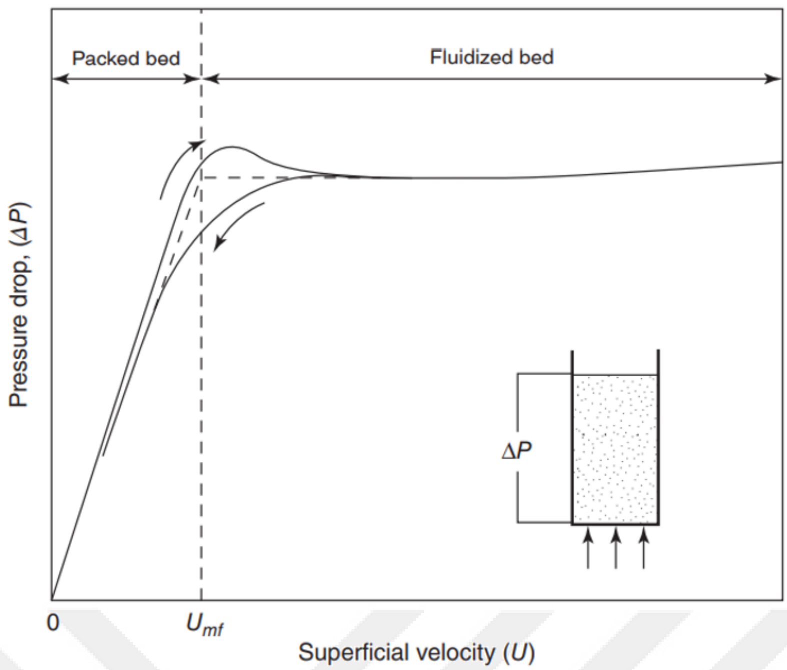

Figure 1.8 Graphical representation for the minimum fluidization velocity [18].

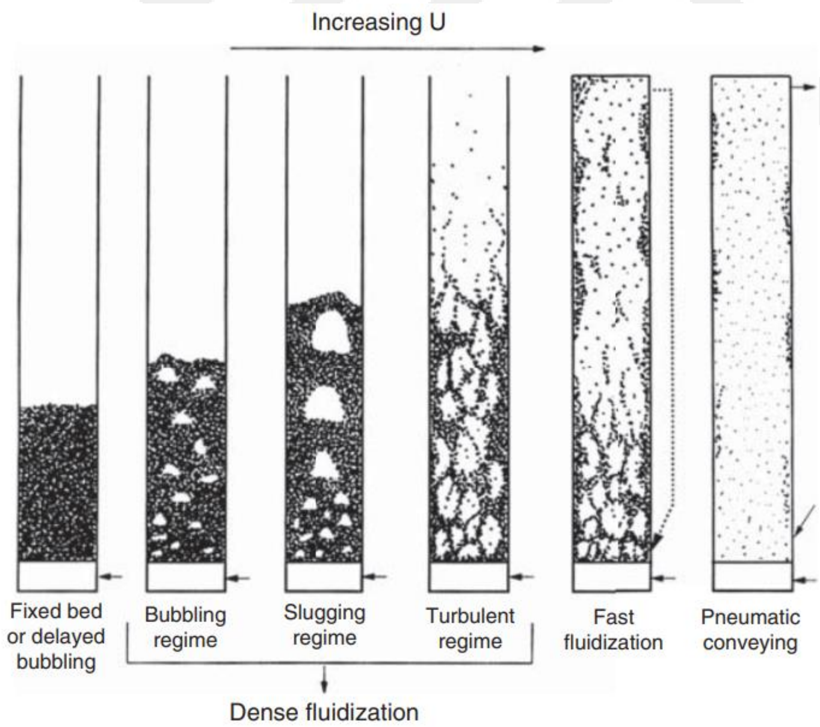

Figure 1.9 Gas–solid fluidization systems with various flow regimes [18].

Moreover, the pressure drop method can also be used in spouted beds to define minimum spouting velocity. On the contrary, different bed heights affect the minimum spouting velocity. Besides, unlike the fluidized bed, the spouted bed's pressure drop behavior can be observed differently. When the inlet velocity increases slowly, the development of the internal spout initiates and slowly extends upward to the bed surface. Simultaneously, the pressure drop increases until the external spout occurs from the bed surface. After forming the external spout, the pressure drop suddenly decreases from the maximum values and gets stabilized. After the spout is fully developed, the superficial velocity is decreased slowly until the collapse of the external spout. As a result, U_{ms} is defined as the location where the collapse occurs. Figure 1.10 identifies how to obtain the minimum spouting velocity [18].

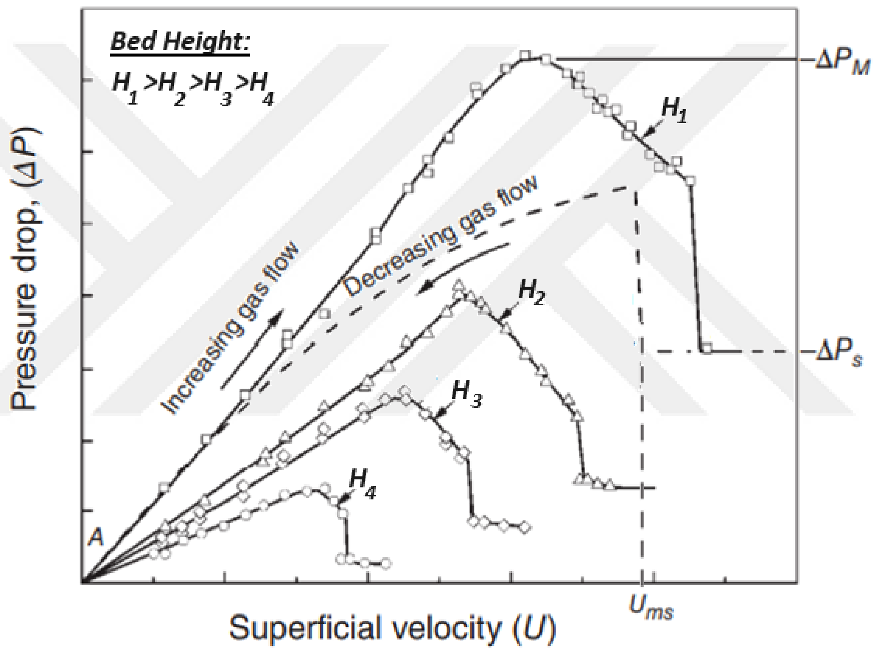

Figure 1.10 Graphical identification for the minimum spouting velocity [18].

Conversely, spouted beds have different flow regimes, which depend not only on the various superficial velocities but also on the various bed depths. Spout characteristic is observed only within a particular range of bed depths and velocities. Out of this range, the spouted bed can change to bubbling, slugging flow, or unstable spouting regimes, which can lose the characteristic cyclic movement of the solids. Figure 1.11 demonstrates various flow regimes of the conical-cylindrical spouted bed.

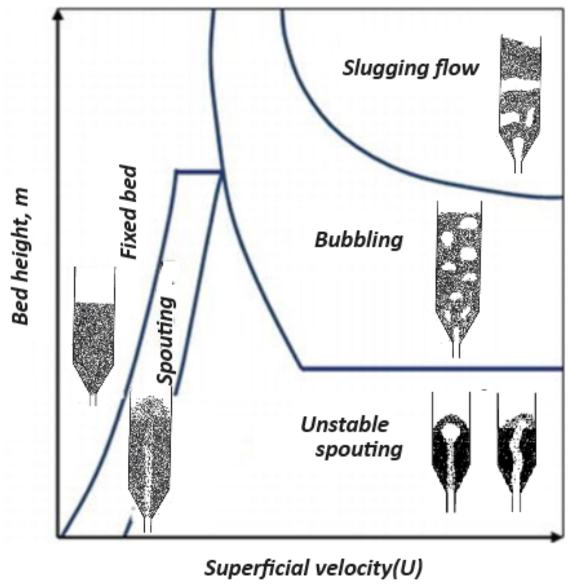

Figure 1.11 Various flow regimes for the spouted beds with conical–cylindrical shape [19].

Conical spouted beds turn to a dilute (or jet) spouting regime when operating with high gas velocity. As well as they keep the characteristic cyclic movement for the particles. Figure 1.12 indicates the translation of the dilute spouting regime.

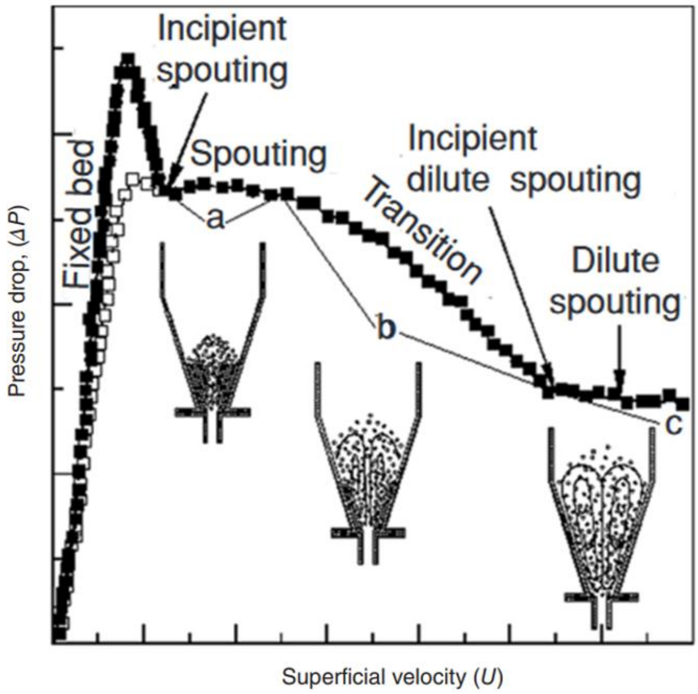

Figure 1.12 Various flow regimes in the conical spouted bed [16].

Geldart focused on the characteristics of the particles that make them fluidized. So, he proposed four groups for gas fluidization and analyzed them under room temperature and atmospheric pressure. The first group is categorized as Group C, which consists of cohesive or very fine powders. This group is dominated by interparticle cohesion. Therefore, normal fluidization is extremely hard. The second group is categorized as Group A. A notable effect between the particles can be observed in interparticle forces, but they are not dominant. Besides, at low gas velocities, these particles can be fluidized easily. Materials of Group A have low particle density (<~ 1.4 g/cm^3). Furthermore, they exist as small mean particle size. Additionally, Group B is categorized as the third group. Fluidization quality is generally good but not as high as for Group A. Interparticle forces have a negligible effect. Materials of Group B usually exhibit a mean particle size ranging from 40 μm to 500 μm. Moreover, material with particle density between 1.4 g/cm^3 to 4 g/cm^3 belongs to Group B. The final group is categorized as Group D, which is observed to be coarser than other groups. Coarse materials can be fluidized, but not as easily or smoothly as in Groups A and B. They are usually handled in spouted beds. Materials of Group D can be large diameter (>~500 μm) and dense (>~ 2.5 g/cm^3). All groups are categorized by density and mean particle diameter in the same dimensional plot, as shown in Figure 1.13 [14, 18].

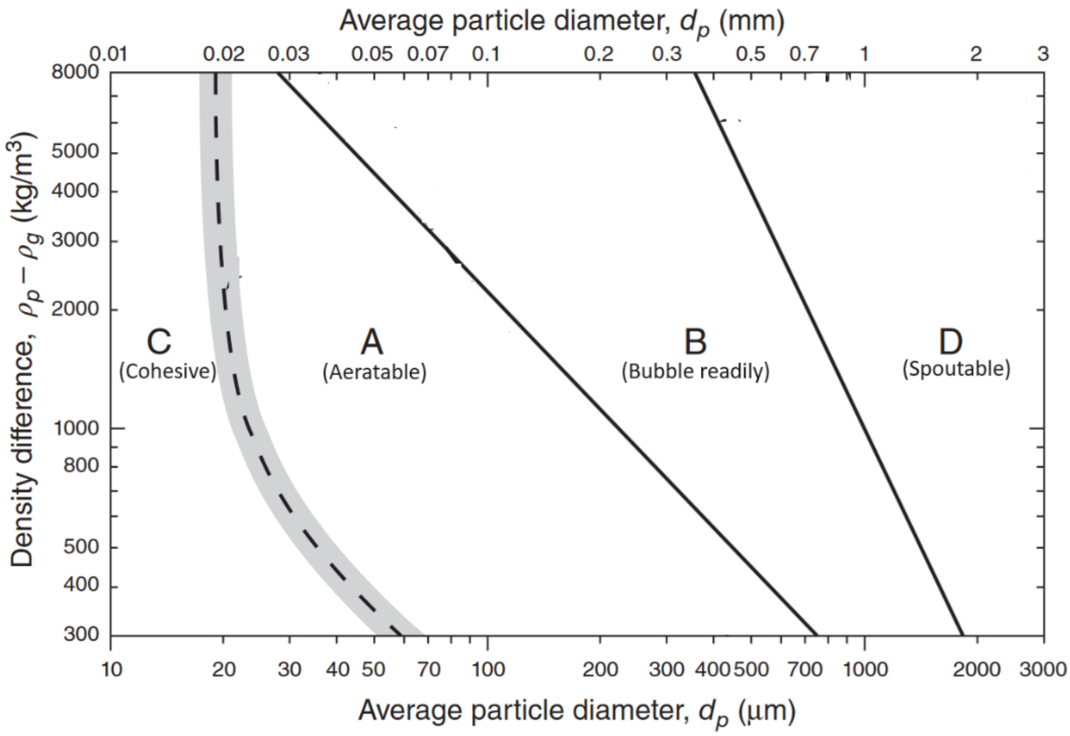

Figure 1.13 Geldart classification of particles [18].

1.2.2. Modeling Approaches of Fluidized and Spouted Beds

Spouted and fluidized beds can be numerically modeled using computational fluid dynamics (CFD). Generally, two main computational techniques are available for modeling gas-solid flow dynamics. The Two-Fluid Model (TFM) is the first technique. TFM is alternatively termed the Eulerian-Eulerian approach. Another modeling technique is the CFD-Discreet Element Method (DEM), also defined as the Eulerian-Lagrangian approach. Figure 1.14 demonstrates schematic views of the TFM method and CFD-DEM approach.

The solid and gas phases are presumed to be a continuum flow in the modelling frame of Eulerian-Eulerian. Hence, interpenetrating continua is mathematically defined in gas and solid phases. Additionally, each phase maintains its own volume without occupying the other. Therefore, each phase's mass, momentum, and energy conservation equations have similar structures with additional interphase energy and momentum transfer terms. Besides, particle–gas and particle-particle interactions must be described in additional constitutive equations because the continuum flow is also defined for the solid phase.

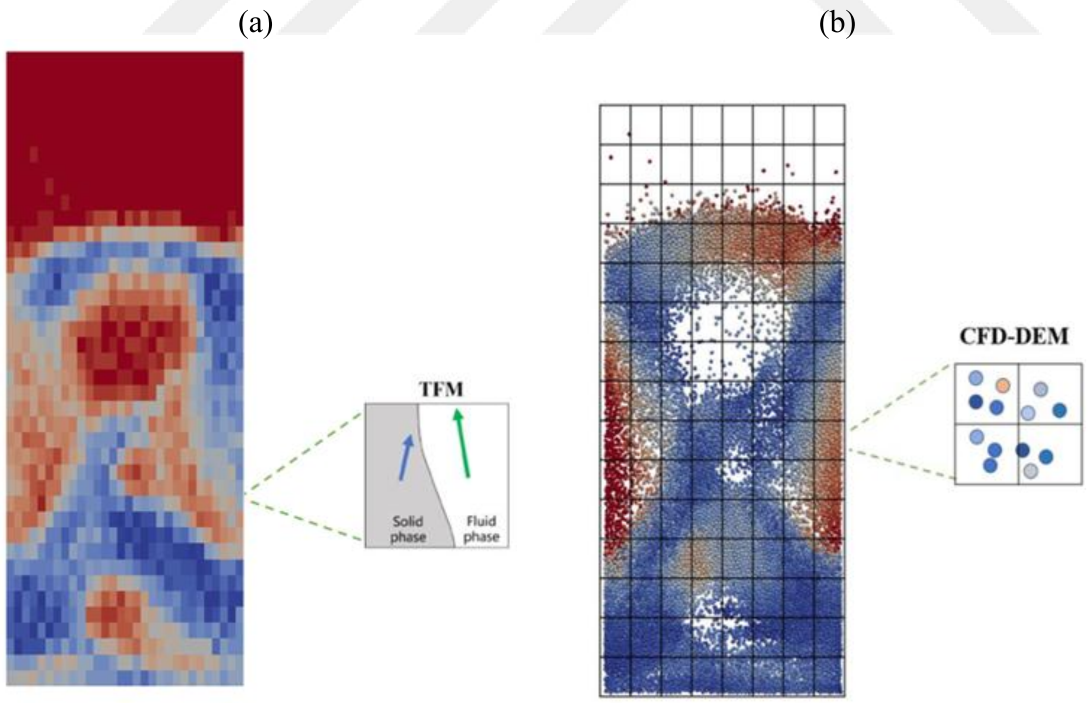

Figure 1.14 Representative views of a) TFM method, and b) CFD-DEM approach [17].

On the other hand, the gas phase is solved in the Eulerian framework in the Eulerian-Lagrangian method because of defining as a continuum. In contrast, the solid phase is defined as separate particles in the fluid domain. Their dynamic characteristics are separately examined in the Lagrangian framework. Additionally, they are allowed to be tracked individually. Therefore, no additional constitutive equations are required. Furthermore, CFD-DEM offers to simulate gas-solid flow dynamics more realistically. Computationally demanding in CFD-DEM applications is required much more than TFM applications, especially when large particle numbers are added to the simulation.

The Eulerian-Eulerian approach, with defined well-constitutive equations, can accurately predict gas-solids behavior in the beds. One of the constitutive equations is the drag model, which plays an essential role in interacting with other phases. Furthermore, other constitutive equations, which depend on solid-solid interactions and solid frictional stresses, also significantly affect the prediction of the solid flow regime. Therefore, the constitutive equations and drag models are enough to validate the beds accurately.

On the contrary, unlike the Eulerian-Lagrangian approach, it cannot track the particle individually. However, it demands lower computational costs. Hence, numerical studies using the Eulerian-Eulerian approach can be enough to get fast results and conceptually understand gas-solid flow dynamics. Because of these reasons, this thesis is conducted with simulation models using the Eulerian-Eulerian approach.

1.3. Literature Review

As mentioned before, the particle receivers in CSPs can store thermal energy at higher temperatures. The fluidized particle receivers can store thermal energy at temperatures above 1000 °C. On the contrary, none of the other novel technologies can reach 1000 °C. So, the fluidized particle receivers are better candidates than others for the next-generation CSPs. However, solid particles recommended for the next generation of CSPs typically have coarse sizes and higher densities. According to Geldart's classification, they are in Group D, making them easier to be handled in spouted beds. Hence, a literature survey was conducted to determine that spouted beds could be alternative technologies to fluidized beds due to their gas-solid flow behavior for CSP thermal receiver applications.

Many researchers have examined fluidized particle receivers for thermal storage in CSP with beam-down systems. Kodama *et al.* [13] examined temperature distributions of a fluidized particle receiver that was directly irradiated using a 30-kW_{th} big sun simulator. They also carried out another test for a similar fluidized bed receiver in a CSP unit. Besides, its capacity was 100 kW_{th} [20]. They reached up to 1200 °C in the laboratory scale bed. Furthermore, Tregambi *et al.* [21] examined temperature distributions of a fluidized and a fixed bed particle receiver, which was directly irradiated with a 4kW_{el} Xe lamp. They measured 600 °C and 1600 °C as the maximum local temperatures for the fixed and fluidized beds, respectively. Díaz-Heras *et al.* [22] conducted experiments in two different test setups, spout-fluid and conical spouted beds. They heated the setups directly irradiated by a 4kW_{el} Xe lamp. They showed that the particles have lower temperatures in the spouted bed. Furthermore, they mentioned that the spouted bed consumes less than 52% of gas than the spout-fluid beds**.** However, they did not investigate hydrodynamics in detail. They only measured bed height and gas flow velocity. Their study is the only study for spouted beds that have experimentally examined a directly irradiated as a thermal energy storage unit. Another study by Díaz-Heras *et al.* [23] examined thermodynamically comparing the spouted and the bubbling beds. They have shown that thermal efficiency is similar in both technologies. On the other hand, the spouted bed is found to reach at a higher temperature; however, it takes longer to reach it.

Furthermore, a few studies exist that the spouted bed has been examined directly or indirectly irradiated by solar radiation for gasification applications. Boujjat *et al*. [24] and Ma *et al*. [25] numerically and experimentally investigated spouted bed reactors irradiated by solar energy for biomass gasification. Moreover, at the CNRS-PROMES laboratory, a conical spouted bed reactor was developed for biomass gasification [26, 27]. Additionally, a spouted bed used wood biomass for continuous solar gasification. This spouted bed had a capacity of 1.5 kW_{th} and was heated by direct irradiation [24, 26, 28, 29]. The temperature of the spouted bed experimentally reached around 1200-1300 °C using different inert particle bed materials (such as silicon carbide, alumina, olivine, and sand).

In summary, spouted bed receivers have the potential to reach higher temperatures than 1000 °C, like fluidized bed receivers. Spouted beds can also fluidize denser and larger particles with less energy. On the other hand, solid particles, suggested for the next generation CSPs, generally have coarse sizes and higher density. They are classified in Group D, according to Geldart. Hence, they are treated more easily in spouted beds. As a result, the spouted bed receivers have the potential to be used in the CSP plants. However, commercially spouted bed receivers have not been built yet. They exist only on a lab scale. Furthermore, no literature study has been found to investigate thermal performances in detail. Figure 1.15 gives schematic views of a spouted bed heated by direct irradiation.

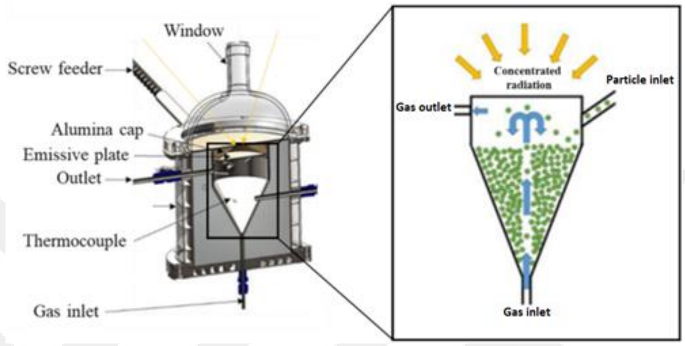

Figure 1.15 Schematic views of a directly irradiated spouted bed receiver [24].

1.3.1. Fluidized and Spouted Beds TFM Simulations

Numerical studies using TFM can be sufficient to get fast results and conceptually understand gas-solid flow dynamics and thermal performances of spouted bed receivers. Table 1.3 presents the summary of numerical studies using two-fluid model in fluidized and spouted bed beds for CSP applications. As can be seen from the table, there are only two studies in spouted beds investigating directly irradiated spouted bed receivers, but they are for gasification applications [24, 29]. The spouted and fluidized bed studies use different radiation models. Two studies have selected P1 approximation as the radiation model [4, 30]. Besides, two studies have selected the discrete ordinates models as the radiation model [24, 29]. One study selected the Rosseland approximation [31], and another selected the Monte Carlo method [32]. However, none of the literature studies investigated the effects of gas-solid flow dynamics and factors affecting the thermal performance in detail. Furthermore, before getting into the complexity of the incoming radiation, not only the distribution of thermal energy in the bed but also the gas-to-solid heat transfer caused by the incoming spouting/fluidizing air and the bed material need to be understood. There are some specific thermal studies –experimental and numerical– that aim to serve this purpose, and they are presented in the next section.

Table 1.3 Overview of numerical research using two-fluid models in fluidized and spouted beds for CSP applications.

References	Fluidize Technology	Application	Irradiated Heat Source	Simulation Model/ Software	Radiation Model
Baud et al. [32]	Fluidized bed	Thermal Storage	Directly	TFM/ Fluent 12	Monte Carlo
Matsubara et al. [33]	Fluidized bed	Thermal Storage	Directly	TFM/ Fluent	N/A
Marti et al. [4]	Upward moving fluidized dense suspension	Thermal Storage	Indirectly	TFM/ OpenFOAM 2.3	P1 approximation
Beniot et al. [31]	Upward moving fluidized dense suspension	Thermal Storage	Indirectly	TFM/ NEPTUNE CFD	Rosseland
Shen et al. [34]	Fluidized bed	Thermal Storage	Directly	TFM/ Fluent 18.1	Ray-Tracking
Jiang et al. [30]	Fluidized bed	Thermal Storage	Indirectly	TFM/ Fluent 15	P1 approximation
Boujjat et al. [24] *Bellouard et al.* [29]	Conical spouted bed	Gasification	Directly	TFM/ Fluent 18.0/19.1	The Discrete Ordinates

1.3.2. Transient Cooling of Fluidized and Spouted Beds

The numerical studies using irradiated heat sources did not provide detailed information on the transient state of thermal energy in the bed. Only limited number of studies have finished in the literature for this purpose. Using a thermal camera, Tsuji *et al.* [35] examined transient temperature distribution in a 2D spouted bed for 7s. Brown [36] also used a thermal camera to examine transient temperature distribution in a 2D spouted bed for 60s. On the hydrodynamics side, he measured only the fountain height and pressure drop with different inlet velocities. Fattahi *et al.* [37] and Hosseini *et al.* [38] carried two-fluid model studies that used Brown's study for validation. Additionally, Patil *et al.* [39] numerically and experimentally investigated the different particle sizes and inlet velocities for transient temperature distribution in a fluidized bed. Their study contains very detailed experimental data for temperature distribution of the transient cooling process of a hot fluidized bed which is the typical discharge process in a thermal receiver. Many CFD-DEM numerical studies used their study for validation.

1.4. Aims and Scope of the Thesis

Spouted bed receivers present opportunities to be utilized as thermal receivers in CSPs. The experimental studies regarding laboratory scale spouted beds have been gaining attention with the results of these studies being published in the open literature. On the other hand, the number of numerical modelling studies in the literature are still very limited. One of the commonly used modelling approaches is the Eulerian-Eulerian method (also known as two-fluid approach) where, similar to the gas phase, the particles are presumed to be a continuum with the closure relations derived from the kinetic theory of granular flow. Most of the modelling studies using two-fluid model are concentrated on either gas-solid flow dynamics or thermal aspects using a single experimental data set (either from literature or in-house) for comparison or validation. A more comprehensive approach is required to investigate the performance of this modeling approach for spouted beds in the CSP application. Furthermore, it is necessary to research solid-gas flow dynamics and in detail to determine how they impact the development of new CSP systems economically and effectively. Therefore, the aims of the thesis are set as follows:

a) Investigating the hydrodynamics and thermal modelling parameters affecting TFM results for spouted bed thermal receivers,
    - Investigating the effects of the hydrodynamic modelling parameters and related constitutive equations,
    - Investigating the effects of the thermal modelling parameters and related constitutive equations,
b) To assess the prediction performance of TFM for spouted bed thermal receivers using different data sets from the literature as well as in-house experimental data,

The hydrodynamic and thermal modelling are limited to laboratory scale spouted beds. Upon the completion of the thesis, it is expected that relatively new information related to modelling of CSP spouted bed thermal receivers with two-fluid approach is generated that will be a reference for future research.

2. THEORY OF TWO FLUID MODEL

2.1. Introduction

Complex solid-gas flow simulations can be conducted using Two Fluid Models (TFM). The solid and gas phases are presumed to be a continuum flow in the TFM. Numerical calculations for each phase are carried out separately using the energy, momentum, and mass conservation equations. Because of the gas-solid interactions, additional terms are also defined in each momentum and energy equation. Different drag models can characterize forces from gas-solid interaction in the momentum equations. Besides, different Nusselt correlations can be described regarding the heat transfer because of the interaction of gas-solid phases.

The solid phase continuum parameters can be described by the kinetic theory of granular flow (KTGF) that allows to compute viscosity and pressure of the particles because a continuum phase is defined for the solid phase. Furthermore, a granular temperature in KTGF is characterized by the fluctuation of the particle's kinetic energy after collision. A formulation of granular temperature is used to compute solids phase parameters. A separate transport equation is solved for granular temperature accounting for its production and dissipation. Furthermore, additional constitutive equations are required in KTGF. Therefore, this section examines the energy and momentum equations alongside the constitutive equations, that are essential in TFM theory.

First, interpenetrating continua assumptions are defined for gas and solid phases before solving differential energy, momentum, and continuity equations. Additionally, the following assumptions are made in the Eulerian framework:

- A phasic volume fraction represents each phase.
- Each phase maintains its volume without occupying the other.
- In space and time, continuous functions are considered for the volume fractions.
- The summation of the volume fractions of all phases equals 1.

The volume fraction of both phases is summated in Equation (2.1).

$$\varepsilon_g + \varepsilon_s = 1.0 \tag{2.1}$$

The subscripts of g demonstrate the gas phase. Meanwhile, the subscripts of s represent the solid phase. In Equation (2.1), the term of ε represents each phase's volume fraction.

2.2. Conservation Equations

A spouted bed's hydrodynamic and thermal models use the energy, momentum, and mass conservation equations. This section details the conservation equations and related constitutive equations.

2.2.1. Continuity Equations

Equation (2.2) demonstrates the solid phase. Meanwhile, Equation (2.3) represents for the gas phase. Any mass transfer among the phases is not represented in these equations. The mass accumulation rate is represented in the first left-hand-sided term of the equations. Furthermore, the second term of the equations is indicated for the net rate belonging to convective mass flux. Additionally, all terms in Equations (2.2) and (2.3) indicate per unit volume.

For solid phase:

$$\frac{\partial}{\partial t}(\varepsilon_s \rho_s) + \nabla.(\varepsilon_s \rho_s \vec{u}_s) = 0 \tag{2.2}$$

For gas phase:

$$\frac{\partial}{\partial t}\left(\varepsilon_g \rho_g\right) + \nabla.\left(\varepsilon_g \rho_g \vec{u}_g\right) = 0 \tag{2.3}$$

Where ε, ρ, and $\vec{u}$ represent each phase's volume fraction, density, and velocity.

2.2.2. Momentum Equations

The general expression of the momentum conservative equation is demonstrated in Equation (2.4) for the gas phase.

$$\frac{\partial}{\partial t}\left(\varepsilon_g\rho_g\vec{u}_g\right)+\nabla.\left(\varepsilon_g\rho_g\vec{u}_g\vec{u}_g\right) \\ = -\varepsilon_g\nabla p+\nabla.\bar{\bar{\tau}}_g+\vec{F}_{drag}+\varepsilon_g\rho_g(\vec{F}_g+\vec{F}_{lift,g}+\vec{F}_{vm,g}) \tag{2.4}$$

The external body forces are indicated as $\vec{F}_g$ in Equation (2.4). $\vec{F}_{lift,g}$ represents the lift force. Meanwhile, the force of the virtual mass is shown as $\vec{F}_{vm,g}$. The interaction (drag) force between the two phases, indicated as $\vec{F}_{drag}$, is part of the momentum equation. Lift, virtual mass, and drag forces can affect momentum equations coupled among the gas-solid phases. However, gas and solid phases have a significant difference in their densities. Hence, lift and virtual mass forces are smaller in magnitude than drag force for spouted and fluidized bed conditions. As a result, the lift force can usually be ignored, as well as virtual mass [40].

The drag force is stated in Equation (2.5).

$$\vec{F}_{drag}=K_{gs}(\vec{u}_s-\vec{u}_g) \tag{2.5}$$

where, K_{gs} represents the coefficient of momentum transfer by the interphases. The term of $(\vec{u}_s-\vec{u}_g)$ is indicated as the relative velocity among the phases. These two terms in Equation (2.5) also determine the drag force on particles by the gas-solid interaction [16].

When the lift and the virtual mass forces are ignored, Equation (2.4) can be transformed to Equations (2.6) and (2.7) for both phases, respectively.

For solid phase:

$$\frac{\partial}{\partial t}(\varepsilon_s\rho_s\vec{u}_s)+\nabla.(\varepsilon_s\rho_s\vec{u}_s\vec{u}_s) \\ = -\varepsilon_s\nabla p+\nabla.\bar{\bar{\tau}}_s+\varepsilon_s\rho_s\vec{g}+K_{gs}\left(\vec{u}_s-\vec{u}_g\right)-\nabla p_s \tag{2.6}$$

For gas phase:

$$\frac{\partial}{\partial t}\left(\varepsilon_g\rho_g\vec{u}_g\right)+\nabla.\left(\varepsilon_g\rho_g\vec{u}_g\vec{u}_g\right)=-\varepsilon_g\nabla p+\nabla.\bar{\bar{\tau}}_g+\varepsilon_g\rho_g\vec{g}+K_{gs}\left(\vec{u}_g-\vec{u}_s\right) \tag{2.7}$$

The pressure is represented by p, which all phases share. The tensor of stress belonging to the gas phase is represented as $\bar{\bar{\tau}}_g$. Moreover, $\bar{\bar{\tau}}_s$ also represents the tensor of stress belonging to the solid phase. The gravitational acceleration, $\vec{g}$, is part belonging to the equation of the momentum.

The time rate belonging to the variation of momentum is represented in the first left-hand-sided term of the equations. The second term demonstrates the convective momentum transport. The phase pressure force is shown in the first right-hand sided term. The viscous force is represented within the second term. The gravitational force is indicated in the third term. The gas-solid interaction force is shown in the fourth term. The solid phase pressure force is only observed in the solid momentum equation. Additionally, all terms in Equations (2.6) and (2.7) have a unit of force per unit volume.

2.2.3. Constitutive Relations for Momentum

The momentum exchange coefficient couples the momentum equations of both phases. Interaction among phases causes these momentum exchanges. Drag models allow modeling this interaction in the equations. Different drag models exist in the literature. Generally, Syamlal-O'Brien, Ergun, Gidaspow, and Wen-Yu drag models are suggested to model gas-solid flow. Solid Reynolds numbers and volume fractions are the most important parameters in the drag models. Hence, in the spouted beds, the drag models have essential effects on gas-solid flow dynamics. Furthermore, Ansys Fluent, which is the commercial CFD software, mainly offers these drag models. This section describes the solid-gas momentum exchange coefficient in detail.

Before solving the solid momentum equation, solid stress tensor ($\bar{\bar{\tau}}_s$) and solid phase pressure (p_s) must be defined as the constitutive equations. Because solid particles are not fluid, they must be reduced to continuum within TFM. Therefore, their stress tensor and pressure terms are only defined with the constitutive equations. These constitutive equations are expressed within the context of KTGF. The constitutive equations and their methodology are also presented in this section.

2.2.3.1. The Solid-Gas Momentum Exchange Coefficient

Syamlal and O'Brien is one of the fundamental drag models used for gas-solid flows. They developed especially for fluidized beds, considering the terminal velocities of particles [40, 41]. Equation (2.8) gives the solid-gas momentum exchange coefficient of Syamlal and O'Brien.

$$K_{gs} = \frac{3}{4} C_D \frac{\varepsilon_s \varepsilon_g \rho_g}{v_{r,s}^2 d_s} \left(\frac{Re_s}{v_{r,s}} \right) \left| \vec{u}_s - \vec{u}_g \right| \tag{2.8}$$

The density is shown as ρ_g. The viscosity is represented by μ_g, and the velocity of the gas phase is demonstrated as $\vec{u}_g$. The Particles' diameter is represented as d_s. The velocity of the solid phase is indicated as $\vec{u}_s$. The Reynolds number and terminal velocity correlation of solid phases are represented by $v_{r,s}$, and Re_s and respectively. C_D is the drag coefficient in the drag equation belonging to Syamlal and O'Brien.

Terminal velocity correlation of solid phase:

$$v_{r,s} = 0.5 \left(A - 0.06 Re_s + \sqrt{(0.06 Re_s)^2 + 0.12 Re_s (2B - A) + A^2} \right) \tag{2.9}$$

$$A = \varepsilon_g^{4.14}, \qquad B = \begin{cases} 0.8 \varepsilon_g^{1.28}, & for\ \varepsilon_g \leq 0.85 \\ \varepsilon_g^{2.65}, & for\ \varepsilon_g > 0.85 \end{cases} \tag{2.10}$$

The solid Reynolds number is demonstrated as:

$$Re_s = \frac{\rho_g d_s \left| \vec{u}_s - \vec{u}_g \right|}{\mu_g} \tag{2.11}$$

Syamlal and O'Brien formulation's the drag coefficient is defined as:

$$C_D = \left(0.63 + \frac{4.8}{\sqrt{\frac{Re_s}{v_{r,s}}}} \right)^2 \tag{2.12}$$

Ergun suggested an empirical correlation according to the calculation of the pressure drop in fixed beds. The drag model takes into account losses of viscous and kinetic energy. Equation (2.13) gives Ergun's momentum exchange coefficient for the gas-solid interaction [42, 43].

$$K_{gs} = 150\frac{\varepsilon_s(1-\varepsilon_g)\mu_g}{\varepsilon_g d_s^2} + 1.75\frac{\rho_g\varepsilon_s|\vec{u}_s - \vec{u}_g|}{d_s} \tag{2.13}$$

According to bed expansion measurements to scale Stokes-drag, Wen and Yu developed an empirical drag equation. Wen and Yu's momentum exchange coefficient for the gas-solid interaction is given in Equation (2.14) [42, 44, 45].

$$K_{gs} = \frac{3}{4}C_D\frac{\varepsilon_s\varepsilon_g\rho_g|\vec{u}_s - \vec{u}_g|}{d_s}\varepsilon_g^{-2.65} \tag{2.14}$$

The drag coefficient of Wen and Yu:

$$C_D = \begin{cases} \frac{24}{\varepsilon_g Re_s}\left[1 + 0.15\left(\varepsilon_g Re_s\right)^{0.687}\right], & Re_s < 1000 \\ 0.44, & Re_s \geq 1000 \end{cases} \tag{2.15}$$

The solid Reynolds number in Equation (2.15) is the same as in Equation (2.11).

Gidaspow composed the coupled with Wen-Yu and Ergun equations as a new drag model that is more suitable for denser fluidized beds [40, 46, 47]. Equation (2.16) gives the exchange coefficient of the momentum of Gidaspow for the solid-gas interaction.

$$K_{gs} = \begin{cases} K_{gs} = 150\frac{\varepsilon_s(1-\varepsilon_g)\mu_g}{\varepsilon_g d_s^2} + 1.75\frac{\rho_f\varepsilon_s|\vec{u}_s - \vec{u}_g|}{d_s}, & for\ \varepsilon_g < 0.80 \\ K_{gs} = \frac{3}{4}C_D\frac{\varepsilon_s\varepsilon_g\rho_g|\vec{u}_s - \vec{u}_f|}{d_s}\varepsilon_g^{-2.65}, & for\ \varepsilon_g \geq 0.80 \end{cases} \tag{2.16}$$

The drag coefficient, C_D, in Equation (2.16) is the same as in Equation (2.15).

2.2.3.2. Kinetic Theory of Granular Flow (KTFG)

A slowly and rapidly shearing regimes are two distinct flow regimes for granular flows. The rapid shear causes particle stresses, which result from translational or collisional transfer in momentum. Additionally, kinetic contributions dominate in the rapidly shearing flow regime. On the other hand, the normal and tangential frictional forces cause the slowly shearing or plastic regime, which is another reason for the particle stresses. The main reason for these forces is sliding contacts. Furthermore, friction dominates in the slowly shearing regime. Hence, these types of stresses occur at high particle concentrations. All stresses are defined as solid pressure and viscosity, which is established in the kinetic theory for granular flows (KTGF) [16].

The particle velocity is divided into two components after the collision. The first component is a mean velocity ($\vec{u}_{s,mean}$). Furthermore, a fluctuating random velocity ($\vec{u}_s'$) is the second component. The particle stresses cause fluctuations in the particle velocity. Their measurement is defined as the granular temperature [16]. The decomposition of the velocity of particles is given in Equation (2.17). The granular temperature is also given in Equation (2.18).

$$\vec{u}_s = \vec{u}_{s,mean} \pm \vec{u}_s' \tag{2.17}$$

$$\frac{2}{3}\theta_s = (\vec{u}_s'.\vec{u}_s') \tag{2.18}$$

Equation (2.19) gives the granular temperature's transport equation that is reproduce from changes in the kinetic theory of gases [47].

$$\begin{aligned} \frac{3}{2}\left[\frac{\partial}{\partial t}(\varepsilon_s\rho_s\theta_s) + \nabla.(\varepsilon_s\rho_s\vec{u}_s\theta_s)\right] \\ = \left(-p_s\bar{\bar{I}} + \bar{\bar{\tau}}_s\right):\nabla\vec{u}_s + \nabla.\left(k_{\theta_s}\nabla\theta_s\right) - \gamma_{\theta_s} + \emptyset_{gs} \end{aligned} \tag{2.19}$$

The granular temperature conductivity is shown as k_{θ_s}. γ_{θ_s} demonstrates the dissipation of granular energy. $\emptyset_{gs}$ indicates the interphase energy transfer in granular temperature's transport equation.

The first right-hand-sided term in Equation (2.19) indicates the ratio of variation of granular energy. Furthermore, the second term represents a change in the granular energy due to convection. The generation granular energy that is derived from a solid stress tensor is shown in the first right-hand-sided term. The diffusion belonging to granular energy is represented in the second term. Moreover, the third term indicates dissipation of energy due to collisional. The interphase energy transfer is shown in the fourth term [44].
The convection and diffusive terms can be neglected under these conditions: the local equilibrium of granular fluctuation energy and the local balance between its production and dissipation [48]. Equation (2.19) is then transformed to Equation (2.20), which gives the granular energy balance equation under this assumption.

$$0 = \left(-p_s\bar{\bar{I}} + \bar{\bar{\tau}}_s\right):\nabla\vec{u}_s - \gamma_{\theta_s} \tag{2.20}$$

The collisional dissipation of energy occurs as a result of Collisions between particles. The term of γ_{θ_s} in Equation (2.20) is represents the energy dissipation ratio. Lun *et al.* [49] proposed the expression of the collisional dissipation of energy that is given in Equation (2.21).

$$\gamma_{\theta_s} = \frac{12(1 - e_{ss}^2)g_0}{d_s\sqrt{\pi}}\,\rho_s\varepsilon_s^2\theta_s^{\frac{3}{2}} \tag{2.21}$$

In Equation (2.21), the restitution coefficient is shown as e_{ss}. The restitution coefficient is related to the ratio of how much kinetic energy is kept after the collision of two particles. A perfectly elastic collision is observed when the particle protects its kinetic energy after the collision. When the restitution coefficient equals to 1, the perfectly elastic collision is simulated. On the contrary, a perfectly plastic collision is observed when the particle loses its kinetic energy after the collision. The perfectly plastic collision is simulated when the restitution coefficient equals to 0 [44]. The coefficient of restitution is hard to measure by experimentally and depends on stiffness ratio, impact velocity, and material properties [50].

Moreover, in Equation (2.21), g_0 demonstrates the radial distribution function that is described the touching possibility of two particles. It is used for a modification factor of the probability of collisions between particles in denser solid phases [49]. Equation (2.22) gives an expression of the radial distribution function.

$$g_0 = \left[1 - \left(\frac{\varepsilon_s}{\varepsilon_{s,max}}\right)^{\frac{1}{3}}\right]^{-1} \tag{2.22}$$

In Equation (2.22), $\varepsilon_{s,max}$ represents the maximum packing limit that indicates the maximum volume voidage for the particles. Moreover, when the particles have the shapes of monodispersed spheres, the maximum theoretical packing limit is 0.6.

Lun *et al*. [49] proposed an equation for solid pressure, which is given in Equation (2.23).

$$p_s = \varepsilon_s \rho_s \theta_s + 2\rho_s(1 + e_{ss})\varepsilon_s^2 g_0 \theta_s \tag{2.23}$$

The kinetic component associated with the momentum transferred due to the shear stress from particle flow is represented in the first right-hand-sided term. The collisional contribution resulting from the momentum transferred during particle collisions is demonstrated in the second term [44].

The equation (2.24) gives the solids stress tensor.

$$\bar{\bar{\tau}}_s = \left(\lambda_s - \frac{2}{3}\mu_s\right)\nabla.\vec{\mathrm{u}}_s\bar{\bar{\mathrm{I}}} + \mu_s[\nabla\vec{u}_s + (\nabla\vec{u}_s)^T] \tag{2.24}$$

The particle collisional and translational momentum transfer causes shear and bulk viscosities to be represented in the solids stress tensor.

$$\lambda_s = \frac{4}{3}\ \varepsilon_s^2 \rho_s d_s g_0 (1 + e_{ss})\ \frac{\theta_s}{\pi})^{\frac{1}{2}} \tag{2.25}$$

Lun *et al*. [49] proposed an equation for solid bulk viscosity in Equation (2.25). When the granular particles compress or expand, they show the resistance calculated in the equation.

$$\mu_s = \mu_{s,col} + \mu_{s,kin} + \mu_{s,fric} \tag{2.26}$$

Equation (2.26) gives solid shear viscosity, including collisional ($\mu_{s,col}$), kinetic ($\mu_{s,kin}$), and frictional components ($\mu_{s,fric}$).

$$\mu_{s,col} = \frac{4}{5}\varepsilon_s \rho_s d_s g_0 (1 + e_{ss}) \left(\frac{\theta_s}{\pi}\right)^{\frac{1}{2}} \tag{2.27}$$

Equation (2.27) gives the shear viscosity's collisional component [51].

Syamlal *et al*. [51] and Gidaspow *et al*. [52] proposed different kinetic part of shear viscosity. The expression of Syamlal is given in Equation (2.28). Additionally, the expression of Gidaspow is given in Equation (2.29).

$$\mu_{s,kin} = \frac{d_s \rho_s \sqrt{\theta_s \pi}}{6(3 - e_{ss})}\left[1 + \frac{2}{5}(1 + e_{ss})(3e_{ss} - 1)\varepsilon_s g_0\right] \tag{2.28}$$

$$\mu_{s,kin} = \frac{10 \rho_s d_s \sqrt{\theta_s \pi}}{96 \varepsilon_s (1 + e_{ss}) g_0}\left[1 + \frac{4}{5}\varepsilon_s g_0 (1 + e_{ss})\right]^2 \tag{2.29}$$

The frictional part of viscosity is given in Equation (2.30). It is derived by Schaeffer [53]. Friction between particles in dense flow at low shear causes the stresses described in the equation.

$$\mu_{s,fric} = \frac{P_s sin\emptyset}{2\sqrt{I_{2D}}} \tag{2.30}$$

The solid frictional pressure is shown as P_s in Equation (2.30). The internal friction's angel is represented by $\emptyset$. Moreover, indicates the deviatoric stress tensor for the second invariant I_{2D}.

$$\vec{\tau}_s = -\frac{\pi}{6}\sqrt{3}\varphi \frac{\varepsilon_s}{\varepsilon_{s,max}} \rho_s g_0 \sqrt{\theta_s} \vec{u}_{s,w} \tag{2.31}$$

Equation (2.31) gives the shear force at the wall [46]. $\vec{u}_{s,w}$ represents the tangential velocity component of the particles on the wall. Moreover, the friction between the wall and particles is characterized as the specularity coefficient that is indicated as φ. No friction is observed between the particles and the wall when φ equals 0. Furthermore, the particle slips on the wall with no shearing resistance. Otherwise, when φ equals 1, the shearing resistance is observed the highest value. Hence, the particles stick practically to the wall. When the value of φ increases, the shear stress on the particles increases on the wall.

2.2.4. Energy Equations

Equation (2.32) gives the extensive form of the energy equation, which is defined in Ansys Fluent [46]. It consists of mechanical and thermal energy terms and represents for the gas phase.

$$\frac{\partial}{\partial t}\left(\varepsilon_g \rho_g E_g\right) + \nabla.\left(\varepsilon_g \vec{u}_g (\rho_g E_g + p)\right) = \nabla.\varepsilon_g \kappa_{eff,g} \nabla T_g - \nabla.\sum_j H_{j,g} \vec{J}_{j,g} + \nabla.\bar{\bar{\tau}}_g.\vec{v}_g + \left(Q_{sg} + \dot{m}_{sg} H_{sg} - \dot{m}_{gs} H_{gs}\right) + S_g \tag{2.32}$$

The left-hand-sided terms of Equation (2.32) represent the rate of energy variation and the energy due to convection, respectively. The first two right-hand-sided terms indicate energy transfer affected by conduction and species diffusion, respectively. The third term indicates viscous dissipation. Furthermore, the fourth term demonstrates the amount of heat exchange from other phases. The last term includes a volumetric heat source due to radiation or chemical reactions.

"Q_{sg}" represents the heat exchange rate due solid-gas interaction. On the other hand, the term "$\dot{m}_{sg} H_{sg} - \dot{m}_{gs} H_{gs}$" is given as the heat energy rate due to a phase change in the fluid phase, such as condensation or evaporation of the droplet. $\dot{m}_{sg}$ and H_{sg} are the mass transfer and the interphase enthalpy due to phase change, respectively.

The species diffusion term includes that the heat energy transfer rate of different materials resulting from combustion or chemical reaction. Enthalpy and diffusive flux of species j in the gas phase is represented by $H_{j,g}$ and $\vec{J}_{j,g}$ respectively.

Since the spouted bed has no combustion and phase change, Equation (2.32) can be simplified as Equation (2.33).

$$\frac{\partial}{\partial t}\left(\varepsilon_g \rho_g E_g\right) + \nabla.\left(\varepsilon_g \vec{u}_g (\rho_g E_g + p)\right) \\ = \nabla.\varepsilon_g \kappa_{eff,g} \nabla T_g + \nabla.\bar{\bar{\tau}}_g.\vec{v}_g + Q_{sg} + S_g \tag{2.33}$$

Equation (2.34) represents the unit total energy for the gas phase. It is a summation of internal enthalpy and kinetic energy, and Equation (2.35) gives the internal energy. The constant volume heat capacity of the gas phase is demonstrated as $c_{v,g}$ in Equation (2.35).

$$E_g = I_g + \frac{\vec{u}_g{}^2}{2} \tag{2.34}$$

$$I_g = \int_{T_{ref}}^{T} c_{v,g} dT_g \tag{2.35}$$

Furthermore, enthalpy for the gas phase is demonstrated in Equation (2.36).

$$H_g = I_g + \frac{p}{\rho_g} \tag{2.36}$$

Using Equation (2.36), Equation (2.34) is changed to Equation (2.37).

$$E_g = H_g - \frac{p}{\rho_g} + \frac{\vec{v}_g{}^2}{2} \tag{2.37}$$

Equation (2.38) is derived from Equation (2.37) integrated into Equation (2.33).

$$\frac{\partial}{\partial t}\left(\varepsilon_g\rho_g(H_g+\frac{\vec{u}_g^{\;2}}{2})\right)+\nabla.\left(\varepsilon_g\rho_g\vec{u}_g(H_g+\frac{\vec{u}_g^{\;2}}{2})\right)$$
$$=\nabla.\varepsilon_g\kappa_{eff,\mathrm{g}}\nabla T_g+\nabla.\bar{\bar{\tau}}_{\mathrm{g}}.\vec{u}_g+Q_{sg}+p\frac{\partial\varepsilon_g}{\partial t}+S_g \tag{2.38}$$

For incompressible and negligible viscous dissipation assumptions, mechanical energy terms (Pressure work and kinetic energy) can be neglected in Equation (2.38). It can be reproduced as Equation (2.39), which is also identified as the thermal energy equation or energy equation in enthalpy form.

$$\frac{\partial}{\partial t}\left(\varepsilon_g\rho_g(H_g)\right)+\nabla.\left(\varepsilon_g\rho_g\vec{u}_g(H_g)\right)=\nabla.\varepsilon_g\kappa_{eff,\mathrm{g}}\nabla T_g+Q_{sg}+S_g \tag{2.39}$$

Where κ_{eff} indicates the effective thermal conductivity. Moreover, Q_{sg} is the energy transfer terms among gas-solid phases and defined as:

$$Q_{sg}=\alpha\left(T_s-T_g\right) \tag{2.40}$$

where α is the volumetric interphase heat-transfer coefficient. Furthermore, the temperature of the solid and gas phases is represented by T_s and T_g, respectively.

Using Equation (2.40) and Equation (2.39), energy equations can be identified for solid and gas phases. Equation (2.41) shows for the solid phase, and Equation (2.42) gives for the gas phase energy equations. $S_{radiation}$ is a directly irradiated solar heat source for the spouted bed receiver.

$$\frac{\partial}{\partial t}(\varepsilon_s\rho_sH_s)+\nabla.(\varepsilon_s\rho_s\vec{u}_sH_s)=\nabla.\varepsilon_s\kappa_{eff,s}\nabla T_s+\alpha\left(T_g-T_s\right)+S_{radiation} \tag{2.41}$$

$$\frac{\partial}{\partial t}\left(\varepsilon_g\rho_gH_g\right)+\nabla.\left(\varepsilon_g\rho_g\vec{u}_gH_g\right)$$
$$=\nabla.\varepsilon_g\kappa_{eff,g}\nabla T_g+\alpha\left(T_s-T_g\right)+S_{radiation} \tag{2.42}$$

A literature survey was conducted to identify studies investigating heat transfer's effects on fluidized beds in TFM. The gas phase energy equation of all the studies is summarized in Table 2.1. However, they used different notations. So, their notations were changed to this thesis's notation. Syamlal and Gidaspow [54] and Kuipers *et al*. [55] derived the energy equation with the enthalpy term. Schmidt and Renz [56] involved the work of expansion of the voidage and the viscous dissipation into the energy equation. Other studies are similar to the thesis's energy equation. None of the studies involved source terms because they only investigated the effects of gas-to-solid or bed-to-wall heat transfer without radiation.

Table 2.1 Summary of the gas phase energy equation in other TFM studies in the literature.

References	Expression of the energy equation of the gas phase
Syamlal and Gidaspow [54]	$\frac{\partial(\varepsilon_g\rho_g I_g)}{\partial t}+\frac{\partial(\varepsilon_g\rho_g I_g\vec{u}_g)}{\partial x}+\frac{\partial(\varepsilon_g\rho_g I_g\vec{u}_g)}{\partial y}=-p\left[\frac{\partial\varepsilon_g}{\partial t}+\frac{\partial(\varepsilon_g\vec{u}_g)}{\partial x}+\frac{\partial(\varepsilon_g\vec{u}_g)}{\partial x}\right]+\alpha(T_s-T_g)+\frac{\partial}{\partial x}\left(\kappa_{eff,g}\varepsilon_g\frac{\partial T_g}{\partial x}\right)+\frac{\partial}{\partial y}\left(\kappa_{eff,g}\varepsilon_g\frac{\partial T_g}{\partial y}\right)$
Kuipers *et al.* [55]	$\frac{\partial(\varepsilon_g\rho_g I_g)}{\partial t}+(\nabla.\varepsilon_g\rho_g I_g\vec{u}_g)=-p\left[\frac{\partial\varepsilon_g}{\partial t}+(\nabla.\varepsilon_g\vec{u}_g)\right]+(\nabla.\varepsilon_g\kappa_{eff,g}\nabla T_g)-\alpha(T_g-T_s)$
Schmidt and Renz [56, 57]	$\frac{\partial(\varepsilon_g\rho_g H_g)}{\partial t}+\nabla.(\varepsilon_g\rho_g H_g\vec{u}_g)=-\nabla.\varepsilon_g.q_g+\alpha(T_s-T_g)+\tau_g.\nabla.\vec{u}_g+\varepsilon_g\left[\frac{\partial p}{\partial t}+\vec{u}_s\nabla p\right]$
Patil *et al.* [58]	$\frac{\partial(\varepsilon_g\rho_g H_g)}{\partial t}+\nabla.\varepsilon_g\rho_g\vec{u}_g H_g=\nabla.\varepsilon_g\kappa_{eff,g}\nabla T_g-\alpha(T_g-T_s)$
Armstrong *et al.* [59]	$\frac{\partial(\varepsilon_g\rho_g H_g)}{\partial t}+\nabla.\varepsilon_g\rho_g\vec{u}_g H_g=\nabla.\varepsilon_g\kappa_{eff,g}\nabla T_g-\alpha(T_g-T_s)$
Yusuf *et al.* [60]	$\frac{\partial(\varepsilon_g\rho_g H_g)}{\partial t}+\nabla.\varepsilon_g\rho_g\vec{u}_g H_g=\nabla.\varepsilon_g\kappa_{eff,g}\nabla T_g-\alpha(T_g-T_s)$

2.2.5. Constitutive Relations for Energy

Effective thermal conductivity is obtained from constitutive equations for energy. The volumetric interphase heat-transfer coefficient is also produced in the same relations. In this section, these equations are explained in detail.

2.2.5.1. The Thermal Conductivity

The voidage of the solid particles is filled by the gas phase in the fluidized or spouted beds. Hence, not only do the solid particles contact each other, but they also contact the gas phase. As a result, the thermal conductivity belonging to solid bulk particles can be different from that of solid material. Therefore, Zehner and Schlunder [61] developed the concept of the bulk's thermal conductivity as a mathematical description that depends on the thermal properties of the particle and gas materials and their void fraction. Additionally, the gas and solid phases in TFM can be applied separately into these formulations.

Gidaspow and Syamlal [54] and Kuiper *et al*. [55] embedded the Zehner and Schlunder formulations in their fluidized bed simulation using TFM. They used them to obtain wall-to-bed heat transfer. Schmidt and Renz [56] described these formulations as a standard approach. On the other hand, they described the Hunt model as a kinetic approach based on KTGF to describe the thermal conductivity of a particulate phase. Patil *et al*. [58] combined standard and kinetic approaches for solid-phase thermal conductivity. They modified Martin's porosity model for the near-wall and performed his equation in their model. On the contrary, unlike Patil's model, Armstrong *et al*. [59] used only the standard approach and the porosity model in the area close to the wall. According to Yusuf et al. [60], variations in thermal conductivities of solid phase can be observed in various regions of the bed. Furthermore, the Zehner and Schlunder approach is more suitable in the center of the bed. However, it can overestimate for the solid phase because the volume fraction suddenly changes dramatically in the near wall. Hence, they suggested that the Legawiec and Ziolkowski model be utilized to acquire the heat transfer coefficient at wall-to-bed. The Zehner and Schlunder formulation was not embedded in Ansys Fluent.

Seven different thermal conductivities are defined in constitutive equations for energy. Their definitions are explained in this section. Table 2.2 gives the notations of seven different thermal conductivities.

Table 2.2 Summarization of the notation of different thermal conductivities.

Notation of Different Thermal Conductivities	Definition	Unit
$\kappa_{g,\mathrm{o}}$	True conductivity of gas material (not phase form)	W/mK
$\kappa_{s,\mathrm{o}}$	True conductivity of solid material (not phase form)	
$\kappa_{b,\mathrm{g}}$	Bulk thermal conductivity of gas phase	
$\kappa_{b,\mathrm{s}}$	Bulk thermal conductivity of solid phase	
κ_b	Bulk thermal conductivity of mixture belonging to solid and gas phases	
$\kappa_{eff,\mathrm{g}}$	Effective thermal conductivity of gas phase (It is related to gas phase volume fraction.)	
$\kappa_{eff,\mathrm{s}}$	Effective thermal conductivity of solid phase (It is related to solid phase volume fraction.)	

Zehner-Schlunder's Standard approach:

The total bulk thermal conductivity is indicated as the summation of the gas and solid bulk thermal conductivities. Equation (2.43) represents the formulation of the total bulk thermal conductivity.

$$\kappa_b = \kappa_{b,\mathrm{g}} + \kappa_{b,\mathrm{s}} \tag{2.43}$$

where κ_b is the total bulk thermal conductivity. Moreover, the gas and solid bulk thermal conductivities are demonstrated as $\kappa_{b,g}$ and $\kappa_{b,s}$, respectively.

Equation (2.44) gives the gas bulk thermal conductivity. $\kappa_{g,o}$ represents the true gas thermal conductivity in Equation (2.44). Additionally, Equation (2.45) gives the solid bulk thermal conductivity.

$$\kappa_{b,g} = \left(1 - \sqrt{(1-\varepsilon_g)}\right)\kappa_{g,o} \tag{2.44}$$

$$\kappa_{b,s} = \sqrt{(1-\varepsilon_g)}\,[\omega A + (1-\omega)\Gamma]\kappa_{g,o} \tag{2.45}$$

$$\Gamma = \frac{2}{\left(1-\frac{B}{A}\right)}\left[\frac{(A-1)}{\left(1-\frac{B}{A}\right)^2}\frac{B}{A}\ln\left(\frac{A}{B}\right) - \frac{(B-1)}{\left(1-\frac{B}{A}\right)} - \frac{(B+1)}{2}\right] \tag{2.46}$$

A is the proportion of true solid thermal conductivity to true gas thermal conductivity. It is given in Equation (2.47). $\kappa_{s,o}$ also represents the true solid thermal conductivity in Equation (2.47).

$$A = \frac{\kappa_{s,o}}{\kappa_{g,o}} \tag{2.47}$$

The shape factor is indicated as B. It characterizes the geometrical effect belonging to the solid particle. For spheres, B is equal to Equation (2.48).

$$B = 1.25\left(\frac{(1-\varepsilon_g)}{\varepsilon_g}\right)^{10/9} \tag{2.48}$$

The ratio of the particle contact area is indicated as ω, which is 7.26×10^{-3} for the total particle surface area of spheres.

The effective gas and solid thermal conductivities are defined in the energy equations. Furthermore, they have a relation with the gas and the solid bulk thermal conductivities, respectively. Equation (2.49) shows the relation between gas bulk and effective fluid thermal conductivities.

$$\kappa_{eff,f} = \frac{\kappa_{b,g}}{\varepsilon_g} \tag{2.49}$$

According to Kuipers *et al.* [55], and Schmidt and Renz [56], Equation (2.50) shows the relation between solid bulk and effective solid thermal conductivities. Conversely, according to Patil *et al.* [58], L.M. Armstrong *et al*. [59], and R. Yusuf *et al*. [60], Equation (2.51) gives the relation between the solid bulk and the effective solid thermal conductivities.

$$\kappa_{eff,s} = \frac{\kappa_{b,s}}{\varepsilon_s} \tag{2.50}$$

$$\kappa_{eff,s} = \frac{\kappa_{b,s}}{\sqrt{\varepsilon_s}} \tag{2.51}$$

Using Equation (2.44), Figure 2.1 was obtained for nominal gas bulk thermal conductivity with different gas fraction values.

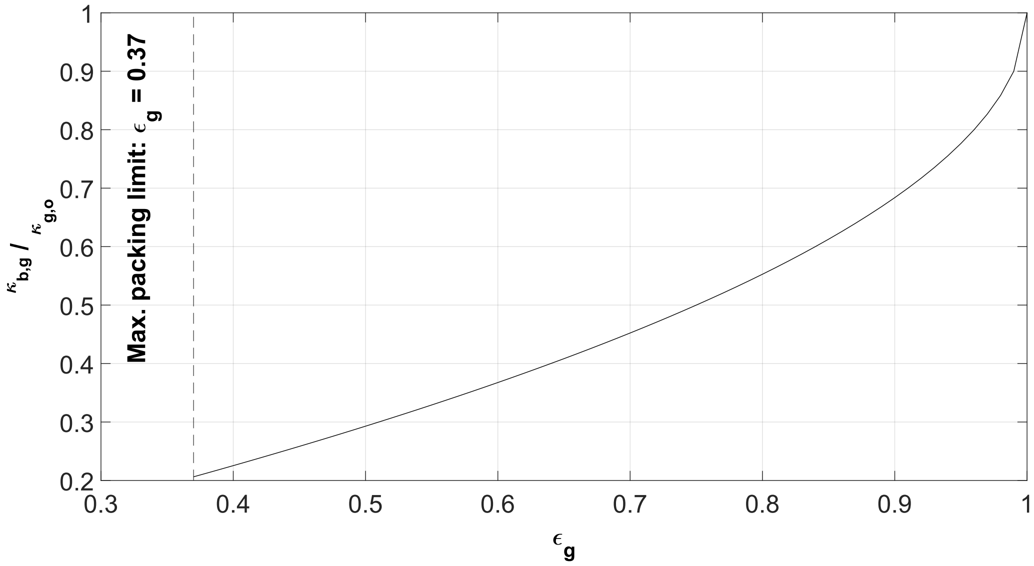

Figure 2.1 Nominal gas bulk thermal conductivity vs gas volume fraction.

Using Equation (2.45), Figure 2.2 and Figure 2.3 were obtained for nominal gas bulk thermal conductivity with different gas fraction values and different ratios of true solid thermal conductivity to true gas thermal conductivity, respectively.

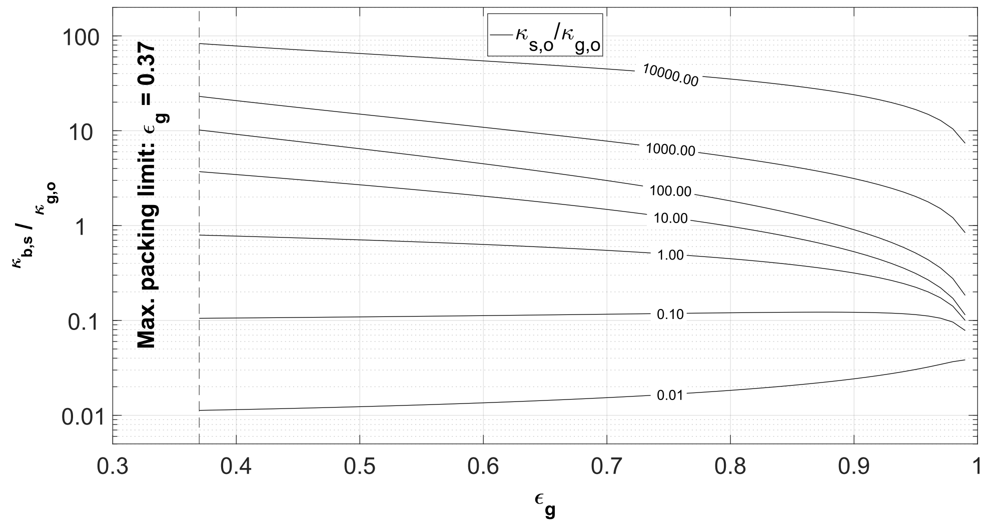

Figure 2.2 Nominal solid bulk thermal conductivity vs gas volume fraction.

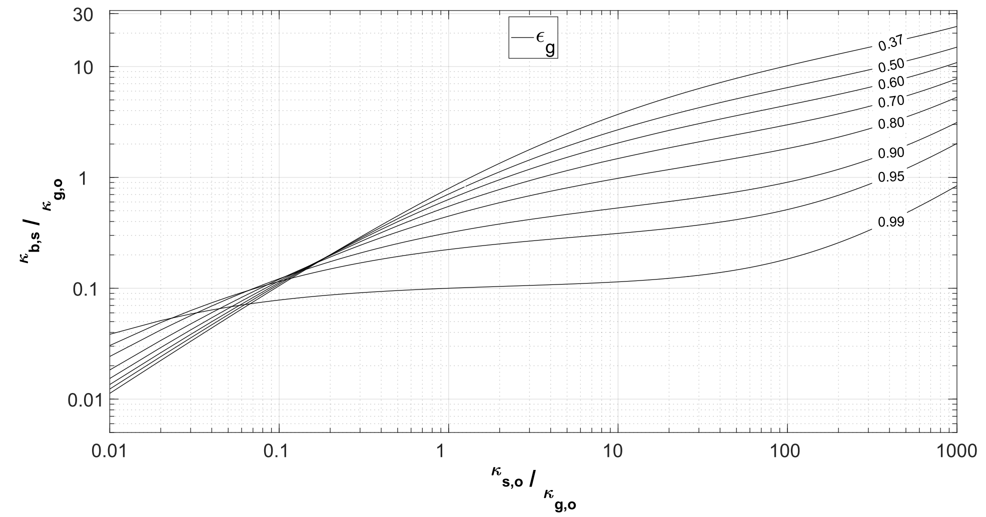

Figure 2.3 Nominal solid bulk thermal conductivity vs proportion of true solid thermal conductivity to true gas thermal conductivity.

Kinetic approach:

The kinetic approach can only be used to obtain the solid bulk thermal conductivity, which is given in Equation (2.52). On the other hand, Equation (2.44) is still valid for calculating the gas bulk thermal conductivity, which is the same as the standard approach.

$$\kappa_{b,s} = \varepsilon_s \rho_s c_{p,s} d_s \pi^{\frac{3}{2}} \frac{\sqrt{\theta}}{32 g_0} \tag{2.52}$$

θ represents the granular temperature which is evaluated from Equation (2.18). g_0 indicates the radial distribution function based on Hunt model [56]. Equation (2.53) also gives the formulation of the radial distribution function.

$$g_0 = \frac{16-7\varepsilon_s}{16(1-\varepsilon_s)^2} \tag{2.53}$$

However, the radial distribution function of the Hunt model has not been embedded in Ansys Fluent. So, Ansys Fluent uses Equation (2.22) for the radial distribution function.

2.2.5.2. The Interphase Volumetric Heat Transfer Coefficient

Equation (2.54) gives the volumetric interphase heat-transfer coefficient.

$$\alpha = \alpha_{sg} A_i \tag{2.54}$$

where α_{sg} is the heat transfer coefficient from solid-gas interaction which is shown in Equation (2.55). Moreover, A_i is the specific interfacial exchange area which is given in Equation (2.56).

$$\alpha_{gs} = \frac{\kappa_{g,0} Nu_p}{d_s} \tag{2.55}$$

$$A_i = \frac{6(1-\varepsilon_g)}{d_s} \tag{2.56}$$

Nusselt number for particle is indicated as $\mathrm{Nu_p}$, Gunn [62] proposed a Nusselt correlation for granular flows. This correlation is given in Equation (2.57).

$$Nu_p = (7 - 10\varepsilon_g + 5{\varepsilon_g}^2)\,(1 + 0.7{Re_s}^{0.2} + Pr^{\frac{1}{3}}) + \left(1.33 - 2.4\varepsilon_g + 1.2{\varepsilon_g}^2\right){Re_s}^{0.7} Pr^{\frac{1}{3}} \tag{2.57}$$

This correlation is only valid $Re_s < 5000$, and $0.35 < \varepsilon_g < 1$ conditions. Prandl number is also given in Equation (2.58). Additionally, solid Reynolds number, Re_s , is the same as Equation (2.11).

$$Pr = \frac{c_{p,s}\,\mu_g}{\kappa_{g,o}} \tag{2.59}$$

2.2.6. Discretization Techniques for Conservation Equations

In this section, discretization techniques are explained shortly without representing the formulation. Ansys Fluent uses a control volume technique, which allows all conversation equations to be converted to an algebraic equation on a control-volume basis. So, the three-conversation equation can be solved numerically. By default, the scalar discrete values of a control volume (cell) are stored at the cell centers of Ansys Fluent. These values include velocity, mass flux, pressure, and volume fraction values. However, face values are required for algebraic equations and must be calculated with interpolation from the cell center values. So, in the thesis, three different spatial discretization techniques were selected to calculate face values: first-order upwind scheme, second-order upwind scheme, and QUICK (Quadratic Upstream Interpolation for Convective Kinematics) scheme [46].

The first-order upwind scheme provides first-order accuracy. When selecting this scheme, the face value equals the cell's center value. Meanwhile, second-order accuracy is provided by the second-order upwind scheme. This scheme can be selected instead of the first-order scheme for higher-order accuracy. The cell face values are calculated using the cell-center value with a Taylor series expansion. Furthermore, QUICK schemes combine second-order upwind and central interpolation methods, providing third-order accuracy.

Meanwhile, PRESTO! (PREssure STaggering Option) is an interpolation scheme. Using PRESTO!, the cell face values are solved based on the cell-center values of the pressure in the discretization of the Momentum Equation. In Ansys Fluent, PRESTO! is offered as a default setting for the multiphase simulations. Discrete continuity balance is used to solve cell surface pressure for a staggered grid [46].

Furthermore, SIMPLE (Semi-Implicit Method for Pressure Linked Equations) algorithm is a Pressure-based solver algorithm. Therefore, it is used to solve numerically incomprehensible momentum equations, which are pressure-velocity coupling problems. So, this algorithm reproduces an equation for pressure from the momentum and continuity equations. It also provides a relationship between velocity and pressure field. Therefore, it is applied to Eulerian multiphase simulations for pressure-velocity coupling [46].

3. COLD BED VALIDATION STUDY

3.1. Validation Study of He *et al.*

He *et al*. conducted experiments in a conical cylindrical spouted bed [63, 64]. Their experimental results contain excessive data sets about the spouted bed hydrodynamic behavior. Therefore, their work became a benchmark for the validation of modeling studies including CFD-DEM and TFM. Significantly, many 2D axisymmetric modeling studies used He *et al.*'s experimental results to validate their computational results as given in Table *3.1*. In this thesis, the work of He *et al*. was utilized to evaluate performance of the TFM approach to examining the hydrodynamics characteristics in spouted beds.

Plexiglass was chosen as the external wall material for the test setup. Spherical glass beads filled the bed up to 0.325 m height from the inlet. The particle diameter is 1.41 mm. Moreover, the particle density is 2503 kg/m^3 [63, 64]. Figure 3.1 demonstrates a representative image of the bed dimensions and experimental setup.

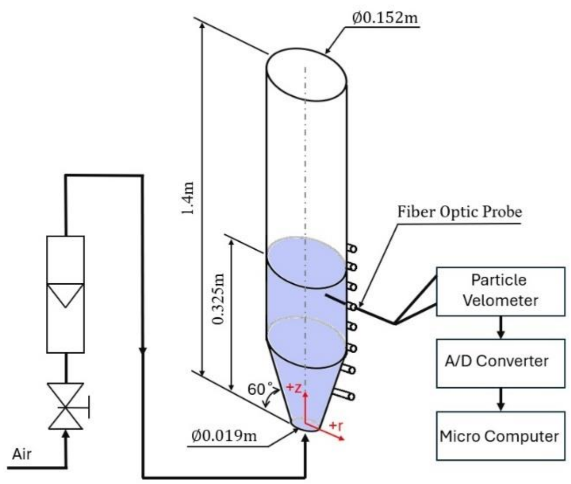

Gas Phase Properties	
Material	Air
Viscosity (*kg / (m s)*)	$1.79\text{x}10^{-5}$
Density (kg/m^3)	1.225

Solid Phase Properties	
Material	Glass Beads
Particle Diameter (*m*)	0.00141
Density (kg/m^3)	2503

Figure 3.1 A schematic view of He *et al.*'s experimental set-up [63, 64].

A fiber optic probe was used for measuring particle velocity and voidage. A velocity of 0.54 m/s was measured as the minimum spouting velocity (U_{ms}).Furthermore, the solid particle velocity and voidage were measured for three superficial velocities: U/U_{ms} = 1.1, $U/U_{ms} = 1.2$, and $U/U_{ms} = 1.3$. [63, 64].

Table 3.1 2D axisymmetric validation studies for He *et al.*'s experimental study.

References	Superficial Gas Velocity	Time Step (s)	Viscous Model	Scope of the Study
Du *et al.* [40]	U/U_{ms} = 1.3, 1.2, 1.1	1x10^{-3}, 2x10^{-3}	Turbulent	Investigation of different drag models.
Du *et al.* [50]	$U/U_{ms} = 1.3$	1x10^{-3}, 2x10^{-3}	Turbulence	Investigating the effects of different restitution coefficient, maximum packing limit and frictional stress.
Wang [65]	$U/U_{ms} = 1.3$	1x10^{-5}	Laminar	Investigating the effects of frictional stress and solid bulk viscosity. Also, proposing a correlation for particle velocity with Gidaspow drag model.
Zhonghua and Mujundar [66, 67]	$U/U_{ms} = 1.1$	N/A	Turbulent	Validating particle velocity and voidage only for Gidaspow drag model.
Bettaga [68]	$U/U_{ms} = 1.3$	1x10^{-4}, 1x10^{-3}	N/A	Validating particle velocity and voidage only for Gidaspow drag model.
Lule-Senturk [44]	$U/U_{ms} = 1.3$	5x10^{-4}	Laminar	Investigating the effects of different drag model correlations, different restitution coefficients, maximum packing limit and frictional stress. Also, proposing a correlation for particle velocity with Gidaspow and Syamlal O'Brien drag formulations.
Lan *et al.* [69]	$U/U_{ms} = 1.2$	1x10^{-4}	Turbulent	Investigating different wall specularity coefficients and restitution coefficients.
Hosseini *et al.* [48]	U/U_{ms} = 1.3, 1.2, 1.1	1x10^{-4}	Turbulent	Investigating different solid viscosity formulation for Du Plesis drag model. Also compared with different discretization schemes, algebraic, and full transport equation.
Reza *et al.* [70]	$U/U_{ms} = 1.3$	1x10^{-4}, 0.5x10^{-3}	Laminar, Turbulent	Comparing with laminar and turbulence model.
Wu *et al.* [71]	$U/U_{ms} = 1.3$	2x10^{-5}	Turbulent	Validating particle velocity and voidage only for Gidaspow drag model.
Shi *et al.* [72]	$U/U_{ms} = 1.3$	N/A	Laminar	Validating particle velocity and voidage only for Syamlal O'Brien drag formulations.

3.2. Initial and Boundary Condition

All simulations were carried out for $U/U_{mf} = 1.3$ as superficial gas velocity. Figure 3.2 gives the model dimensions, initial, and hydrodynamic boundary conditions.

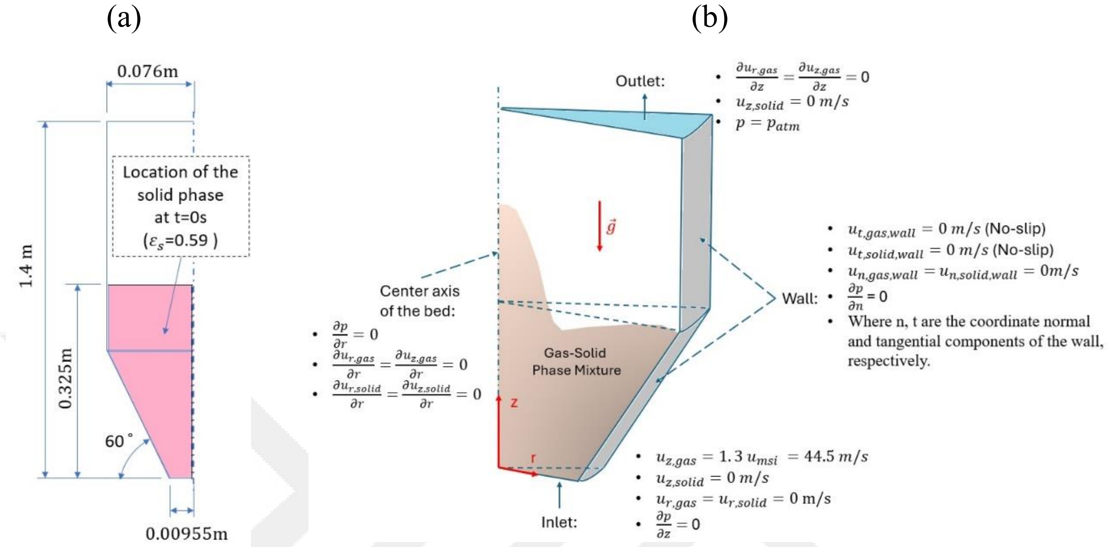

Figure 3.2 A representative image of the cold bed simulation model, a) Initial conditions and the model dimensions, b) Hydrodynamic boundary conditions.

Two Fluid Model (TFM) were used in all simulations and was implemented with Ansys Fluent 2022. The model is defined as 2D axisymmetric and transient. The solids phase parameters were determined using KTGF presented in the theory section. The simulations were carried out in real-time for 15 seconds. The results presented are the time-averaged values of last 5 s of the simulations with the data taken at 0.1 s intervals.

The flow is presumed to be laminar. Pressure based solver is selected. Meanwhile, pressure-velocity coupling scheme is defined as phase coupled SIMPLE algorithm. The momentum, volume fraction, and energy discretizations are selected as first-order upwind algorithm, whereas PRESTO! algorithm is defined for pressure discretization. The simulations were implemented using a constant time step of 0.0005 seconds. Each time step was solved in a maximum of 100 iterations. An under-relaxation factor of the solution controls is selected as 0.2 for pressure, momentum, granular temperature, volume fraction, and density. The convergence criterion is selected as the absolute error between two iterations. Scaled residual values of 10^{-3} are defined for the momentum and the continuity equations.

Moreover, when the first-order upwind algorithm is used, the solution quickly converges. However, the result is less accurate than the second-order upwind algorithm, for which the convergence is more difficult. It is thought that this difficulty arises from the transient nature of the simulations, especially at the beginning when the jet tries to penetrate through the bed before forming a stable spout. After a stable spout is formed and solid circulation is achieved in the bed, the bed operates in pseudo-steady state and convergence is easier. In the section of the cold bed validation study, the second-order upwind algorithm is not assigned in the simulated model. However, in the hot bed validation studies section, the effect of the second-order upwind algorithm is also investigated in the simulation models.

3.3. Mesh Independence Study

Three grid sizes were selected as coarse, medium, and fine for mesh independence study. Each grid size has a different discretized length in the r, and z directions. The discretized length decreases from coarse to fine sizes. Furthermore, the grid structure remains the same as in Lule-Senturk's work [44]. Nevertheless, the discretized lengths were selected arbitrarily. Their dimensions are given in Figure 3.3. The element shape of all sizes is quadrilateral. Syamlal O'Brien drag model was also selected for mesh independence studies. Moreover, He *et al.* indicated the packed limit of solid fraction was 0.59. Hence, the packing limit of the mesh study was set to equal He *et al.*'s packed limit. Table 3.2. represents other parameters of two fluid models that were used for the mesh independence study.

Radial distributions of the particle axial velocity and volume fraction were evaluated at 118 mm height from the inlet as measured in the experimental study. Figure 3.4 represents the results of the mesh independence studies. The results of the course mesh study follow a saw tooth shape. However, the results of the fine and medium mesh studies follow a smooth line, and they are close to each other compared to the coarse mesh study.

Furthermore, the bed pressure drop calculated for all three meshes are given in Table 3.3. As a result of the mesh study, the medium mesh setting is selected for the further investigation of the impacts of various drag models, restitution coefficient, and wall specularity coefficients on the simulation results.

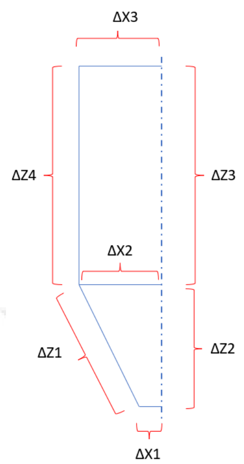

	ΔZ1 (mm)	ΔZ2 (mm)	ΔZ3, ΔZ4 (mm)	ΔX1 (mm)	ΔX2, ΔX3 (mm)
Coarse Mesh	1.872	1.62	1.6	0.203	1.617
Medium Mesh	1.156	1	1	0.126	1
Fine Mesh	0.869	0.752	0.75	0.095	0.752

	Total Element Number	Total Node Number
Coarse Mesh	40420	41328
Medium Mesh	106400	107877
Fine Mesh	188264	190230

Figure 3.3 Mesh settings for cold bed validation studies.

Table 3.2 Parameters of two fluid model for mesh independence study.

Gas-Solid Force Setup	Drag Coefficient:	Syamlal O'Brien
	Lift Coefficient:	-
	Virtual mass Coefficient:	-
Solid-Solid Force Setup	Restitution Coefficient:	0.95
	Granular Bulk Viscosity:	Lun *et al.*
	Granular Viscosity:	Syamlal-O'Brien
	Granular Temperature:	Algebraic
	Radial Distribution:	Lun *et al.*
	Frictional Viscosity:	-
	Solid Pressure:	Lun *et al.*
Packing Limit	0.59	

(a)

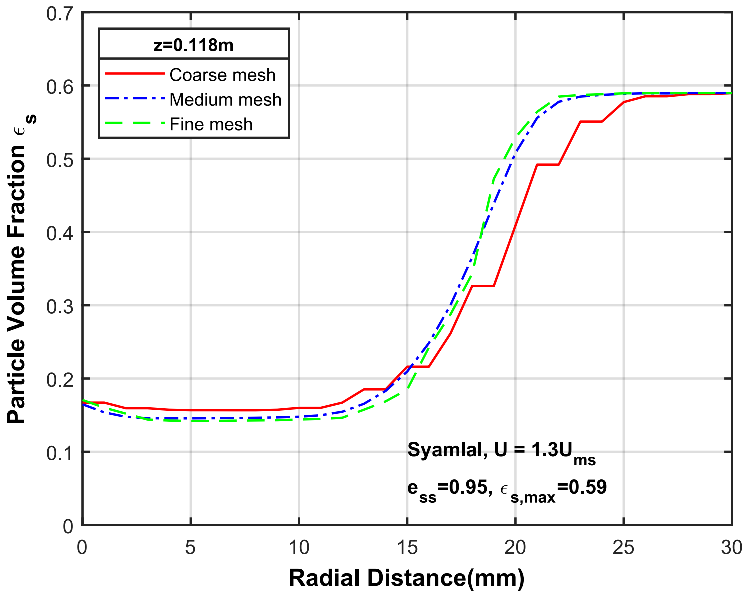

(b)

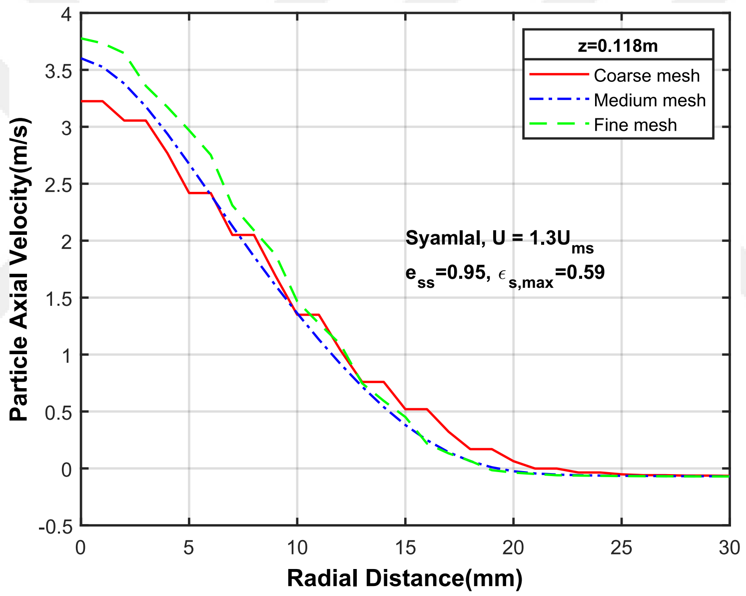

Figure 3.4 Comparison of different mesh size belonging to a) particle volume voidage and b) particle axial velocity.

Table 3.3 Results of the pressure drops for the mesh independence study.

	Fine Mesh	Medium Mesh	Coarse Mesh
Pressure Drop (Pa)	3439	3312	3191

3.4. Investigation of the Effects of Drag Models

In this section, the three fundamental gas-solid drag models evaluated in two-fluid simulations, Gidaspow, Wen-Yu, and Syamlal O'Brien drag models, are selected for comparative analysis to investigate their effects on the modeling results. Other parameters of two fluid models, which are defined in the mesh independence studies, are kept the same except for the drag model.

The solid volume fractions for different radial positions were evaluated at 53 mm, 118 mm, 168 mm, and 268 mm heights from the inlet, which were also measured in the experimental study. At z = 53 mm, the results of the solid volume fraction of all three drag models are close to the results of the experiment in the spout region. Additionally, the spout region for He *et al.*'s experimental data set can be defined between r = 0 to r = 20 mm at z = 53 mm. However, the spout diameters of all three drag models are approximately 25% smaller than the experiment. At z = 118 mm, the particle volume fraction increases proximate to the central axis of the bed in the simulations. When the height increases, the predicted volume fractions overestimate the experimental data and turn into a characteristic shape like a hook. The hook shape is observed more clearly near the spout axis for the drag formulations of Wen-Yu and Syamlal O'Brien at z = 168 mm and z = 268 mm. Except for the hook shape, the results of the Wen-Yu and Syamlal O'Brien drag formulations are more proximate to the test results at z = 118 mm and 268 mm. However, at z = 168 mm, the spout diameters of the drag formulations of Wen-Yu and Syamlal O'Brien are approximately 10% larger than the experiment. Yet, the Gidaspow drag model results are the least accurate predictions since spouting does not occur when this model is used. Apparently, Gidaspow drag model does not create sufficient drag force to produce a spout at the given operating velocity. Figure 3.5 represents the performance of various drag models on particles for diverse bed heights.

The results belonging to the particle axial velocity on radial distances at different heights are given in Figure 3.6. The axial particle velocity for different radial positions were evaluated at 53 mm, 118 mm, 168 mm, and 268 mm heights from the inlet. At z = 53 mm, the experimental results of particle velocity are almost twice as high as those of all three drag models. With increasing the height, the results of the drag models approach the experimental results. Also, the difference in the drag forces of all three drag models is observed more clearly at z = 168 mm and 268 mm. The model regarding Syamlal O'Brien produces more drag forces than the Wen-Yu and Gidaspow drag formulations. Hence, the Syamlal O'Brien drag formulation provides the nearest result to the experimental data at z = 168 mm and 268 mm. In contrast, the Gidaspow drag formulation results in huge discrepancies.

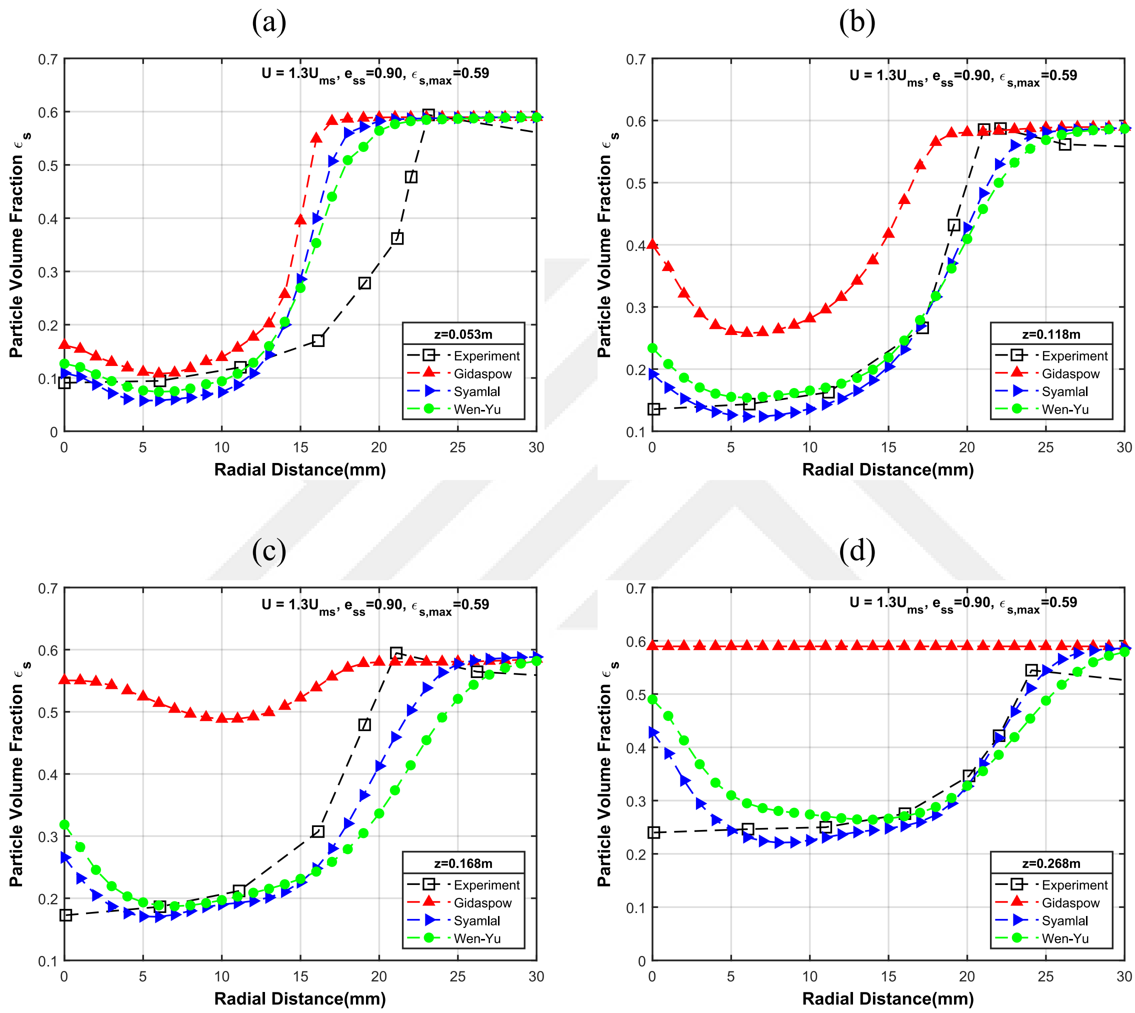

Figure 3.5 Radial distribution of particle volume fraction for various drag formulations a) z = 0.053 m, b) z = 0.118 m, c) z = 0.168 m, d) z = 0.268 m.

Moreover, the simulations were compared with other studies which used Gidaspow drag model at z = 118 mm in Figure 3.7. The external spout does not also occur in Lule-Senturk's work [44], like in the current study. Therefore, Lule-Senturk's work and the current simulation incorrectly estimate the fraction of the solid volume for the spout region. However, the external spout was observed in the research of Wu *et al.* [71] and Du *et al.* [40]. Hence, their particle axial velocity results are closer to the experiment results than Lule-Senturk and the current simulation, but they still underpredict the experimental results approximately by 59%.

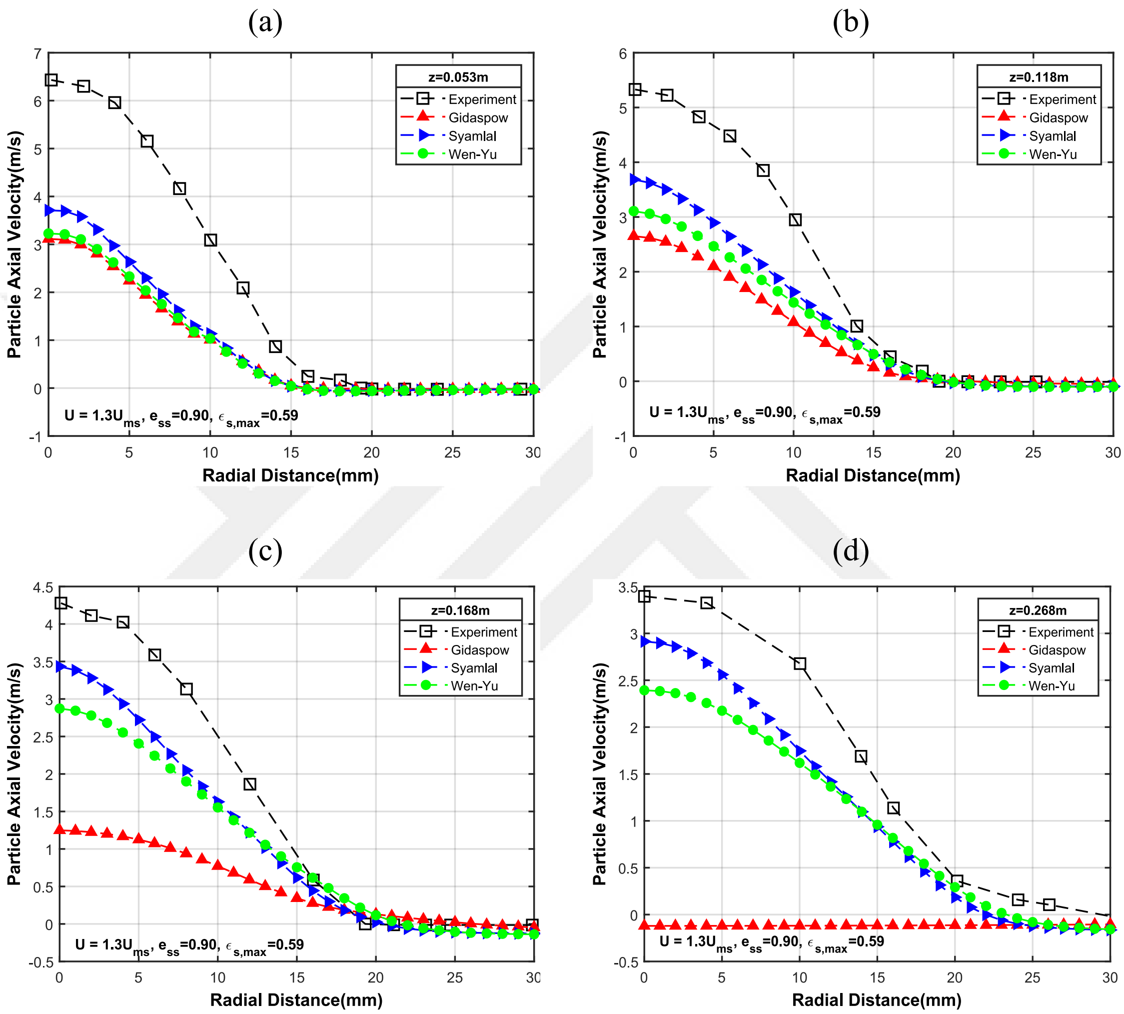

Figure 3.6 Examination of the effects of various drag models on radial distribution of particle axial velocity, and a) z = 0.053 m, b) z = 0.118 m, c) z = 0.168 m, d) z = 0.268 m.

Additionally, Figure 3.8 and Figure 3.9 demonstrate that the simulations were compared with other studies that used the Syamlal O'Brien drag model at z = 118 mm and 168 mm. The hook problem exists at the height of 118 mm, but it is not pronounced. However, at the height of 168 mm, the problem is clearly observed in other studies. The axial particle velocity predictions in the literature studies underestimate the experimental data by approximately 50%, similar to the findings of this work when the Syamlal O'Brien formulation is selected as a drag model.

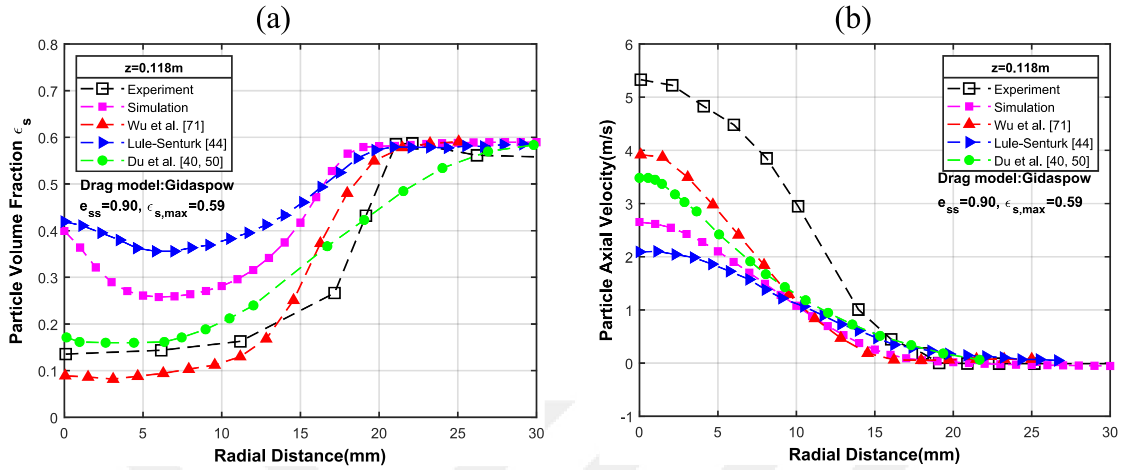

Figure 3.7 Comparison with other studies in the literature for radial distributions of a) particle volume concentration and b) axial velocity at z = 118 mm for the Gidaspow drag model.

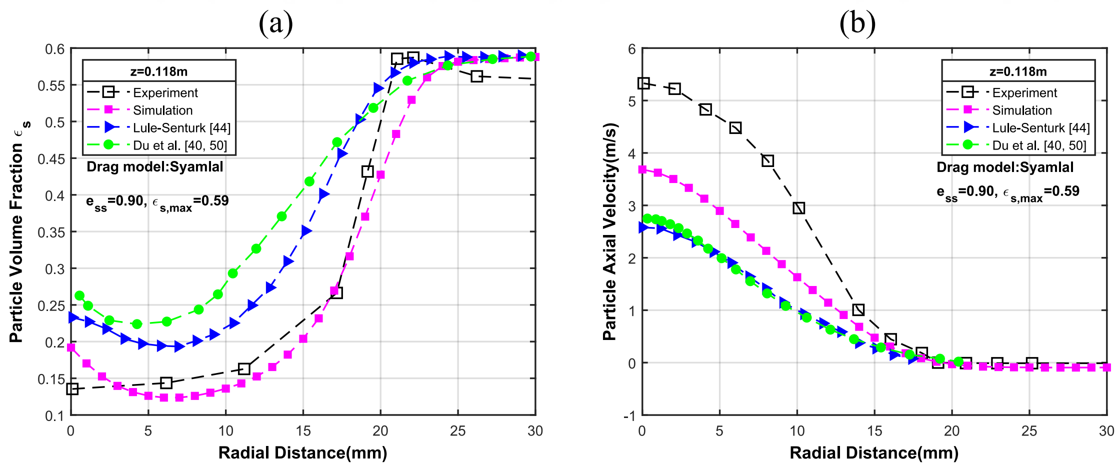

Figure 3.8 Comparison with other studies in the literature for radial distributions of a) particle volume fraction and b) axial velocity at z = 118 mm for the Syamlal O'Brien drag formulation.

Figure 3.10 represents the contour images belonging to the solid phase volume concentration after the simulation has ended (t = 15 s) for three various drag models. In summary, Syamlal O'Brien produces more drag force than other drag models. Therefore, the particle axial velocity and the fountain height can be observed to be higher than the others. The Wen-Yu model produces enough drag force to produce the fountain, although it is less than Syamlal O'Brien's model. Hence, the fountain height of Wen-Yu is 0.1m less than the Syamlal O'Brien Model. Meanwhile, enough drag force to create external spout and fountain is not produced for the Gidaspow drag model. This result is distinctly demonstrated in Figure 3.10.

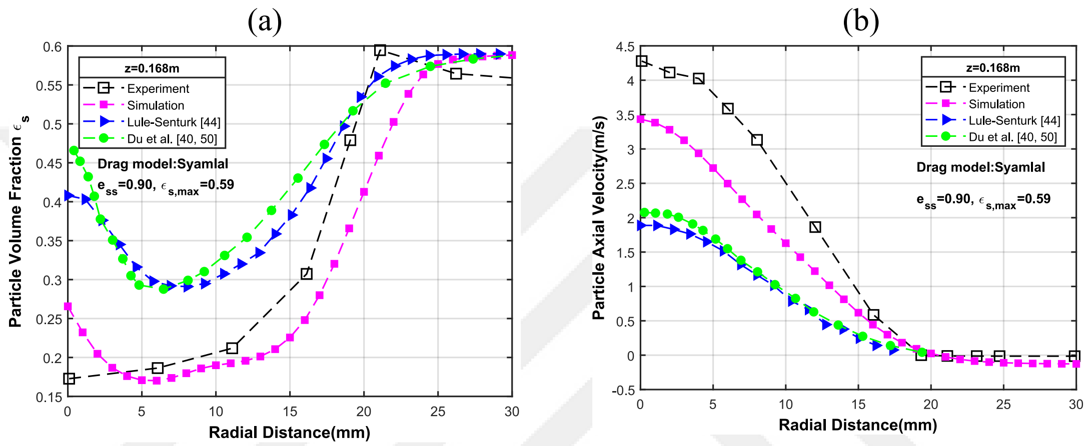

Figure 3.9 Comparison with other studies in the literature for radial distributions of a) particle volumetric fraction and b) axial velocity at z = 168 mm for the Syamlal O'Brien drag formulation.

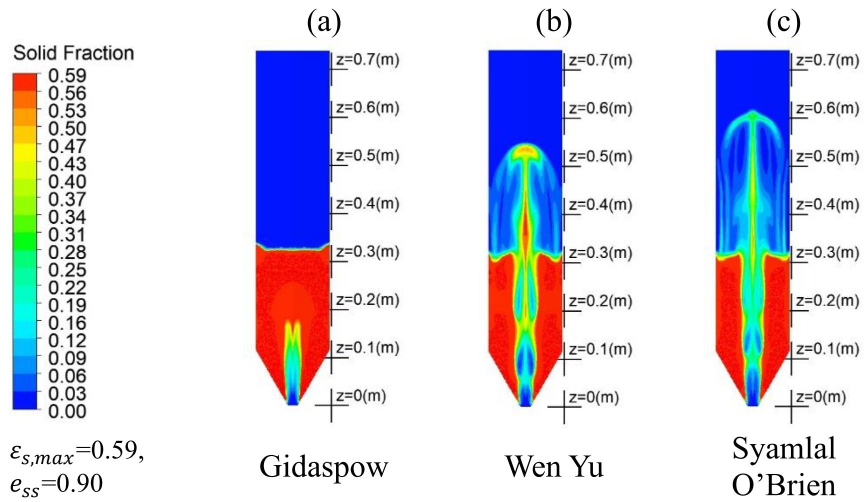

Figure 3.10 Contour images at 15s of the volume fractions of the solid phase for various drag models.

3.5. Investigation of the Effects of Restitution Coefficients

The restitution coefficient is presented within the theory section. It indicates the elasticity ratio after two particles collide. A perfectly elastic collision occurs, when the restitution coefficient is equal to 1. Meanwhile, a perfectly inelastic collision, which means particles stick together, occurs when it is equal to 0. The effects of the restitution coefficient on the spouted bed hydrodynamics are examined in this section. As a first step, three different coefficients are selected as 0.8, 0.9, and 0.95, which is the typical range for the particles used in fluidized and spouted beds. Except for the restitution coefficient, other parameters of the model are kept the same. As a next step, simulations were carried out with different drag models as well as these three different coefficients.

Figure 3.11 and Figure 3.12 demonstrate the simulation outputs related to the particle's volume fraction and axial velocity, which were carried out in the first step, respectively. Although different restitution coefficients are used, the solids volume fraction at the spout axis is still overestimated, especially at higher axial locations, such as z = 168 mm (Figure 3.11c) and 268 mm (Figure 3.11d). This problem is also mentioned in Section 3.1.3. On the positive side, the solid volume fractions are similar to the experiment's results when one moves away radially from the spout axis. Generally, no distinct impacts of the restitution coefficient upon the particle volume fractions are observed.

The particle axial velocity increases significantly at higher axial locations using lower restitution coefficients, such as 0.8. This result can observe clearly in Figure 3.12c and Figure 3.12d. Despite using the Syamlal O'Brien drag formulation, the solved axial velocity values are about 15% lower than the measurement outputs. Therefore, the effects of the different restitution coefficient with different drag models are examined as the next step.

The reversal of the particle axial velocity direction is usually considered as the boundary/interface between the annulus and the spout. This boundary is also equal to the spout diameter. So, the different drag models and the different restitution coefficients were evaluated against each other using the experimentally measured spout diameter. Figure 3.13 shows the modeling and experimental results. Consequently, the outputs of e_{ss} = 0.95 with the Wen-Yu and Syamlal O'Brien drag formulations are observed similar results to the experimental. On the other hand, the Gidaspow drag model does not predict any spout at z = 268 mm because only the internal spout is formed, as shown in Figure 3.10.

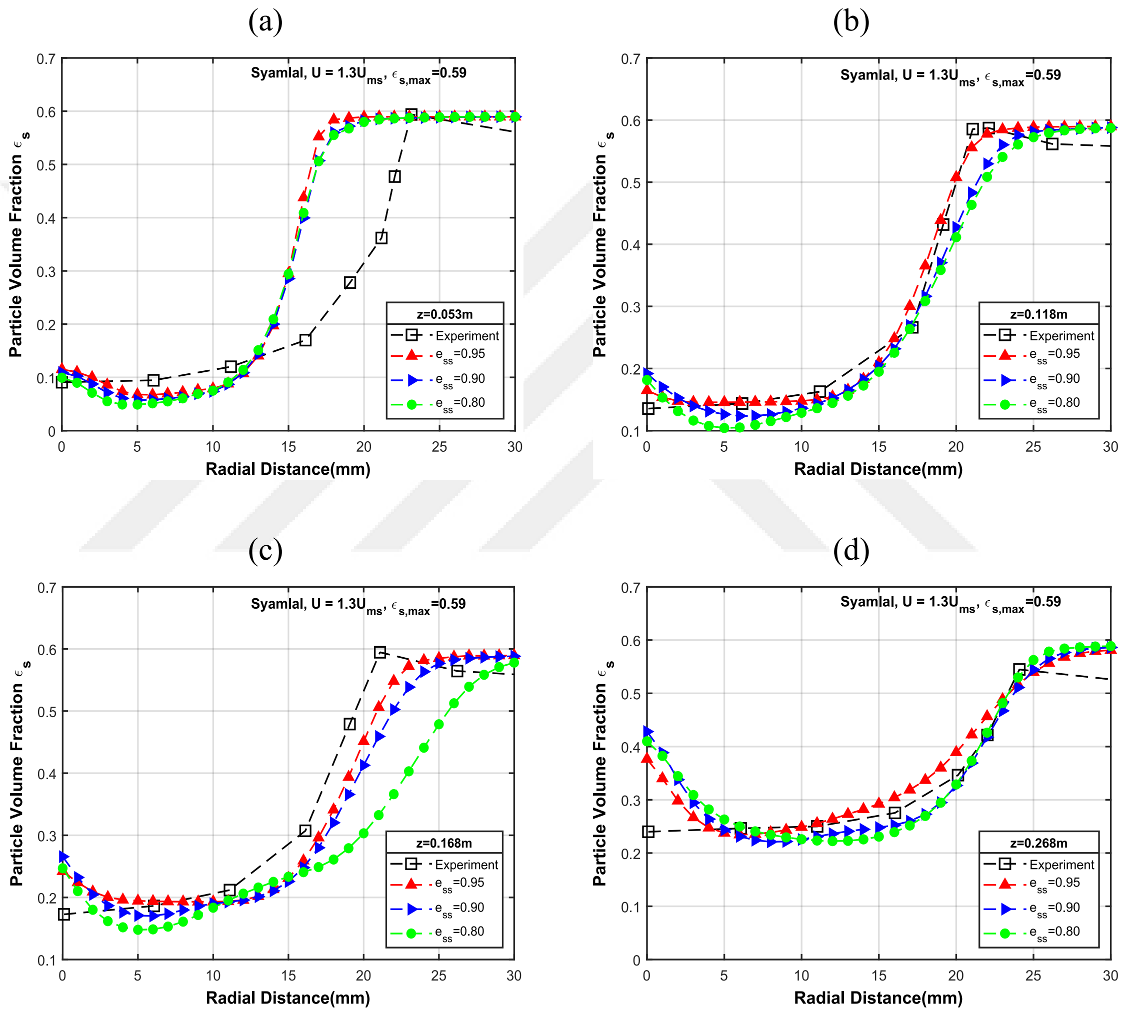

Figure 3.11 Comparison of the effects of various restitution coefficient values on the radial distribution of the particle volume fraction using the Syamlal O'Brien model, $\varepsilon_{s,max}$= 0.59 and a) z = 0.053 m, b) z = 0.118 m, c) z = 0.168 m, d) z = 0.268 m.

He *et al.* also presented the particle velocity results at the central axis of the bed in the fountain region, which can be used for cold bed validation studies. Therefore, the modeling results for the various drag models coupled with the different coefficients of restitution are examined using experimental data, and Figure 3.14 represents the results. From the inlet to the height of 150 mm, all drag models underestimate the particle velocity at the axis. After z= 0.15 m, the drag formulation developed by Syamlal O'Brien, in particular, led to near-matching results with the measurement outputs in the spouted bed and the fountain region. The fountain heights are also accurately predicted with this drag model. The restitution parameter affects not only the fountain height but also the particle velocity prediction in the fountain. The results with e_{ss} = 0.80 are slightly better with the experimental data than other simulation outputs.

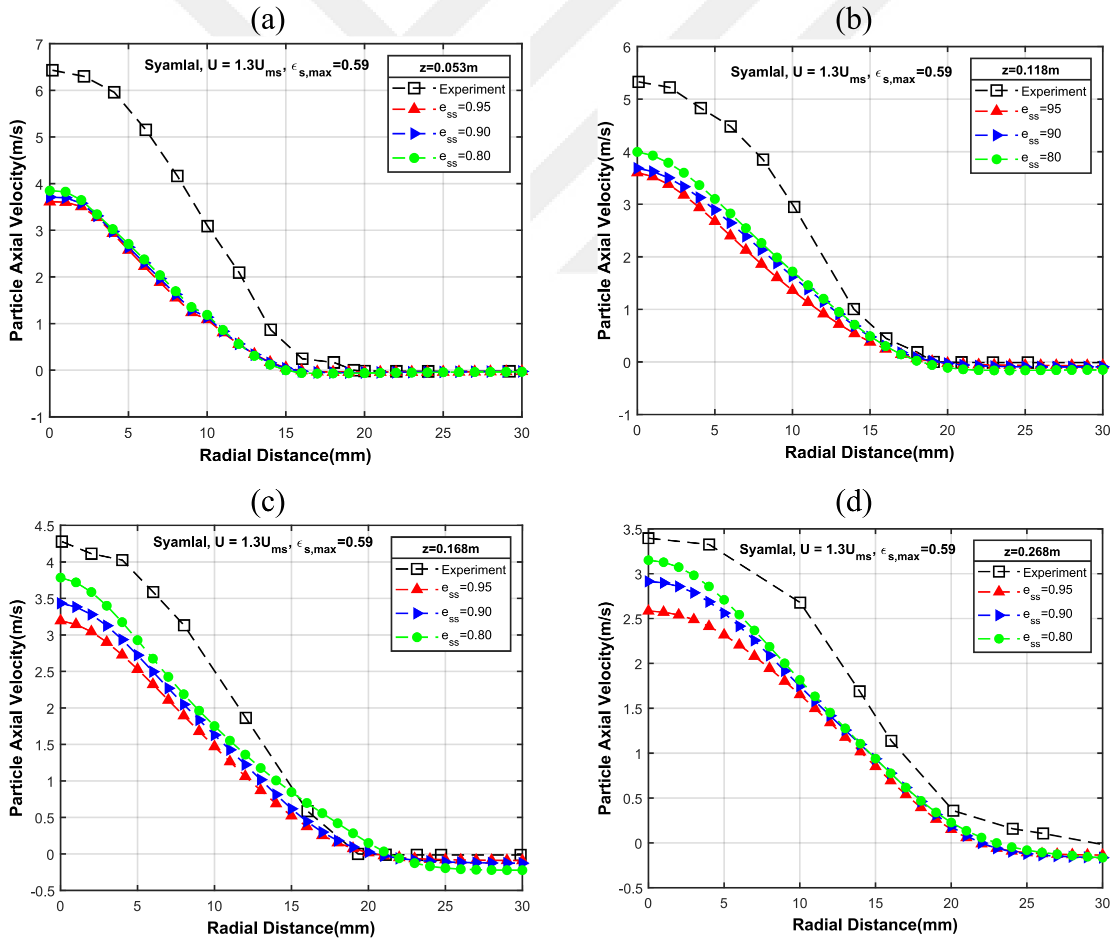

Figure 3.12 Comparison of the effects of various restitution parameter*s* on the distribution in the radial direction of the axial component of particle velocity using the Syamlal O'Brien drag model, $\varepsilon_{s,max}$= 0.59 and a) z = 0.053 m, b) z = 0.118 m, c) z = 0.168 m, d) z = 0.268 m.

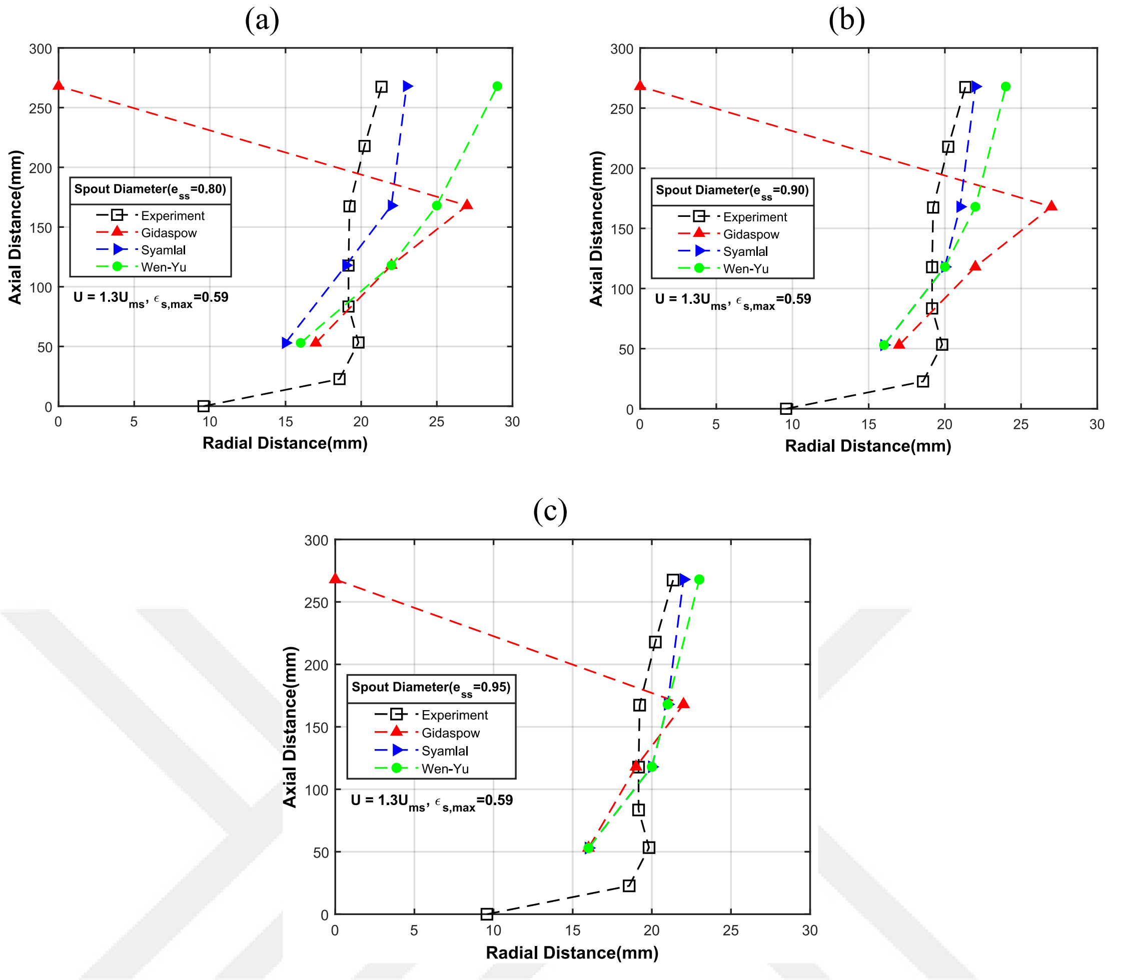

Figure 3.13 Examination of spout diameters of various drag models for $\varepsilon_{s,max}$ = 0.59, and a) e_{ss} = 0.80, b) e_{ss} = 0.90, c) e_{ss} = 0.95.

Figure 3.15 represents the contour images of the particle volumetric fraction after the simulation has ended (t = 15 s) for the Gidaspow drag model and various restitution coefficients. Similar contour images for Wen-Yu and Syamlal O'Brien are shown in Figure 3.16, and Figure 3.17, respectively. Disregarding the Gidaspow model for which no spouting is observed, for the drag models proposed by Wen-Yu and Syamlal O'Brien, the height of the fountain diminishes as the coefficient of restitution increases. The axial component of particle velocity at the spout axis was also shown to decline with increasing coefficient of restitution. This can be clarified by the granular kinetic theory. A higher coefficient of restitution indicates more elastic collisions, less energy loss in the particle collisions and hence higher granular temperature. A higher granular temperature results in more interactions between the particles leading to higher solids phase viscosity. Solid phase velocities tend to decrease as the solids phase viscosity increases.

(a)

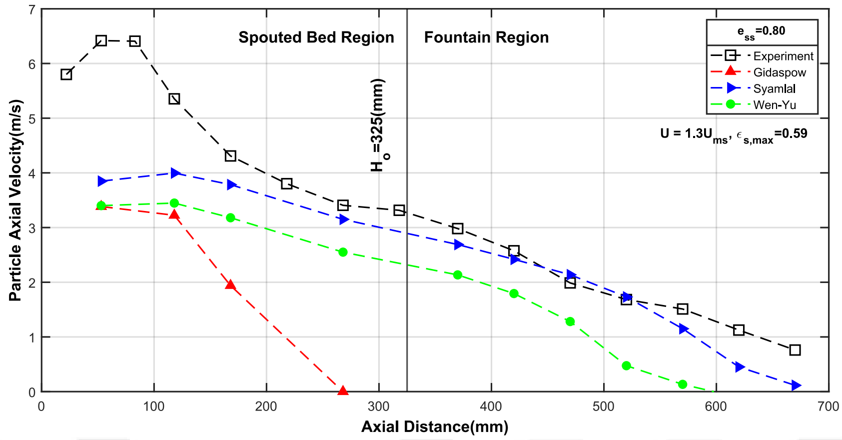

(b)

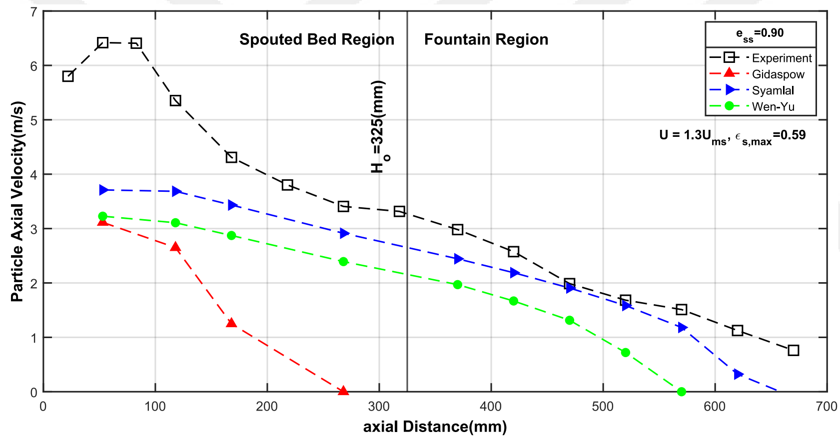

(c)

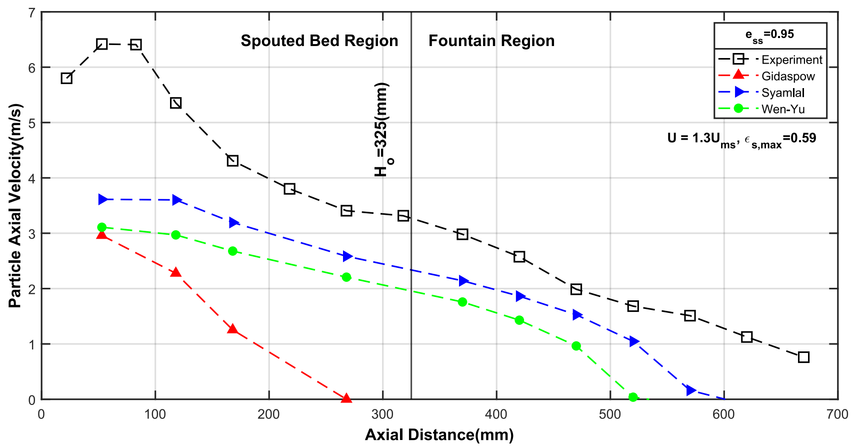

Figure 3.14 Impacts of various drag models on axial variations of particle axial velocity at the spout axis for $\varepsilon_{s,max}$= 0.59, r = 0 m, and a) e_{ss} = 0.80, b) e_{ss} = 0.90, c) e_{ss} = 0.95.

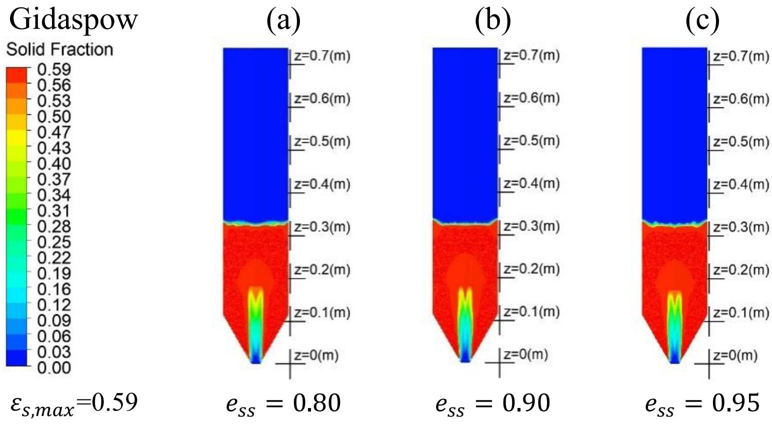

Figure 3.15 Contour images of particle volume fraction at t = 15 s for the Gidaspow drag model, $\varepsilon_{s,max}$= 0.59, and a) e_{ss} = 0.80, b) e_{ss} = 0.90, c) e_{ss} = 0.95.

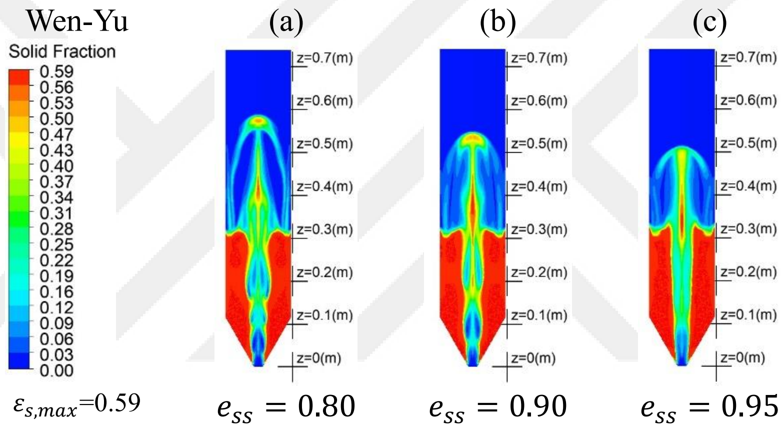

Figure 3.16 Contour images of particle volume fraction at t = 15 s for the Wen-Yu drag model, $\varepsilon_{s,max}$= 0.59, and a) e_{ss} = 0.80, b) e_{ss} = 0.90, c) e_{ss} = 0.95.

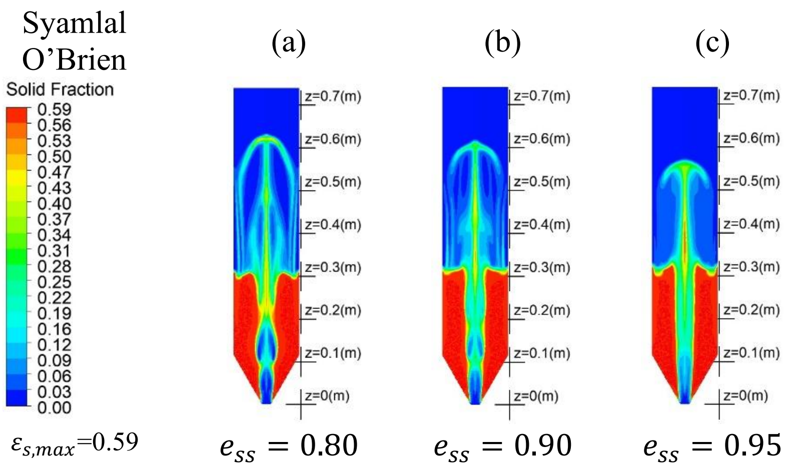

Figure 3.17 Contour images of particle volume concentration at t = 15 s for the Syamlal O'Brien drag formulation, $\varepsilon_{s,max}$= 0.59, and a) e_{ss} = 0.80, b) e_{ss} = 0.90, c) e_{ss} = 0.95.

Figure 3.18 demonstrates the examination of the axial variation of the particle velocity at the central axis. Meanwhile, the study of Shi *et al.* [72] for two different restitution coefficients using the drag formulation proposed by Syamlal O'Brien is shown in the same figure. As seen in Figure 3.18, the results for e_{ss}=0.95 are consistent with the results of this work. However, the results for e_{ss}=0.90 are less consistent. It is not clear why a packing limit of 0.61 was used by Shi et al. although He *et al*. reported the packing limit as 0.59. However, it is interesting to note that using a packing limit of 0.61 results in better predictions for both e_{ss}=0.90 and 0.95.

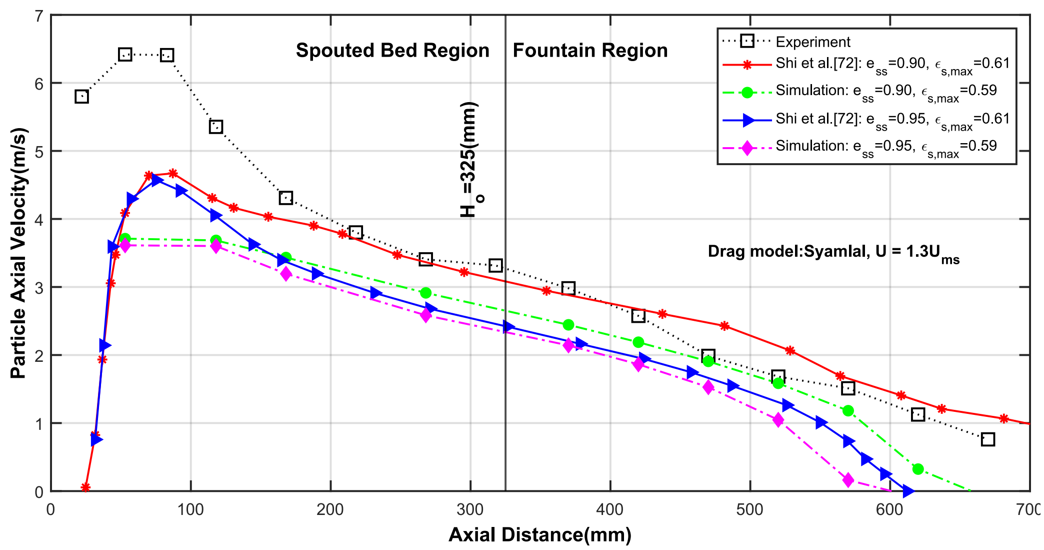

Figure 3.18 Comparison with other studies in the literature for the axial variation of the particle velocity at the spout axis for various restitution coefficients and Syamlal O'Brien drag formulation.

3.6. Investigation of Effects of Wall Specularity Coefficient

The specularity coefficient is presented in the theory section. It indicates the tangential momentum ratio due to the particle-to-wall friction. No friction is observed between the particles and the wall when φ equals 0. Hence, the tangential momentum loss is zero. Furthermore, the particle slips on the wall with no shearing resistance. Conversely, when φ equals 1, the particle-to-wall shearing resistance is the highest value, and the particles stick to the wall. It is almost similar to the no-slip condition. When the specularity coefficient increases, the wall shear stress on the particles increases. In this section, four different coefficients are selected as 0.0, 0.05, 0.2, and 1.0 to investigate the effects of the wall specularity. Other parameters of two fluid models, which are defined in the mesh independence studies, are kept the same.

Figure 3.19 and Figure 3.20 give the simulation findings of particle volume concentration and the axial component of particle velocity for different heights, respectively. According to the results, using the different specularity coefficients does not significantly change the particle volume concentration and axial velocity. The volume concentration of particles of φ = 0 is slightly higher than φ = 1.

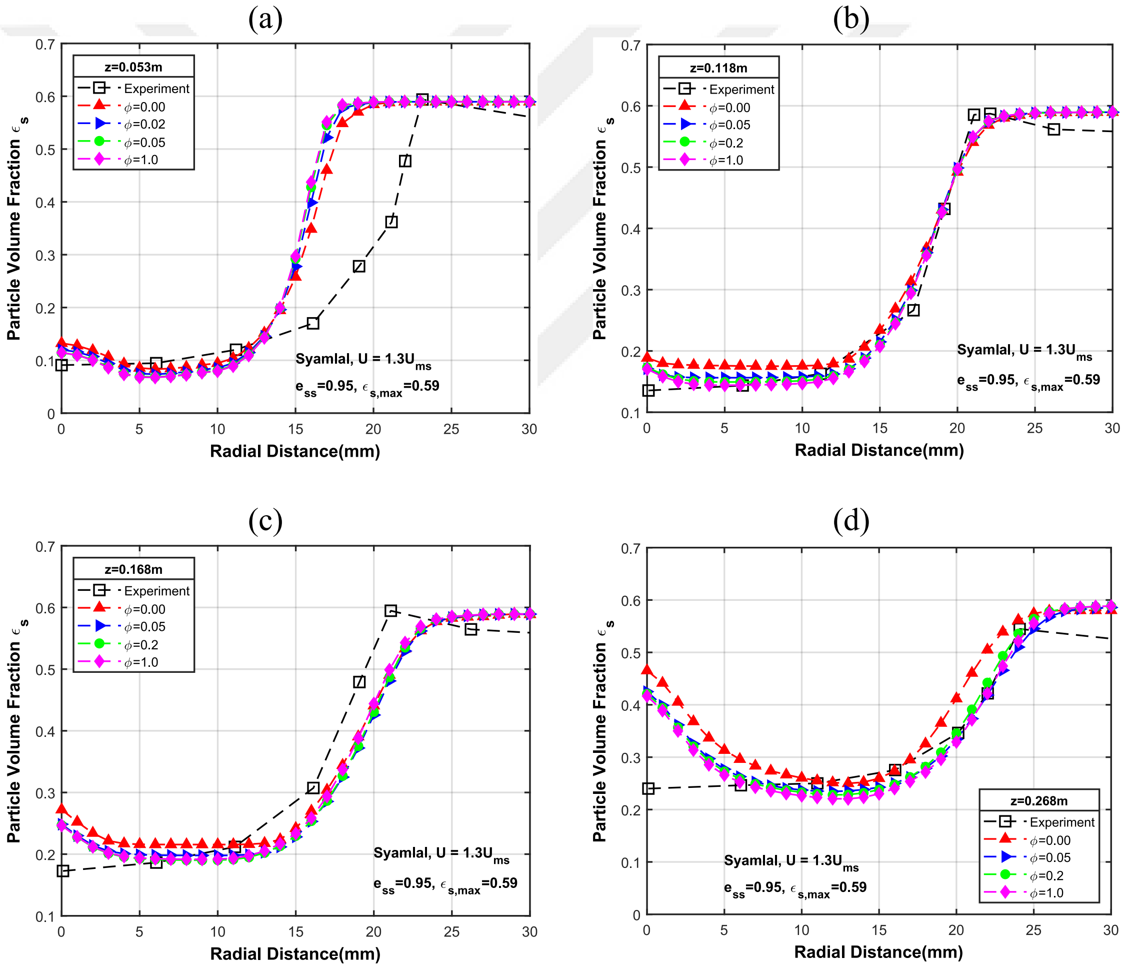

Figure 3.19 Comparison of various wall specularity coefficients on radial distributions of particle volume fraction for the Syamlal O'Brien drag model, $\varepsilon_{s,max}$ = 0.59, e_{ss} = 0.95, and a) z = 0.053 m, b) z = 0.118 m, c) z = 0.168 m, d) z = 0.268 m.

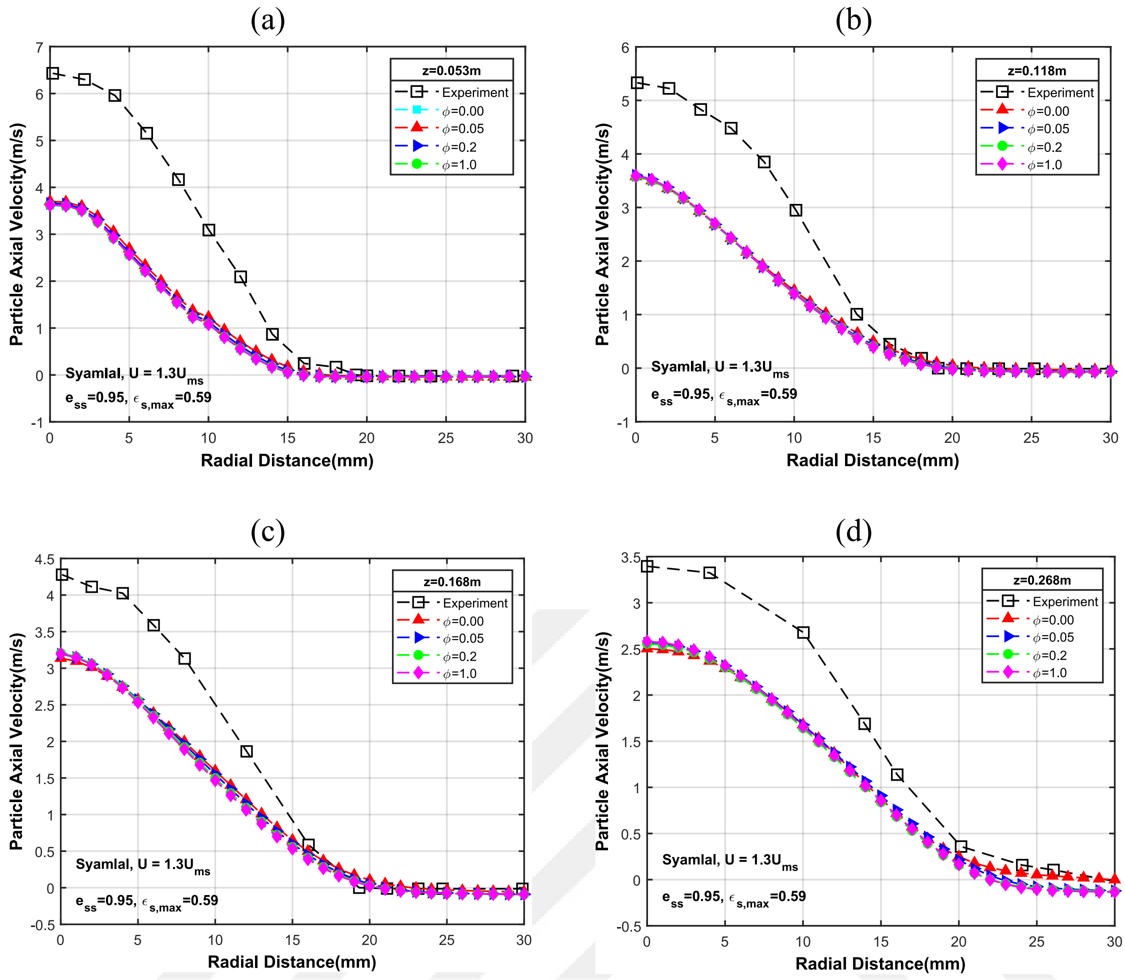

Figure 3.20 Comparison of various wall specularity coefficient on radial distributions of particle axial velocity for the Syamlal O'Brien drag model, $\varepsilon_{s,max}$ = 0.59, e_{ss} = 0.95, and a) z = 0.053 m, b) z = 0.118 m, c) z = 0.168 m, d) z = 0.268 m.

The actual effects of different specularity coefficients on the particle axial velocity near the wall are represented in Figure 3.21Figure *3.20*. According to the results, the highest particle axial velocity near the wall is observed for φ = 0. Furthermore, when the coefficient increases to φ = 1, the particle axial velocity almost shows no movement. However, the hydrodynamic effects due to the differences in the particle axial velocities adjacent to the wall are insignificant in the spouted bed. Moreover, contour images at end of the simulation (t= 15 s) are given in Figure 3.22 for different wall specularity coefficients where only slight differences are observed.

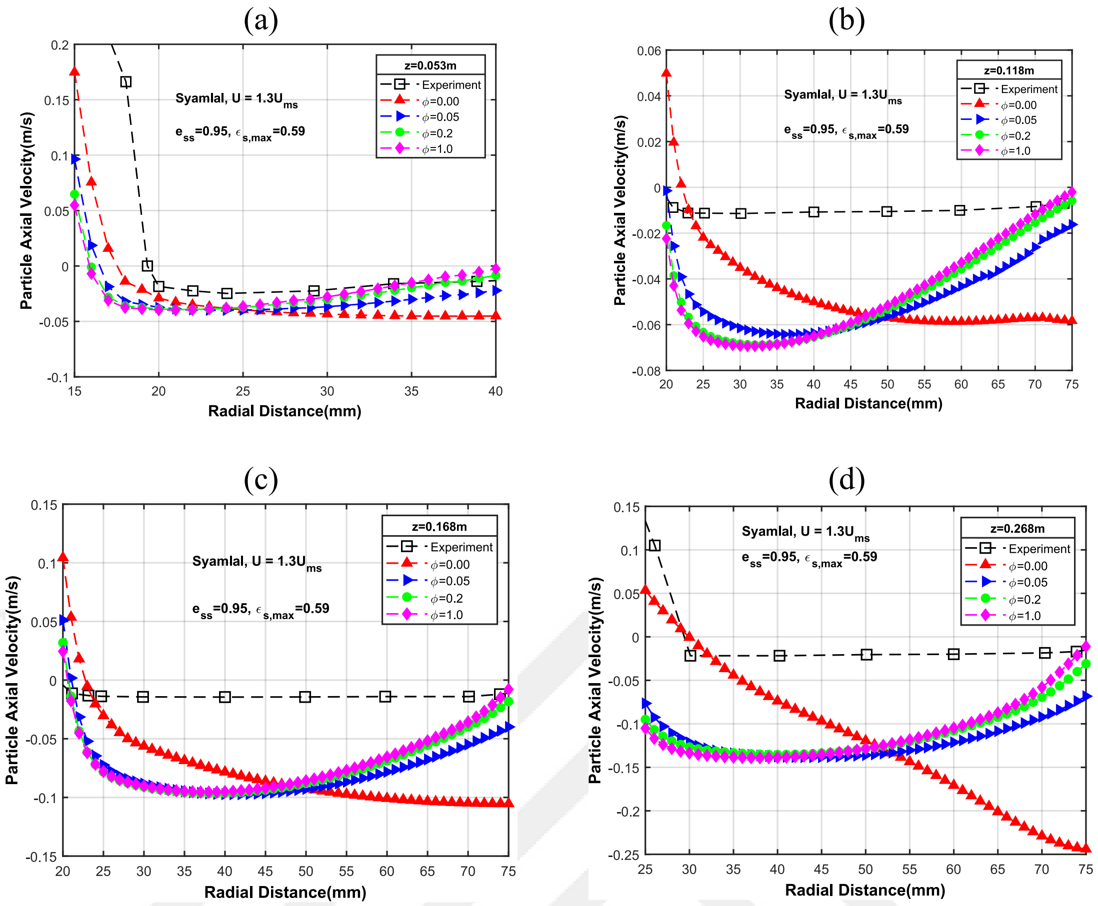

Figure 3.21 Comparison of various specularity coefficient on particle axial velocity near the wall for the drag formulation proposed by Syamlal O'Brien, $\varepsilon_{s,max}$ = 0.59, e_{ss} = 0.95, and a) z = 0.053 m, b) z = 0.118 m, c) z = 0.168 m, d) z = 0.268 m.

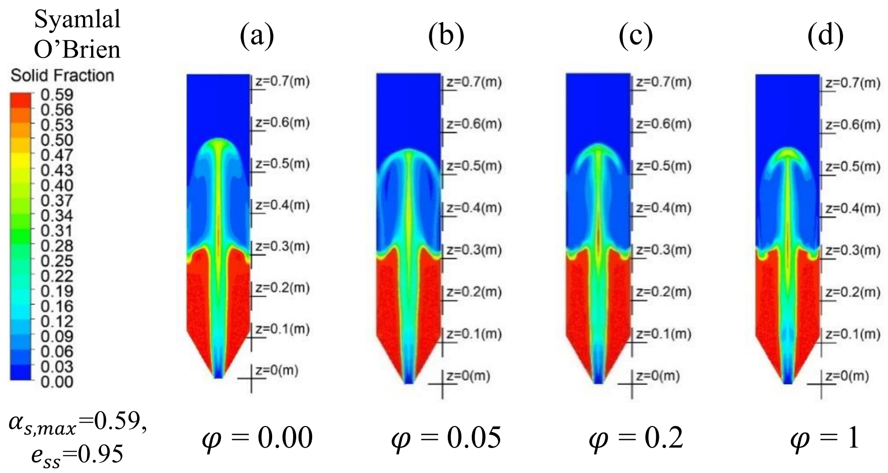

Figure 3.22 Contour images of particle volume concentration at t = 15 s for the drag formulation proposed by Syamlal O'Brien, $\varepsilon_{s,max}$= 0.59, e_{ss}= 0.90, and a) φ = 0.00, b) φ = 0.05, c) φ = 0.2, d) φ = 1.00.

Additionally, Table 3.4 and Table 3.5 show the pressure drops for all modelling cases that were completed and presented in this section. Their results are compared with He *et al.* experimental results.

Table 3.4 Results of the pressure drops for different drag models and restitution coefficients.

Drag Model	Restitution Coefficient		
	e_{ss} = 0.95	e_{ss} = 0.90	e_{ss} = 0.80
Gidaspow	3332 Pa	3382 Pa	3411 Pa
Wen-Yu	3353 Pa	3467 Pa	3581 Pa
Syamlal O'Brien	3312 Pa	3350 Pa	3424 Pa
Experimental Result [63, 64]	3000 Pa		

Table 3.5 Results of the pressure drops for the various restitution coefficients and drag models.

Drag Model	Wall Specularity Coefficient (e_{ss} = 0.95)			
	φ = 0.00	φ = 0.05	φ = 0.2	φ = 1.0
Syamlal O'Brien	3925 Pa	3459 Pa	3357 Pa	3309 Pa
Experimental Result [63, 64]	3000 Pa			

3.7. Conclusions According to Experimental Data of He *et al.*

Different measurement parameters should be examined to fully understand the hydrodynamic properties of a spouted bed. These parameters are the fountain height, the particle volume fraction and axial velocity in the annulus and spout regions, the bed pressure drop, and the spout diameter. Furthermore, they can be predicted using the TFM approach. Therefore, these parameters were used to validate the cold bed simulation model in the thesis. He *et al*'s study gives excessive experimental data sets for the hydrodynamics characteristics of a laboratory scale spouted bed, more details than any experimental study in the literature. Moreover, most TFM validation studies on the spouted beds referred to He *et al*.'s data sets for comparison and validation. Moreover, most TFM validation studies on the spouted beds referred to He *et al*.'s data sets for comparison and validation. The simulation findings are investigated in detail to determine the corresponding effects based on three main parameters: the wall specularity coefficient, drag model and restitution coefficient.

The following conclusions are reached in this chapter by comparing the simulation findings with He *et al*.'s experimental data set:

- Among the drag models tested (Syamlal O'Brien, Gidaspow and Wen-Yu drag models), no external spout and fountain are observed when Gidaspow model was used. Gidaspow model was not able to produce sufficient drag force at the given operating velocity.
- Generally, Syamlal O'Brien drag model produced better predictions for the radial distribution belonging to the axial component of particle velocity, the spout diameter and the volume fraction of particle.
- A peculiar 'hook-like' shape was observed at the spout axis for the solids volume fraction especially at higher bed heights. This shape was also observed in other TFM studies in the literature.
- One of the main inconsistent results of TFM is that the particle volume fraction is overestimated near the spout axis regardless of the drag model used, especially the problem is seen more clearly at the higher axial heights.
- Generally, the volume fraction of solid in the annulus domain always has a lower value than the maximum packing limit. However, the results of TFM do not observe any changes and are always seen as the maximum packing limit.
- Up to the height of 150 mm from the inlet, the experimental axial particle velocities are almost twice as much the simulated values for all drag models. However, Wang [65] stated that the particle axial velocity values might have been inaccurate due to systematic errors in the fiber optic measurements. So, Wang proposed a correlation for the particle velocity. Also, Lule-Senturk [44] also found similar results and proposed another correlation that is similar predictions to Wang's.
- The axial particle velocity and fountain height decrease with increasing coefficient of restitution. This is attributed to more elastic collisions with less energy loss leading

to higher granular temperature values. As the granular temperature – which indicates the particles collisional kinetic energy – increases, so does the solid phase viscosity leading to lower axial particles velocities and fountain height.

- The wall specularity coefficient influences the particle velocities near the wall but does not impact the overall gas-solid motion.

4. HOT FLUIDIZED BED VALIDATION STUDY - I

4.1. Validation Study of Patil's Experiment

Patil *et al.* [39] experimentally investigated transient solid phase cooling characteristics for a 2D pseudo-fluidized bed. They used different inlet velocities, bed weights, and particle diameters to investigate the convective cooling behaviour. Hence, they provided an excessive data set about solid-phase cooling. Although many CFD-DEM modeling studies used these data sets for validation, there are only two TFM modeling papers using Patil *et al's* data set for validation modelling [73, 74]. In these studies, the details of the TFM modelling and implementation were not adequately presented. This thesis uses Patil's experimental data sets to explore and investigate the predicting capability of TFM for convective cooling of fluidized beds.

Figure 4.1 indicates a representative image of the experimental set-up of Patil *et al.* and the properties of particles and fluidizing gas used in their experiments. Their fluidized bed dimensions have height, width, and depth of 250 mm, 80 mm, and 15mm, respectively. The front of the bed was made of sapphire glass, which helps to observe particle movement and temperature in the bed. Hence, they used a standard camera to measure solid volume fraction and velocities. Additionally, they used a thermal camera to measure particle temperatures. In contrast, the sides and back walls were made of aluminium plates. However, the thicknesses of aluminium and glass walls were not available in their paper. The outside wall temperature was 20 °C.

They used nitrogen gases to fluidize the bed. The gas enters from the bed's bottom with three different superficial gas velocities: 1.2 m/s, 1.54 m/s, and 1.71 m/s. Besides, a small nozzle was positioned at the bottom center. The nozzle which the 10% of the bottom area was not operated and acts like a zone where there is no gas flow.

Spherical glass beads were filled in the bed. Their diameter is 1mm. Their density has also 2500 kg/m^3. The experiments were conducted at two different bed material mass: 75 gr and 125 gr. The bed heights were determined from the mass of the particles using particle density and the packed bed voidage values.

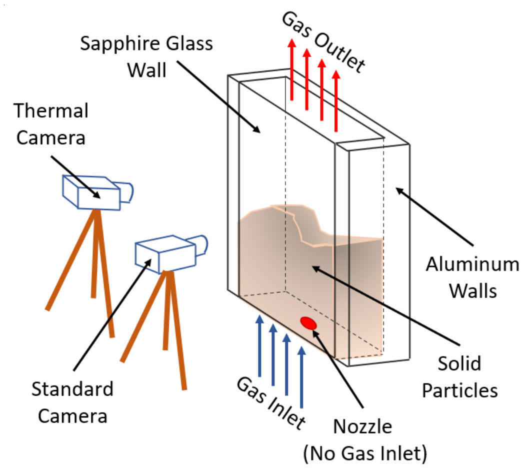

Gas Phase Properties	
Material	Nitrogen
Viscosity $(kg/(m\ s))$	$2.0\text{x}10^{-5}$
Density (kg/m^3)	1.225
Thermal conductivity (W/m K)	0.025
Heat capacity $(J/kg\ K)$	1006

Solid Phase Properties	
Material	Glass Bead
Density (kg/m^3)	2500
Particle Diameter (m)	0.001
Thermal conductivity (W/m K)	1.4
Heat capacity $(J/kg\ K)$	840

Figure 4.1 A representative image of Patil's experimental set-up and the properties of particles and fluidizing gas used.

They followed a specific test procedure to investigate transient solid phase cooling. In the first step, they heated solid particles up to 120 °C. Then, they filled the hot particles into the test set-up at room temperature and fed nitrogen gas at room temperature through the inlet. After that, they recorded particle motion and temperature in the bed with standard and thermal cameras. The recorded images were processed to obtain solid phase temperature and volume fraction distribution in the bed. The cooling curves were presented for the average solid phase temperature below 90 °C. Therefore, the starting temperature for the cooling curve data was 90 °C. They repeated the same testing procedure for all experiments using different inlet velocities and bed mass. One of the important aspects of Patil *et al.*'s data set is the presentation of the measurement of temporal variation of the particle temperatures using thermal camera images. This allows a direct comparison with the TFM solid phase temperature predictions.

Furthermore, Patil *et al.* [39] modeled their experiments with the CFD-DEM approach and compared their simulation results with the experiments. The wall boundary conditions are the only ambiguous part in Patil *et al.* data set. As indicated above, the front part of the experimental set-up is glass, the sides are aluminium, and no information is given about the thicknesses. In their CFD-DEM study, Patil *et al.* [39] specified a heat transfer coefficient for the bed-to-wall (inside) as a fitting parameter and concluded that a value of 300 W/m^{2}K that gives closest to the experimental results. The wall side heat transfer is discussed in detail in the subsequent sections.

4.2. Initial and Boundary Conditions

All simulations used TFM approach implemented with Ansys Fluent 2024 (Student Edition). The solids phase hydrodynamic parameters were determined using KTGF presented in the theory section. The model is defined as 3D and transient. Figure 4.2 gives a representative image of the simulation model, initial conditions, and model dimensions.

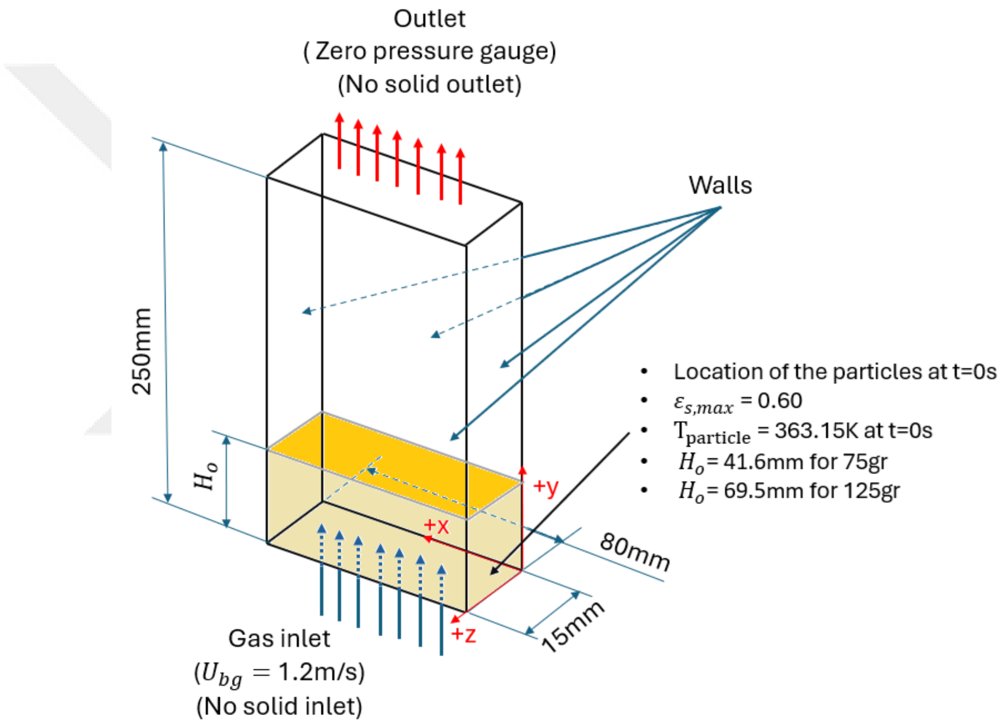

Figure 4.2 A representative image the simulation model, initial conditions and the model dimensions of Patil et al's experimental work.

The simulations were carried out in real time for 12 s. The first 2 s of the simulations were for the bed to get into fluidization state. The hydrodynamic results presented are the time-averaged values of the last 10 s of the simulations, with the data taken at 0.1 s intervals. The inlet gas, the solid phase, and the wall temperatures were set to 90 °C for the first 2 s of the simulation. At t = 2 s of the simulation, the temperature of the inlet gas was adjusted to 20 °C. The thermal results are also presented after 2 s of simulation.

The tangential component of the gas velocity is defined as the no-slip condition on the walls. Conversely, a wall specularity coefficient of 0.05 is defined for the tangential motion of the solid phases based on the results of the simulations in Chapter 2. Figure 4.3 demonstrates the hydrodynamic boundary conditions.

Furthermore, three wall boundary conditions were defined and investigated for their effects on the cooling behaviour. Fixed wall temperature is the first wall boundary condition, defined as a constant temperature with 20 °C. The second wall boundary condition is adiabatic. Heat loss is not permitted through the walls in adiabatic. The final wall boundary condition is a fixed heat transfer coefficient. Meanwhile, the outside walls with a wall thickness are defined in this boundary condition. The external free stream temperature is also fixed at 20 °C. Furthermore, the heat transfer coefficient for the outer wall is set to 8 W/m² K.

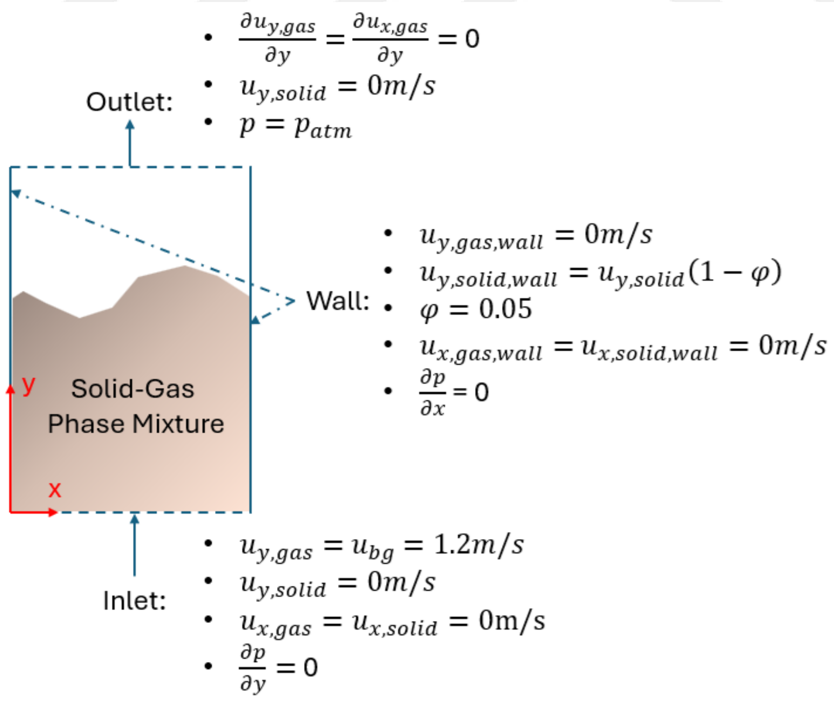

Figure 4.3 Hydrodynamic boundary conditions for the simulation model of Patil *et al.*'s experimental study.

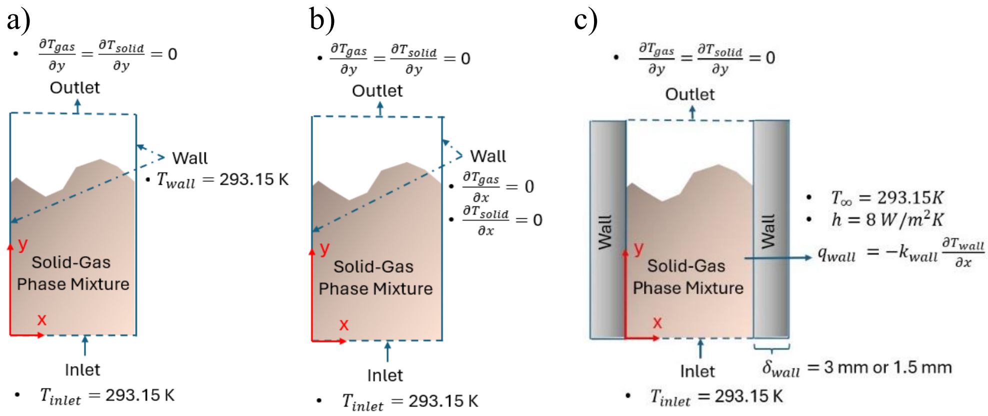

Figure 4.4 Thermodynamic boundary conditions, a) Fixed wall temperature, b) Adiabatic, and c) Fixed heat transfer coefficient.

A pressure-based solver is used in the mesh independence study. Furthermore, a pressure-velocity coupling scheme is assigned as the phase-coupled SIMPLE algorithm. The momentum, volume fraction, and energy discretizations are selected as first-order upwind algorithm, whereas PRESTO! algorithm is defined for pressure discretization. In hydrodynamic and thermal studies, the energy and momentum discretizations are changed to second-order upwind algorithms. The discretization belonging to the volume fraction is also changed to the QUICK algorithm.

The simulations were implemented using a constant time step of 0.0004 seconds. Each time step was solved in a maximum of 100 iterations. Under-relaxation factors for pressure, density, and volume fraction are defined as 0.5, whereas for momentum and energy they are defined as 0.2 and 1, respectively. The convergence criterion is selected as the absolute error between two iterations. Scaled residual values of 10^{-3} are defined for the momentum and the continuity equations, whereas residual values of the energy equations are selected as $1x10^{-6}$ for the convergence criterion. The flow is presumed to be laminar. Moreover, Table 4.1 represents other relevant parameters of the two fluid models.

Table 4.1 Parameters of two fluid model for mesh independence study for the simulation model of Patil et al.'s experimental data.

Gas-Solid Force Setup	Drag Coefficient:	Gidaspow
	Lift Coefficient:	-
	Virtual mass Coefficient:	-
Solid-Solid Force Setup	Restitution Coefficient:	0.9
	Granular Bulk Viscosity:	Lun et al.
	Granular Viscosity:	Gidaspow
	Radial Distribution:	Lun et al.
	Frictional Viscosity:	-
	Solid Pressure:	Lun et al.
	Granular Temperature:	Algebraic
Packing Limit	0.60	

4.3. Mesh Independence Study

For mesh independence studies, the solid phase's total weight is set as 75 gr. The 1.2 m/s inlet velocity is set. A fixed wall temperature of 20 °C is selected for the wall boundary condition. The true thermal conductivities of glass beads and nitrogen gases are assumed as effective thermal conductivity in the simulation model.

Six different grid sizes were selected. Each grid size has a different discretized length in the x, y, and z directions. The discretized length decreases from coarse to fine sizes. Furthermore, the element shape of all sizes is quadrilateral. Moreover, two inflation layers are defined at the wall boundaries because heat transfer of wall-to-bed is significant. Additionally, the total layer thickness is kept the same in all grid sizes and set to 1.5 mm. Conversely, the mesh size at the higher bed height is less significant because the gas-solid flow is not observed at upper bed heights. Hence, a bias factor, the ratio between the smallest and largest cell sizes, is defined in the y direction. Consequently, the grid size gets coarser at higher bed heights. The mesh dimensions are given in Figure 4.5.

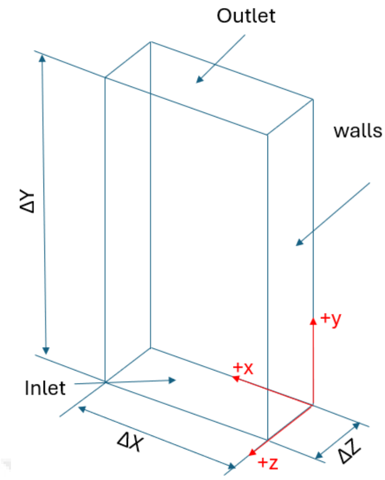

	ΔX (mm)	ΔY (mm)	ΔZ (mm)
Coarse Mesh	2.5	2.5	Bias ratio 6(5mm)
Coarse Medium Mesh	2	2	Bias ratio 6(4mm)
Medium Mesh	1.6	1.6	Bias ratio 6(3.0mm)
Medium Fine Mesh	1.5	1.5	Bias ratio 6(3.5mm)
Fine Mesh	1.4	1.4	Bias ratio 6(3.5mm)
Very Fine Mesh	1.4	1.4	Bias ratio 6(3.25mm)

	Total Element Number/Nodes	Element shape
Coarse Mesh	15800-18054	Quadrilaterals
Coarse Medium Mesh	29232-32768	
Medium Mesh	52416-57970	
Medium Fine Mesh	51480-56648	
Fine Mesh	56088-61612	
Very Fine Mesh	59983-65832	

Figure 4.5 Mesh settings for validation studies of Patil's Experimental.

The solid phase mass flux in the y direction was evaluated at 23 mm height from the inlet which is the same location as the experimental study. All results presented are for the midplane (z = 7.5 mm). The solid phase mass flux defines the mass of the particle flowing in the vertical direction per unit area and time. Furthermore, it is a collective measure of the local particle velocity and volume fraction. The local solid phase mass flux calculated as the product of particle volume fraction, axial velocity component, and particle density (The mass flux of the local solid phase can be calculated as the multiplication of the volume fraction of the particles, axial component of particles velocity, and particle density). The variation of the local solids mass flux for different mesh sizes are given in Figure 4.6. Furthermore, at the end of 12 seconds, the bed pressure drops, and the average temperature of the particles were calculated for all six grid sizes. The results are given in Table 4.2.

The trends of the mass flux curve of all grid sizes are similar. The difference between the different grid sizes is not significantly pronounced and there is no gradual trend as the mesh size is switched from course mesh (~18000 nodes) to very fine mesh (~66000 nodes). Meshes courser than 18000 nodes were not tried since it would be too course for a TFM study in comparison with the studies in the literature whereas a mesh finer than 66000 nodes would be computationally expensive. Similar results were observed for the average solids phase temperature and bed pressure after 12 s of simulations indicating no significant difference among mesh sizes. Additionally, all simulations were performed on an HP Victus 16-r1034nt Notebook with Intel Core i7-14700HX processors containing 28 cores. However, the Ansys Fluent (Student Edition) allows the use of maximum four parallel processors. Therefore, the simulations were run on only four cores. Table 4.2 gives the computational times of mesh independence studies for 12s.

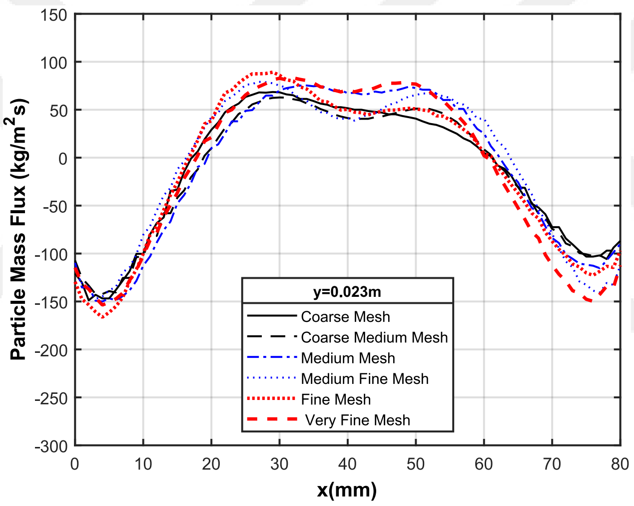

Figure 4.6 Variation of the particle mass flux in x direction for different mesh sizes.

Table 4.2 Results of the pressure drops, the average temperature of solid phase and the computational time at the end of 12 seconds for the mesh independence study.

	The average temperature (K) of solid phase at t = 12 s	**Pressure Drop (Pa)**	**The Computational Times (h)**
Coarse Mesh	305.1	592.4	~5
Coarse Medium Mesh	303.5	594.5	~7
Medium Mesh	301.9	595.3	~8.5
Medium Fine Mesh	303.1	593.9	~8.5
Fine Mesh	303.1	596.9	~10
Very Fine Mesh	302.6	595.2	~10.5

One of the important aspects of thermal study is the energy balance. During the convective cooling of the bed, the solid phase's energy loss should correspond to the heat loss through the walls and energy leaving the system via air with respect to the inlet. Therefore, energy balance was also examined in the context of the mesh studies. Figure 4.7 demonstrates the heat loss by the time-dependent in the system for fine mesh study. It can be observed clearly that the summation of the wall and outlet energy losses are almost equal to the solid phase energy change. Moreover, for all grid sizes, energy losses of walls and outlets were calculated, and their relative errors were evaluated according to total solid phase energy change. Their results are given in Table 4.3, and the error of the energy losses of all grid sizes can be observed under 5%. These are truncation errors due to discretization and their values are acceptable for energy balance.

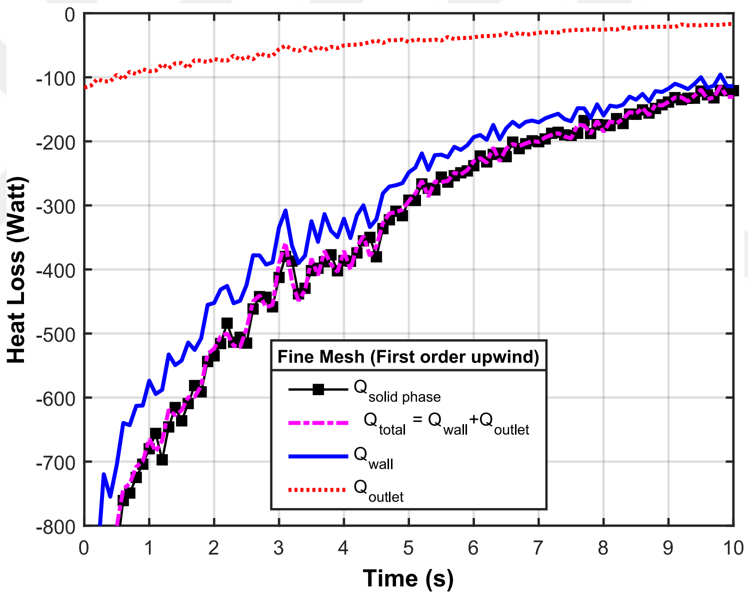

Figure 4.7 Time-dependent heat losses of the system for fine mesh.

In conclusion, mesh-independent studies were carried out for six different grid sizes. All grid sizes were compared for solid phase mass flux, pressure drop, and energy balance and no significant differences were observed. Hence, fine mesh settings were selected for the hydrodynamic and thermal studies.

Table 4.3 Energy losses for different mesh sizes at the end of 12 s of simulation.

	Solid Phase Enthalpy Change (J)	**Walls and Outlet Total Energy loss (j)**	**Error (%)**
Coarse Mesh	-3530.1	-3657	3.48
Coarse Medium Mesh	-3662	-3755.6	2.49
Medium Mesh	-3780.6	-3858.3	2.01
Medium Fine Mesh	-3670	-3780.3	2.15
Fine Mesh	-3630	-3780.6	3.99
Very Fine Mesh	-3722.9	-3812.3	2.34

4.4. Hydrodynamic Study

For hydrodynamic studies, momentum and energy discretizations were applied as second-order upwind algorithm. Moreover, QUICK algorithm is selected for volume fraction discretization. Additionally, fine mesh settings were used at three various inlet velocities: 1.2 m/s, 1.54 m/s, and 1.71 m/s.

Figure 4.8 presents the variation of particle mass flux with x direction at a height of 23 mm for different inlet velocities. The first-order and second-order algorithms were compared with the experimental findings for all three inlet velocities. The second-order upwind scheme matches the experimental data less than the first-order upwind scheme for 1.2 m/s inlet velocity, especially at the center region. However, this may not be a result that can be generalized because, generally, more accurate results can be expected to be observed when using the second-order upwind algorithm. So, the result is unexpected. The reason may be inconsistencies in the experimental results due to margins of error during experimental measurements. On the contrary, second-order upwind algorithms for 1.54 m/s and 1.71 m/s inlet velocities give more accurate results than first-order algorithms. Furthermore, there is a discrepancy between the experimental and simulation results for both discretization schemes near the wall region. Overall, the characteristic shape of the particle mass flux curve is well captured. Figure 4.8a, Figure 4.8b, and Figure 4.8c represent the hydrodynamic results for 1.2 m/s, 1.54 m/s, and 1.71 m/s inlet velocities, respectively. The simulation results are generally consistent with the experiments that exclude the wall region. Although, in the simulations, the ‘hook-like’ behavior near the wall is well replicated, the particle mass flux values at the wall are always underpredicted compared to experimental results in all cases. Meanwhile, the calculation time of the first-order upwind scheme for three inlet velocities for 12 seconds took approximately 10 hours. In contrast, the solving time of the second-order upwind algorithm took approximately 16 hours.

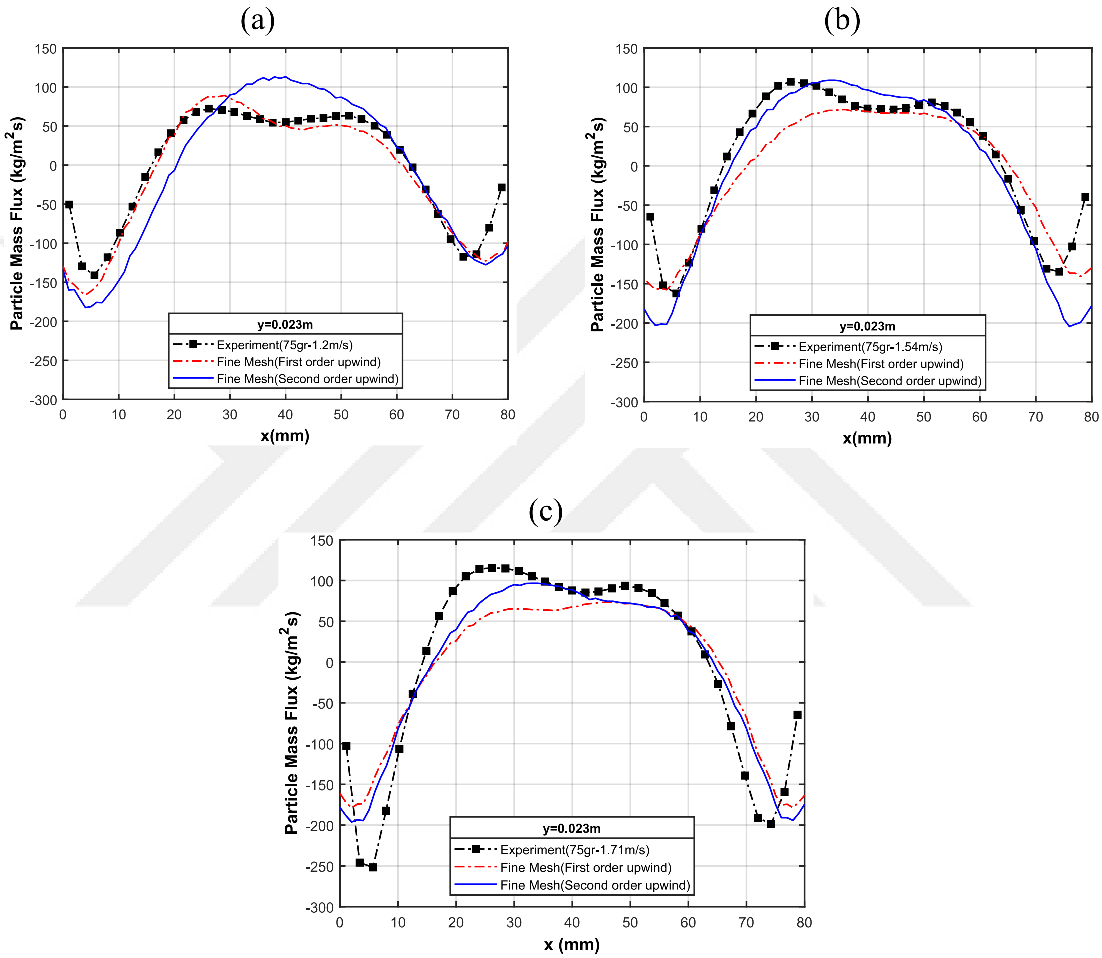

Figure 4.8 Examination of particle mass flux with x direction at a height of 23 mm for different inlet velocities: a) 1.2 m/s, b) 1.54 m/s, and c) 1.71 m/s.

In conclusion, the hydrodynamics studies for three various inlet velocities were compared with the experimental findings. The general shape and trend of the experimental mass flux profile are well captured by the simulations. The highest discrepancy is observed near the wall region regardless of the type of the discretization scheme. Hence, second-order upwind discretization and fine mesh settings are deemed to be sufficient for accurately predicting the gas-solid flow dynamics of this complex system and are also used in thermal studies.

4.5. Thermal Studies

In the context of the thermal studies, the following investigations were carried out:

- Evaluating the Gunn's [62] solid-gas phase interphase heat transfer correlation,
- Evaluating the effects of different methods of modeling thermal conductivities of both phases,
- Evaluating the effects of wall boundary conditions on cooling behaviour.

As presented in Chapter 2, one of the widely used correlations that define the heat transfer between gas-solid interaction is Gunn's [62] correlation. The interphase heat transfer coefficient in Gunn correlation is attached to solids Reynolds number, solids volume fraction, gas Prandtl number, and true gas thermal conductivity. Although Ansys Fluent has a built-in model for Gunn's correlation, it was found that it calculates the heat transfer coefficient using the effective gas phase thermal conductivity value – instead of the true value—when Hunt's kinetic theory or Zehner-Schlunder approach is utilized. In order to circumvent this problem, Gunn's model was applied in Ansys Fluent using a user-defined function (UDF).

A modeling study was performed to evaluate the heat transfer coefficients calculated by Gunn's correlation. The study was conducted for 1.2 m/s inlet velocity, and true thermal conductivities were used as effective thermal conductivities for both phases. Furthermore, the bed-to-wall heat transfer was neglected in the simulation model. Hence, the adiabatic wall boundary condition was defined. Figure 4.9 presents the examination of the heat transfer coefficient between gas-solid interaction in the x direction at y = 30 mm based on Gunn's correlation. The results presented are the time-averaged values. Interestingly, the interphase heat transfer coefficient shows a similar profile to the particle mass flux profile increasing from the wall to the center of the inlet, exceeding 450 W/m^2K as the maximum value. One of the main parameters in Gunn's correlation, particle Reynolds number, is directly proportional to particle mass flux. Furthermore, the particle Nusselt number, Nu_p, calculated by the correlation agrees with the experimental values measured for fluidized beds.

In thermal studies, the effects of gas-solid interphase heat transfer ratio were first investigated for adiabatic wall boundary conditions. Then, different thermal conductivity assumptions were calculated for wall boundaries, such as adiabatic and fixed wall temperature. Furthermore, various wall boundary conditions were also evaluated to determine their effect on the solid phase cooling behavior.

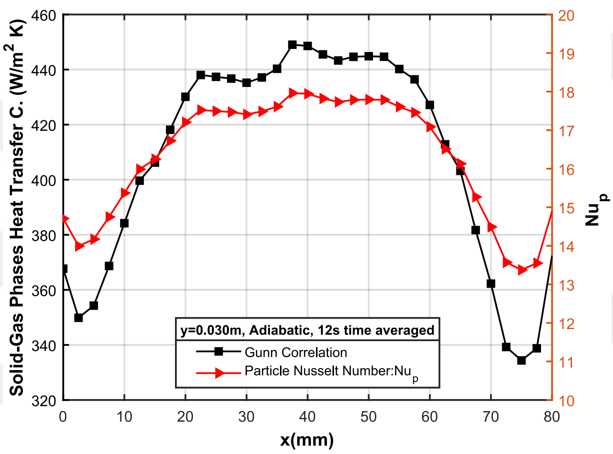

Figure 4.9 Examination of the time-averaged gas-solid interphase heat transfer in the x direction at y= 30 mm based on Gunn’s correlation.

Moreover, in the x direction, Figure 4.10a and Figure 4.10b demonstrate the temperature distribution of the solid and gas at t = 1 s and t = 5 s, respectively. The results were evaluated at 20 mm, 30 mm, and 40 mm heights from the inlet. Temperature differences decrease between both phases as the height from the inlet increases. Due to the high magnitude belonging to the gas-solid interphase heat transfer coefficient, that is peculiar to fluidized beds, energy of the solid phase gets transferred fast to the gas phase. So, the gas-solid temperature variations cease quickly.

The thermal conductivity values of both phases are another major factor for thermal calculations in the context of TFM. The particle thermal conductivity value is more critical than the gas thermal conductivity value. For TFM simulations, as presented in Chapter 2, both phases are described as having an effective thermal conductivity which is different from the so-called true thermal conductivity and depends mainly on the volume ratios of each phase. With the aim of investigating and evaluating the effects of thermal conductivity values for Patil *et al.*’s experimental data set, simulations were run with three different thermal conductivity approaches are used:

- Values of true thermal conductivity of both phases,
- Values of effective thermal conductivity of both phases using Zehner-Schlunder's standard approach,
- Effective thermal conductivity value of particles using Hunt’s kinetic theory approach [57] with true gas thermal conductivity.

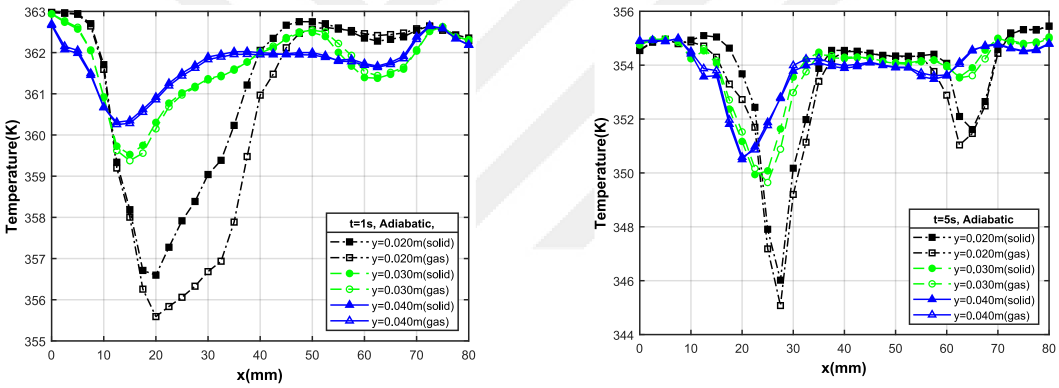

(a) (b)

Figure 4.10 The examination of the instantaneous gas and solids phase temperature distribution in the x direction for 1.2 m/s at a) 1s and b) 5s.

Therefore, in the first approach, the true thermal conductivities of both phases are defined as effective thermal conductivity. In the second approach, the effective thermal conductivities are calculated according to Zehner-Schlunder's standard approach. In the third approach, Hunt's kinetic theory approach is used for effective solid thermal conductivities. Zehner-Schlunder's standard and Hunt's kinetic approaches are not embedded in Fluent. Hence, a UDF was written to implement these approaches. The time averaged thermal conductivity was calculated for 12 s at 30 mm height from the inlet. All simulation studies were also conducted for 1.2 m/s inlet velocity.

Figure 4.11 presents the distribution of the time-averaged effective solids phase thermal conductivity values for Zehner-Schlunder's standard approach and Hunt's kinetic theory approach as well as the true solid thermal conductivity and solids volume fraction. The solids phase effective thermal conductivity as calculated by Zehner-Schlunder's standard approach depends on the solid volume ratio in the x direction. These findings can be observed clearly in Figure 4.11a. Moreover, Figure 4.11b shows the true and effective thermal conductivities of Hunt's kinetic theory approach. The results of Hunt's kinetic theory approach depend on the granular temperatures presented in the theory section. As the time averaged value of the granular temperature – that indicates the energy resulting from particle-particle collisions in m^2/s^2 –, increases towards the center, and so does the effective solids thermal conductivity. This trend is the opposite of the trend observed for Zehner-Schlunder's standard approach. Another important difference between Zehner-Schlunder's standard approach and Hunt's kinetic theory approach is the significant difference in the magnitude of effective thermal conductivity of solid phase. The value of Hunt's approach is approximately ten times the true value. Finally, the smallest values of effective solid thermal conductivity are obtained with Zehner-Schlunder's approach, which is one-fifth times the true value.

Furthermore, Figure 4.12 demonstrates the normalized effective solid and gas phase thermal conductivities which are evaluated with different solid volume fractions using Zehner-Schlunder's approach. Figure 4.13 gives the normalized effective solid phase thermal conductivities which are evaluated with different solid volume fractions and granular temperature using Hunt's approach. The ratio of effective-to-true solids thermal conductivity value shows an increasing trend with the solids volume fraction for the Zehner-Schlunder's approach. For Hunt's approach, the trend depends on the granular temperature; it has a maximum at a solids volume fraction of 0.35-0.4.

In this part, the effects of various thermal conductivity approaches on the cooling curves of the bed are investigated for different wall boundary conditions. The transient changes in the averaged solid phase temperature distribution for adiabatic wall boundary conditions are demonstrated in Figure 4.14. Regardless of the thermal conductivity approach used (True, Zehner-Schlunder, or Hunt), all curves are identical, as seen from this figure. All studies overestimate the experimental results. Moreover, the temperature variation between the experiments and the simulations is around 10 ^{o}C at the end of 10 s of cooling.

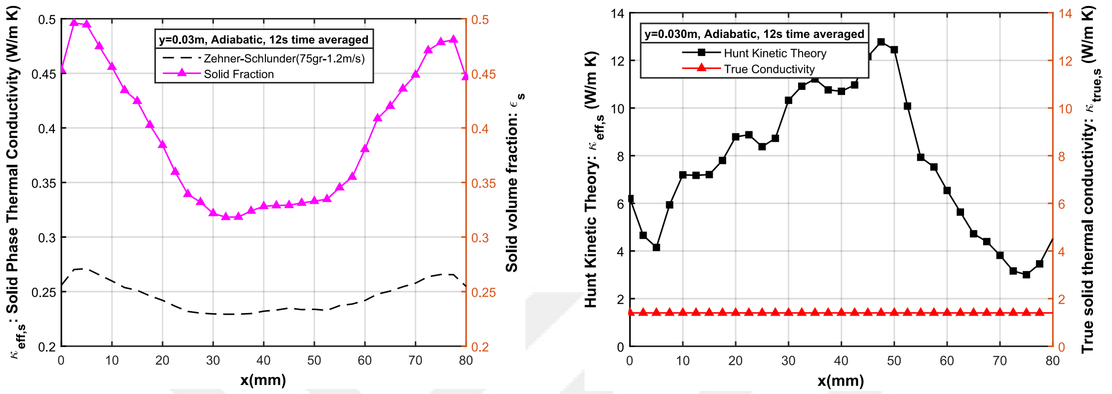

(a) (b)

Figure 4.11 The time-averaged solid phase effective thermal conductivity distribution at y=30 mm in the x direction for a) Zehner-Schlunder's standard approach, and b) Hunt's kinetic theory approach.

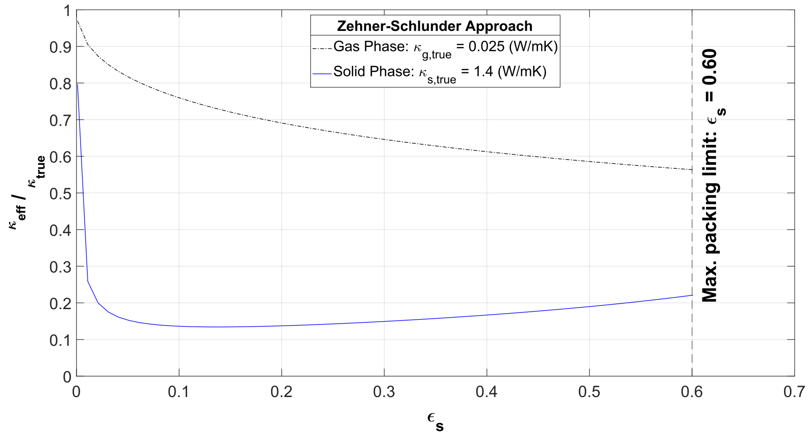

Figure 4.12 The variation of the normalized effective solid and gas phase thermal conductivity with solid volume fraction for the materials used in Patil *et al.*'s experimental study according to Zehner-Schlunder's approach.

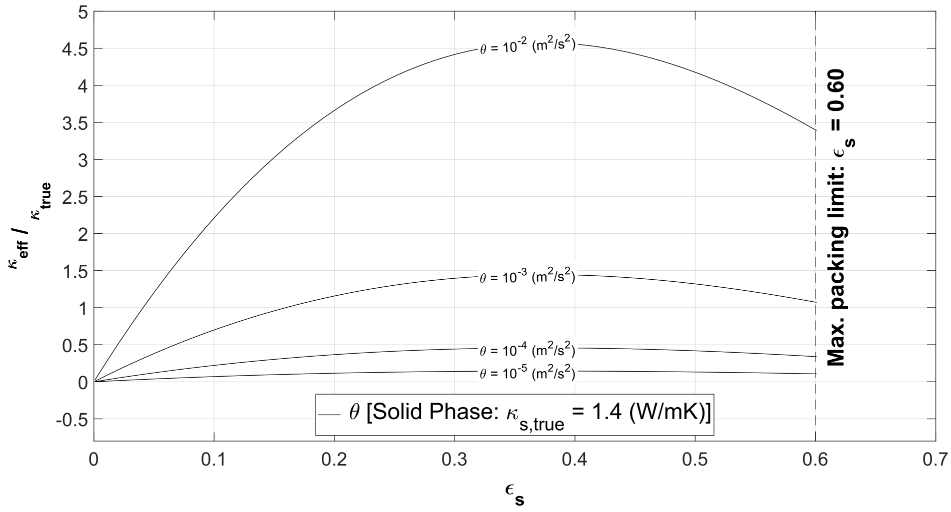

Figure 4.13 The comparison of the normalized effective solid phase thermal conductivity with solid volume fraction for the materials used in Patil *et al.*'s experimental study according to Hunt's kinetic approach.

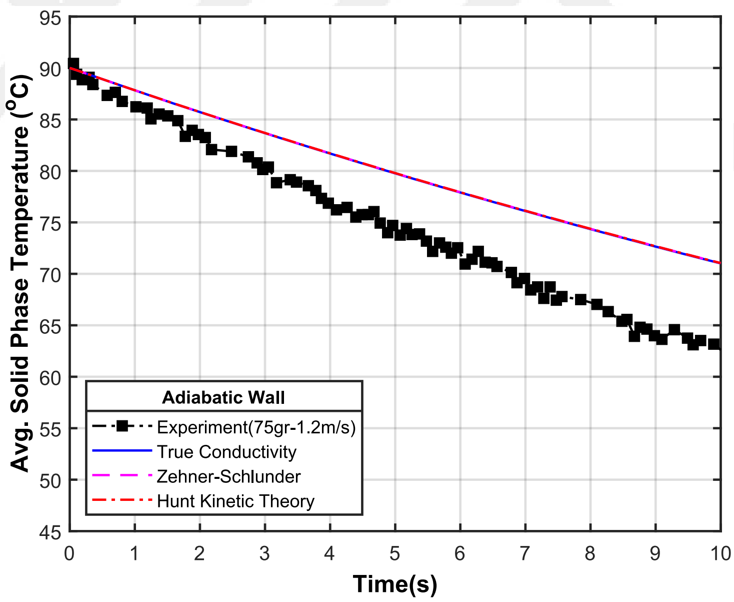

Figure 4.14 The examination of average solids temperature in the bed with respect to time for different effective thermal conductivity approaches for adiabatic wall case.

Simultaneously, other simulation studies were performed to examine the impact of effective solid thermal conductivity on the heat transfer between the wall and the bed. Therefore, the fixed wall temperature boundary condition was defined, and other operating conditions were kept the same in the simulation study. Figure 4.15 represents transient changes in the averaged solid phase temperature distribution for the fixed wall temperature boundary conditions. All thermal conductivity approaches underestimate the experimental results. However, contrary to the previous case, there is a remarkable gap between the curves; the higher the effective solids thermal value, the faster the cooling is. Apparently, a ‘cold’ wall boundary condition results in higher temperature gradients in the solids phase for which the value of the solids thermal conductivity becomes very critical. Zehner-Schlunder's approach is the closest to the experimental results. However, the experimental results are underestimated. Furthermore, at the end of the cooling period, the temperature variation between the simulation and the experiment is approximately 10 °C. On the contrary, in conclusion, Zehner-Schlunder's standard approach gives more predictable results for solid phase cooling behavior. So, Zehner-Schlunder's approach was used in simulation studies conducted with the fixed coefficient of heat transfer for the outer wall.

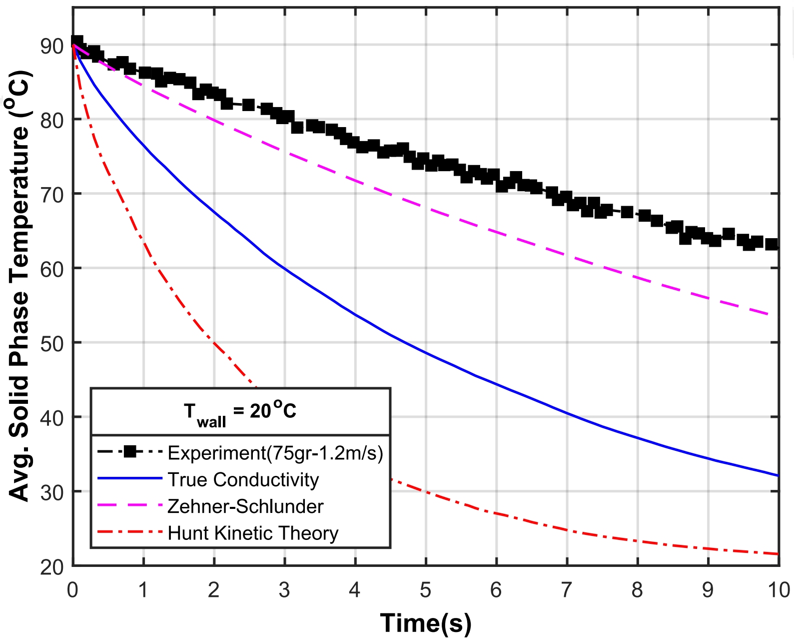

Figure 4.15 The examination of the time-dependent average solid phase temperature in the bed for different effective thermal conductivity approaches and the fixed wall temperature case.

The results can be represented more accurately when the wall is modeled as realistically as possible in the simulation because realistic wall modeling affects the ratio of the solid phase energy loss via the walls, which can be significantly important. So, the effect of the wall's heat capacity must be defined with wall thickness. For this reason, two simulation cases were carried out, defining the fixed heat transfer coefficient wall boundary with two different wall thicknesses: 3 mm and 1.5 mm, respectively. As mentioned before, Patil *et al.* did not mention the thickness of aluminium and glass walls. Therefore, 3 mm and 1.5 mm wall thicknesses were selected arbitrarily. The heat capacity of the aluminum and sapphire glass was taken as 900 J/kgK, and 761 J/kgK, respectively. A convective heat transfer coefficient of h = 8 W/m^{2}K was assumed for the outer wall, a typical free convection value. Figure 4.16 demonstrates the time-dependent averaged solid phase temperature distributions for different boundary conditions for 1.2 m/s inlet velocity. The adiabatic and fixed wall temperature cases are also presented for comparison. The fixed heat transfer coefficient case with a wall thickness of the1.5 mm predicts the experimental data very accurately. Furthermore, Figure 4.17 and Figure 4.18 represent the contour images of the solid phase temperature distribution of the simulation and the experiment for instantaneous time at 1 s and 4 s. The simulated temperature distribution is very similar to the experimental one especially at t = 4 s, showing the peculiar cold spots.

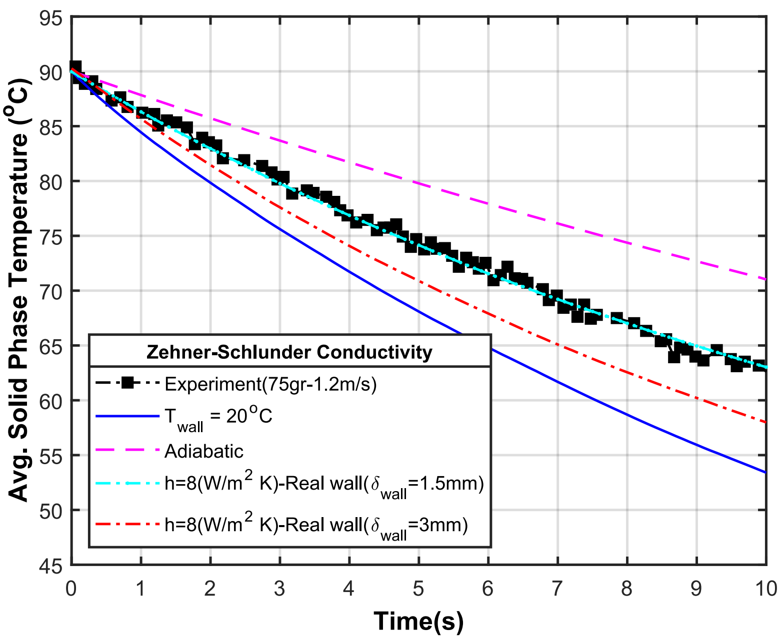

Figure 4.16 The examination of the time-dependent average solids temperature in the bed for different wall boundary conditions for 1.2 m/s inlet velocity.

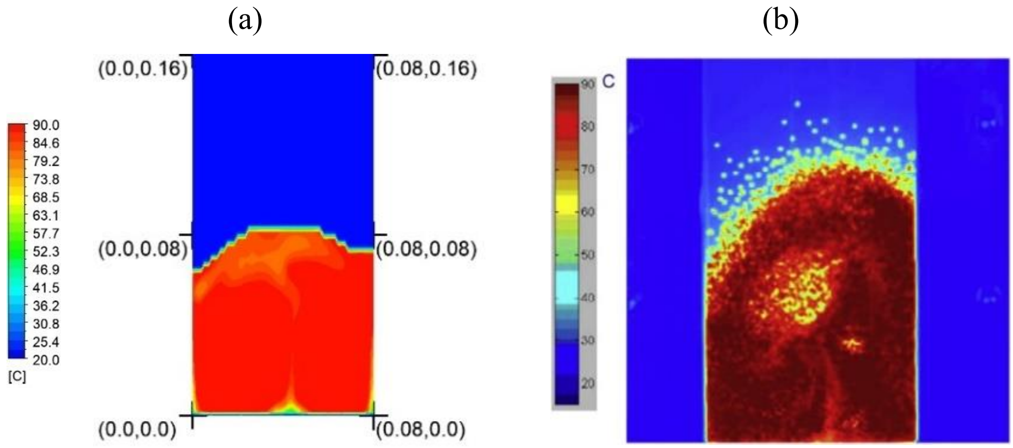

Figure 4.17 Contour images of the particle temperature distribution at t = 1 s at the midplane (z = 7.5 mm), a) the simulation, and b) the experiment for 1.2 m/s inlet velocity, h = 8 W/m^2K, wall thickness = 1.5 mm.

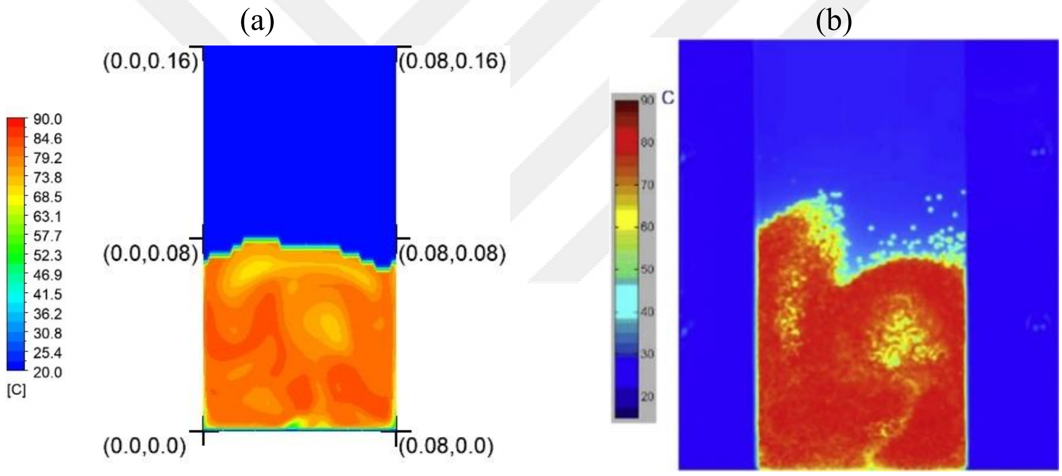

Figure 4.18 Contour images of the particle temperature distribution at t = 4 s at the midplane (z = 7.5 mm), a) the simulation, and b) the experiment for 1.2 m/s inlet velocity, h = 8 W/m^2K, wall thickness = 1.5 mm.

The simulations, which used the same 1.5 mm wall thickness and Zehner-Schlunder's approach, were carried out for 1.54 m/s and 1.71 m/s inlet velocities, individually. The case of a constant wall temperature condition is also presented for these velocities for comparison. Figure 4.19a and Figure 4.19b demonstrate the results. The simulations of both different inlet velocities result in excellent agreement with the experimental results. Consequently, defining an optimal wall boundary condition is crucial for the successful prediction of the solid-phase cooling behavior.

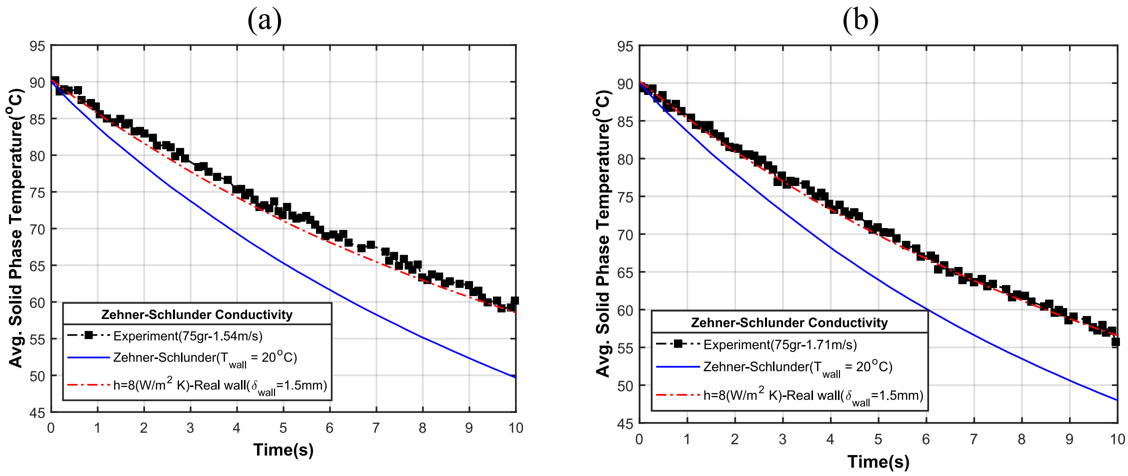

Figure 4.19 The examination of the time-dependent average solids temperature in the bed for different wall boundary conditions with a) the inlet velocity of 1.54 m/s and b) the inlet velocity of 1.71 m/s.

4.6. Conclusions for Patil *et al.*'s Experimental Data Set

Validation studies in the TFM approach are required to understand how gas-solid interaction works and how material properties and boundary conditions affect thermal behavior in the solid phase. Therefore, Patil *et al*'s experimental data sets are selected to validate the TFM approach from thermal perspective.

As a first step, the mesh independence and energy balance studies were completed. Various mesh sizes were investigated in terms of hydrodynamic behavior. The trends of the mass flux curve of all grid sizes are found to be similar, although inconsistent behavior was observed when decreasing the grid size. In contrast, differences in the bed pressure drops and average solid phase temperatures with respect to mesh size are minimal. Moreover, the energy balance was also examined in the mesh studies. The error in the energy balance for all grid sizes was under 5%.

The hydrodynamics studies were compared with the experimental findings for three various inlet velocities. Although minor differences existed between the simulation and experimental findings, especially close to the wall region, the simulated mass flux curves were consistent in trend and magnitude with the experimental results. Hence, thermal studies were continued with second-order upwind discretization and proper mesh settings.

Firstly, the interphase heat transfer correlation proposed by Gunn was used to obtain the heat transfer coefficient between gas-solid interphase. Furthermore, the coefficient rises from the wall to the center of the inlet and exceeds 400 W/m^2K for Patil *et al*'s experimental conditions. As the height from the inlet increases, temperature differences among both phases decrease. The high value of the gas-solid interphase heat transfer coefficient causes energy to transfer quickly between both phases. Hence, gas-solid temperature variations come close to each other quickly.

Three different thermal conductivity approaches were used to investigate their effects on the simulation results: true thermal conductivity values were used as effective values, solids phase effective thermal conductivity values were calculated Zehner-Schlunder's and Hunt's kinetic theory approaches, all implemented using specific UDFs. The values of Hunt's approach are approximately ten times the true value. Finally, the lowest values of effective solid thermal conductivity were obtained with Zehner-Schlunder's approach, which is one-fifth times the true value.

Different wall boundary conditions were used since the most ambiguous part in Patil *et al.*'s data is the wall boundary conditions. Generally, Zehner-Schlunder's approach resulted in better predictions regardless of the wall boundary condition for all cases compared to kinetic approach. When a 1.5 mm aluminum wall thickness with an 8 W/m2K outer free convection heat transfer coefficient was determined for the wall boundary condition, an excellent agreement was achieved with the experimental findings for three various superficial gas velocities.

Overall, calculating the heat transfer coefficient between gas-solid interphase, the effective thermal conductivity of solid phase and appropriate definition of the wall conditions are required for accurate modeling of the cooling or thermal energy discharge behaviour of the bed. Therefore, the following suggestions are made based on the Patil *et al*'s. experimental data set:

- The hydrodynamic validations are very important before carrying out a thermal study.

- The overall energy balance must always be checked to ensure the reliability of the thermal simulations which are often overlooked in the literature. It is suggested that Zehner-Schlunder's standard approach be used instead of kinetic approaches.
- Once the thickness and the material of the wall are known, a wall boundary condition with a fixed outer wall heat transfer coefficient (based on the ambient conditions) work fairly well.

5. HOT SPOUTED BED VALIDATION STUDY - II

5.1. Validation Studies of a Directly Irradiated Spouted Bed

As mentioned in the introduction, carbo and olivine particles were suggested for particle receivers in CSP applications. Moreover, they have high density (above 3000 kg/m^3) and large particle sizes (>~1mm) to be processed more suitably in a spouted bed. However, according to the literature survey, the suggested particles in a spouted bed receiver were never examined in detail. Therefore, Ozdemir [75, 76, 77] built an experimental setup which is a conical spouted bed receiver located in the multiphase laboratory of Hacettepe University. He carried out charging (using a metal halide lamp) and discharging (using spouting air with the lamb turned off) different experiments in the setup with the carbo and olivine particles. This part of the thesis investigates the discharging process numerically once the lamb is turned off. The convective cooling of the directly irradiated bed material (CarboHSP) in a spouted bed was analyzed using TFM approach. The thermal studies were compared with the experimental findings.

The bed wall is made of 5 mm-thick stainless steel. The outer surface of the bed is protected by 50 mm-thick glass wool isolation to limit heat loss through the wall. Additionally, Figure 5.1 and Figure 5.3a show the bed dimensions and a schematic view of the receiver.

A 2 kW$_{el}$ metal halide lamp with a concave reflector is positioned just above the bed outlet. The lamp light focuses on the bed surface with the help of the reflector. Additionally, a fan is placed on the lamp to prevent getting too hot while operating.

During charging and discharging processes, Ozdemir [75] measured the bed temperature at three different bed locations with thermocouples. Two are located in the midpoint of the annulus at 30 mm and 70 mm heights from the inlet, respectively. Another thermocouple is located at the spout axis at 50 mm height from the inlet. Their locations in the bed are also shown in Figure 5.3b. Furthermore, there are two thermocouples at the external and internal surfaces of the bed. It should be noted that the thermocouple at the inner surface does not contact the wall directly. It is located in a measurement hole at the side wall and adjusted to be behind the inside wall surface level. The outside wall thermocouple contacts the outer surface of the insulation directly.

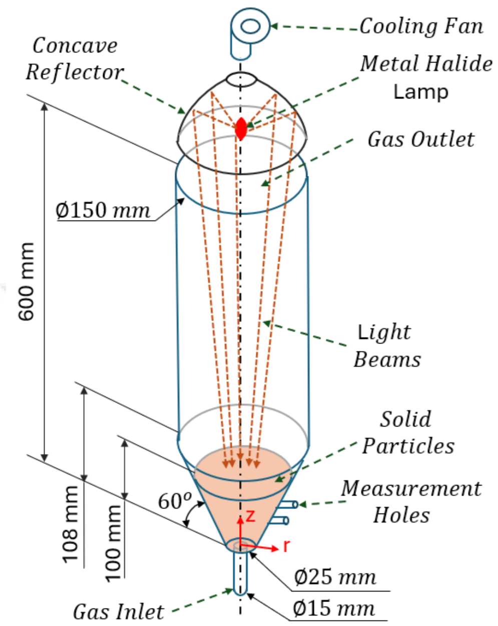

Gas Phase Properties	
Material	Air
Density (kg/m^3)	1.225
Heat capacity ($J/kg\ K$)	1006
Viscosity ($kg/(m\ s)$)	1.79x10^{-5}
Thermal conductivity (W/m K)	0.0242

Solid Phase Properties	
Material	CarboHSP
Particle Diameter (m)	0.00095
Density (kg/m^3)	3630
Material	Olivine
Particle Diameter (m)	0.0012
Density (kg/m^3)	3080

Figure 5.1 A schematic view of the directly irradiated spout bed receiver test setup at the Multiphase Flow Laboratory, Hacettepe University.

The particles were filled up to 100 mm height from the inlet. The density and mean diameter of the carbo particles are 3630 kg/m^3 and 0.95 mm, respectively. Carbo particles have a maximum packing limit of 0.58. As the first step, the spouted bed's hydrodynamic operation conditions were evaluated at ambient temperature. A velocity of 25 m/s was measured as the minimum spouting inlet velocity of the carbo HSP particles. The interstitial gas velocity and bed pressure measurements were carried out at 1.15 U_{ms} inlet velocity [75].

After obtaining hydrodynamic parameters, hot bed experiments heated by directly irradiating with the 2 kW_{el} metal halide lamp were carried out. Furthermore, the bed was operated under 1.0 U_{ms} inlet velocity. The results were examined in three sub-step heating regions: transient heating, steady-state heating, and transient cooling. Figure 5.2 indicates a schematic graph of the normalized bed temperature of three sub-step heating regions based on the experimental results.

In the transient heating region, also known as the charging operation of the bed, the carbo (or olivine) particles were placed in the bed at room temperature and room-temperature air was fed through the inlet. After obtaining stable spouting operation, the lamp began heating the bed surface directly. At the same time, the thermocouples began to record temperatures. Initially, the variation rate of the particle temperature was high and then rate of heating began to go down (steady-state heating region). After the bed reached steady-state condition, the lamb was turned off with and the experiment moved to the transient cooling region, also known as the discharging operation of the bed. In this thesis, the spouted bed receiver was simulated using TFM only for the discharging process (transient cooling region). Furthermore, the experimental cooling data sets, which were measured by all thermocouples, are given in Figure 5.3c.

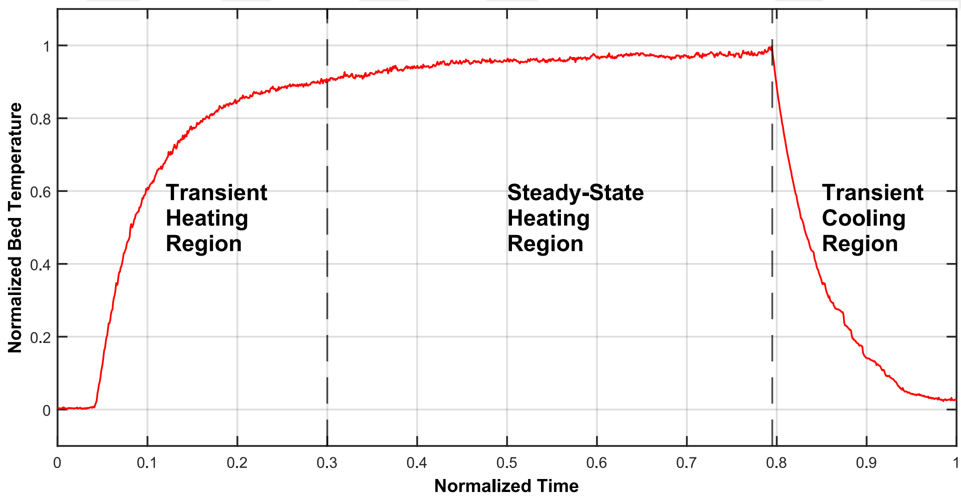

Figure 5.2 A schematic graph of the normalized bed temperature relative to the normalized time in three sub-step heating regions.

Carbo HSP is a commercial product with thermal conductivity, heat capacity, and absorptance values supplied by its manufacturer. Table 5.1 demonstrates the temperature-dependent material properties of the carbo HSP.

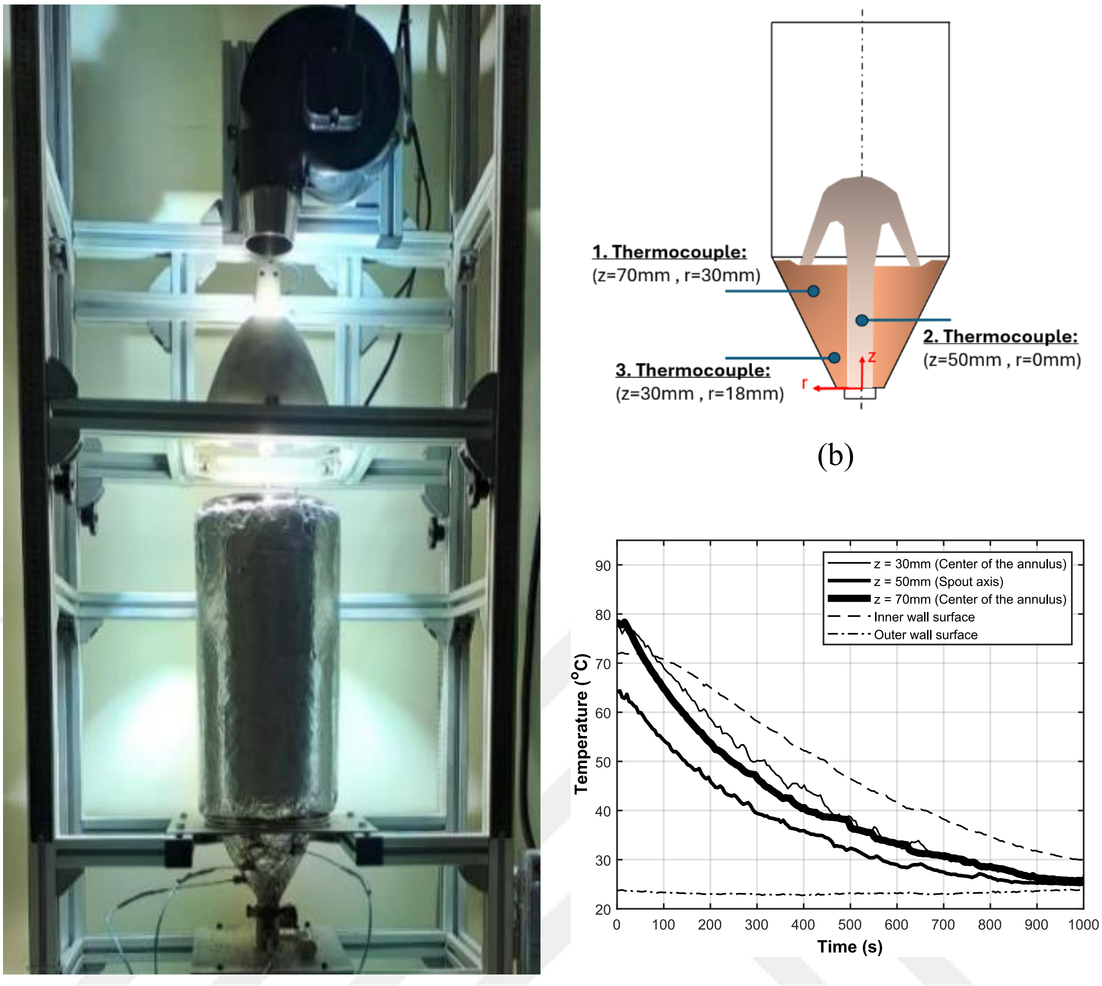

(a) (c)

Figure 5.3 a) Ozdemir's test set-up b) The locations of the thermocouple in the bed, and c) The experimental cooling data sets, which were measured by all thermocouples *[75, 76, 77]*.

Table 5.1 The temperature-dependent thermal conductivity and heat capacity values for carbo HSP [75].

Temperature (°C)	**Thermal Conductivity** (W/m K)	**Heat Capacity** $(J/kg\ K)$
20	0.32	628.02
400	0.5	753.62
800	0.77	837.36
1200	0.97	1172.3

5.2. Initial and Boundary Conditions

All simulations used TFM approach and was implemented with Ansys Fluent 2024 (Student Edition). The solids phase hydrodynamic parameters were determined using KTGF presented in the theory section. The simulation model is 2D axisymmetric and transient. Figure 5.4a gives a schematic view of the simulation model, initial conditions, and model dimensions.

The tangential velocity of both phases on the walls is defined as the no-slip condition. The hydrodynamic boundary condition is given in Figure 5.4b. Meanwhile, three different wall boundary conditions were defined in the computational model. Adiabatic is the first wall boundary condition that is indicated as no heat loss through the walls. The second wall boundary condition is defined as a time-dependent wall temperature that is experimentally measured using the thermocouple at the inner wall surface. Figure 5.5 demonstrates the thermodynamic boundary conditions.

The mesh independence studies were performed only for the adiabatic wall boundary conditions. Meanwhile, the time-dependent wall temperature boundary condition was used only for thermal studies.

A pressure-based solver is used, and a pressure-velocity coupling scheme is assigned as the phase-coupled SIMPLE algorithm. In the first 2 s of the simulation, the first-order upwind algorithm is defined for momentum and volume fraction because the spout occurs barely in the first 2 s. Hence, the first 2 s of the simulation are too unstable for second-order upwind algorithms. After 2s of the simulation, the momentum discretizations is changed to second-order upwind algorithm. The discretization belonging to the volume fraction is also changed to the QUICK algorithm. Meanwhile, at the beginning of the simulation, the energy discretization is defined as second-order upwind algorithms. Furthermore, the PRESTO! algorithm is defined for pressure discretization.

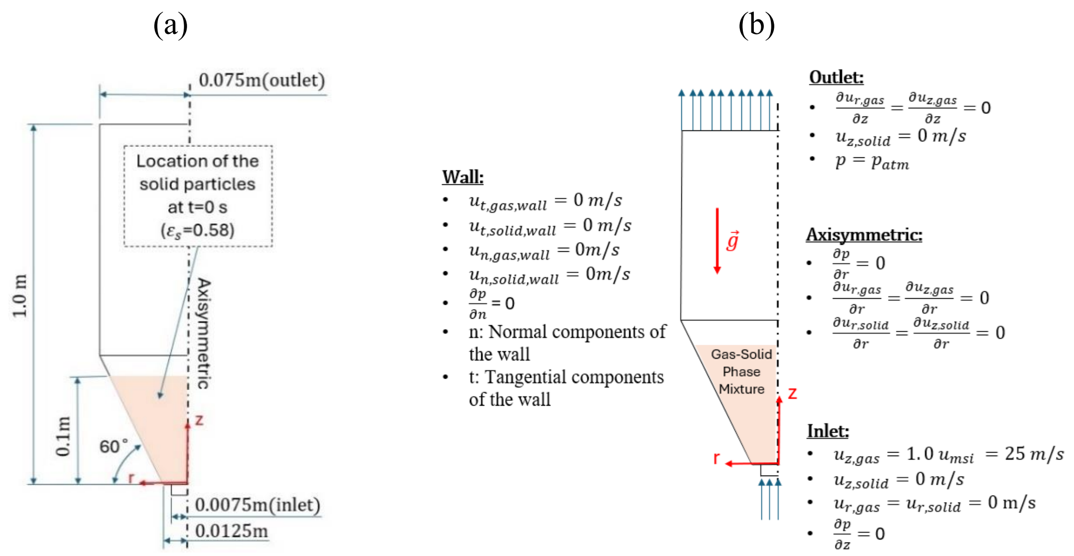

Figure 5.4 a) Initial conditions and the model dimensions, and b) Hydrodynamic boundary conditions of the hot bed simulation model.

The simulations were implemented using a constant time step of 0.0004 seconds. Each time step was solved in a maximum of 100 iterations. Under-relaxation factors for pressure, density, and volume fraction were defined as 0.5, whereas for momentum it is defined as 0.2. On the other hand, the under-relaxation factor for energy is set as 1. The convergence criterion is selected as the absolute error between two iterations. Scaled residual values of 10^{-3} are defined for the momentum and the continuity equations, whereas residual values of the energy equations are selected as $1\text{x}10^{-8}$ for the convergence criterion. The flow is assumed to be laminar.

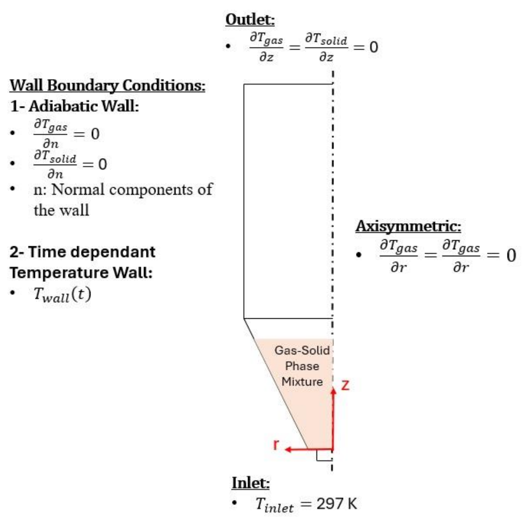

Figure 5.5 Thermodynamic boundary conditions of the hot bed simulation model.

5.3. Mesh Independence Study

Four grid sizes were selected: coarse, medium, fine, and very fine for the mesh independence study. Each grid size has a different discretized length in the r and z directions. The discretized length decreases from coarse to fine sizes. Furthermore, the grid structure remains the same as in the cold bed study. Nevertheless, the discretized lengths were selected arbitrarily and had almost half the lengths of the cold bed study. The element shape of all sizes is quadrilateral. The mesh dimensions are given in Figure 5.6.

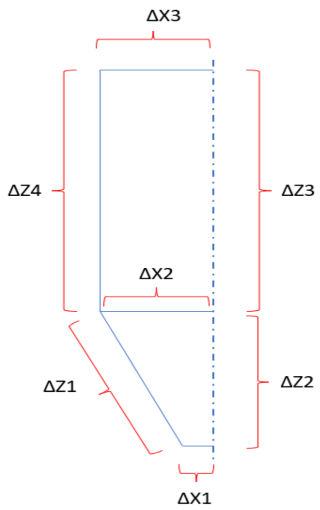

	ΔZ1 (mm)	ΔZ2 (mm)	ΔZ3, ΔZ4 (mm)	ΔX1 (mm)	ΔX2, ΔX3 (mm)
Coarse mesh	1.15	1	Bias ratio 15 (5mm)	0.1	1
Medium mesh	0.92	0.8	Bias ratio 15 (4mm)	0.08	0.8
Fine mesh	0.69	0.6	Bias ratio 20 (4.5mm)	0.06	0.6
Very fine mesh	0.575	0.5	Bias ratio 20 (3.5mm)	0.05	0.5

	Total Element Number	Total Node Number
Coarse mesh	36875	37296
Medium mesh	57619	58144
Fine mesh	80883	81480
Very fine mesh	105750	106424

Figure 5.6 Mesh settings for the hot bed validation studies.

The mesh size at the higher bed height is less critical because the gas-solid flow is not observed at upper bed heights. Hence, a bias factor is defined in the z direction of the cylindrical section of the bed. As a result, the grid size gets coarser at higher bed heights. The drag formulation of Syamlal O'Brien was also performed in mesh independence studies. The inlet velocity was selected as 1.0 U_{ms}, which is 25 m/s. In the simulation model, the Zehner-Schlunder approach was applied to evaluate the effective thermal conductivity of both phases. Moreover, other parameters of TFM are similar to those of the cold bed simulation's mesh independence studies.

The mesh independence studies were carried out in 20 s of real-time. The hydrodynamic results presented are the time-averaged values of the last 10 s of the simulations, with the data taken at 0.1 s intervals. The inlet gas phase temperature was set at room temperature, 24 °C. Meanwhile, the solid phase initial temperature was adjusted to 79 °C, and the wall boundary was determined as adiabatic.

In mesh independence studies, Figure 5.7a, Figure 5.7b, and Figure 5.7c demonstrate the radial distributions for the axial component of the gas velocity, the axial component of the particles velocity, and the solid volume fraction, respectively. Furthermore, their results were also evaluated at z = 50 mm. The radial variation of solid phase axial velocity and solid volume concentration of various mesh sizes are very close to each other. In contrast, gas phase axial velocities have slight differences in the spot region. The difference between fine and very fine meshes is less than 5% for gas velocity, which is deemed acceptable.

Furthermore, the bed pressure drops and the average particles temperatures at the end of 20 seconds were calculated for all four grid sizes. No significant differences in the pressure drop were observed. Additionally, the same computer sources, that are presented in Chapter 4, were used to perform all simulations. The computational times of mesh independence studies were calculated. Table 5.2 represents the results.

Table 5.2 Results of the average particles temperature and the pressure drops at the end of 20 s for the hot bed mesh independence study.

	The average particles temperature (°C) at end of 20 s	**Pressure Drop (Pa)**	**The Computational Times (h)**
Coarse Mesh	71.6	1465.3	~6.5
Medium Mesh	72.3	1461.4	~8
Fine Mesh	68.6	1473.3	~11
Very Fine Mesh	66.9	1480.2	~15

The experimental bed pressure drop was 1151 Pa and calculated pressure drop values using two different empirical correlations were 1435 Pa and 1439 Pa, respectively [75].

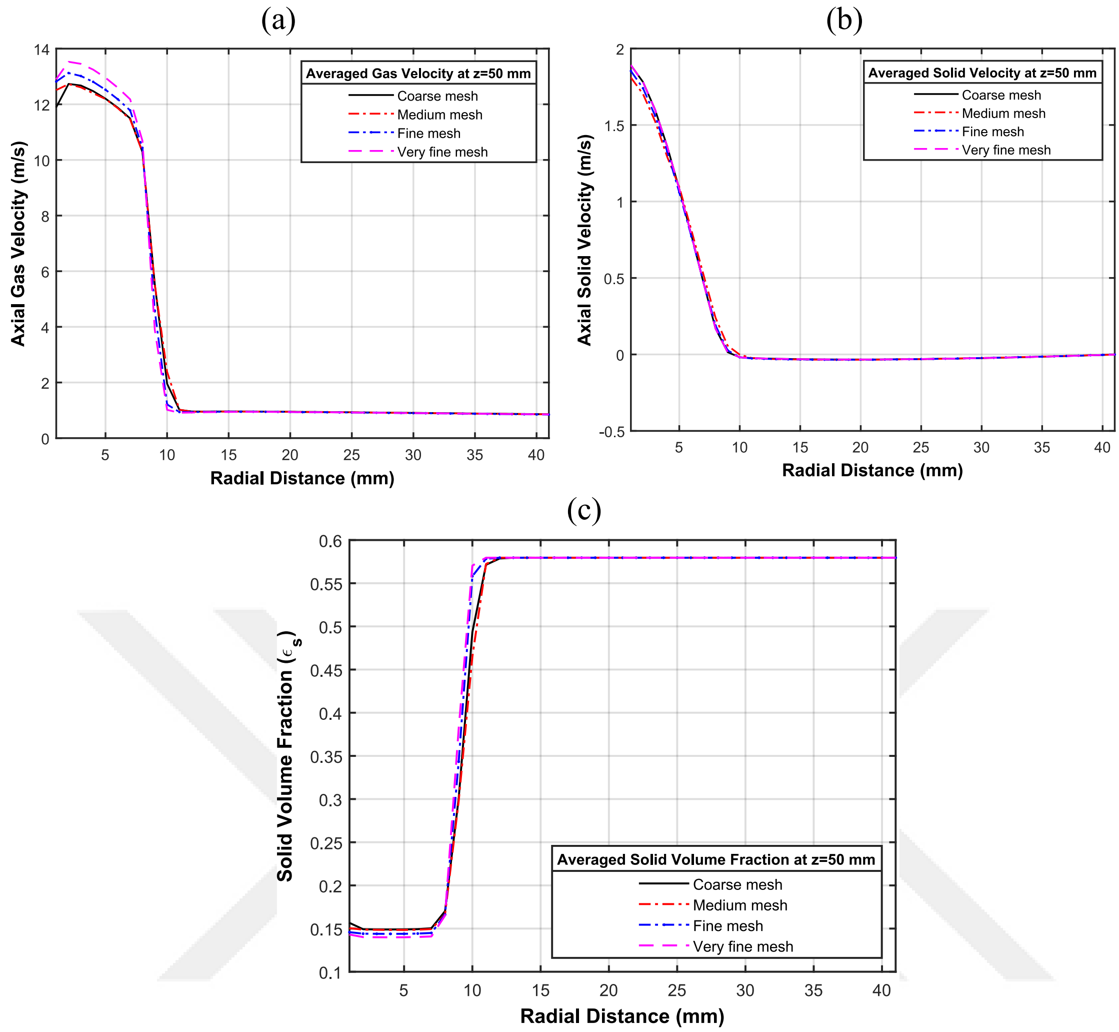

Figure 5.7 Comparison a) the axial part of the gas velocity, b) the axial part of the particles velocity, and c) the solid volume concentration for various mesh sizes.

Moreover, the discretized length in the mesh settings can affect the cooling performance. Suppose mesh independence is wholly provided for the energy equation. In that case, the dissimilar mesh settings must exhibit similar particle cooling performance, and the temperature difference among distinct mesh seizes must almost be zero. Thus, the temperature difference between all four mesh sizes was examined to identified mesh independence for the energy equations. Figure 5.8 represents the results belonging to the time-dependent average solid phase temperature distribution for four mesh sizes. After 10 seconds, the decrease rate of the temperature of the coarse mesh becomes almost zero. The results of the medium mesh also show a similar behavior. On the contrary, the temperature drops when fine and very fine meshes are used continue throughout the simulation. However, after 8 s, the temperature differences begin to be seen between the fine and the very fine mesh settings. The temperature difference is 1.7 °C at the end of the simulations. Hence, the full mesh independence is not observed for the energy equation. When the discretized length of the very fine mesh is further decreased, mesh independence can be possibly obtained for the energy equation. However, the fine and very fine mesh has approximately 81000 nodes and 106000 nodes, respectively. Meanwhile, the computer resource used for this thesis has difficulty even analysing these node numbers since the energy and momentum equations for both phases need to be solved together. Therefore, finer grid sizes were not examined in the mesh studies, and the fine mesh setting was used in the hot bed validation thermodynamic studies.

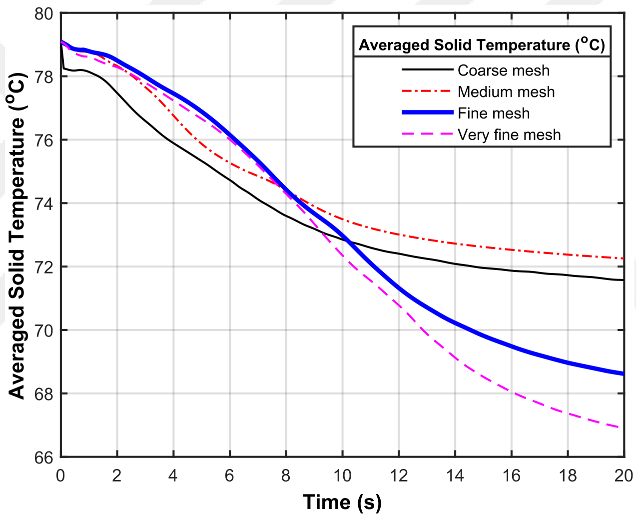

Figure 5.8 Time-dependent averaged solid phase temperature distributions for different mesh size of the hot bed.

5.4. Thermal Studies

In the spouted bed, the cooling response of the solid phase was investigated in this part. As indicated previously, Carbo HSP particles at a bed height of 100 mm were spouted at 1 U_{ms}. The following investigations were carried out:

- Comparing simulation results with Ozdemir's experimental results [75].
- Investigating the cooling behaviour of both phases in the annulus and spout region.
- Evaluating the effects of the Gunn's solid-gas phase interphase heat transfer correlation in the annulus and spout region.

- Evaluating the effects of Zehner-Schlunder's approach of modeling effective thermal conductivities of both phases in the spout and annulus region.

As a first step, the boundary, and initial conditions of the validation study in TFM approach were explained in detail. Furthermore, thermodynamic and hydrodynamic simulation settings of TFM were also given in detail. Then, the results of the hot spouted bed validation study were evaluated and compared with Ozdemir's experimental findings. After that, the results of the temperature distribution of both phases were investigated separately both the spout and annulus region

The findings from the validation studies of Patil's experiments (Chapter 4) are directly used and implemented in the hot spouted bed validation study. The heat transfer coefficient between gas-solid interphase was computed using the Gunn correlation. The Zehner-Schlunder approach was applied to obtain the effective thermal conductivity of both phases. Both Gunn's correlation and Zehner-Schlunder approach were satisfactory in Patil's study.

The internal wall temperature that was obtained in the experiments was directly defined in the simulation model as the wall boundary condition. Figure 5.9 represents the experimental time-dependent internal wall temperature for the discharging operation condition.

The carbo's true thermal conductivity, that is also described as the thermal conductivity of pure carbo material, and heat capacity were calculated for 70 °C by interpolation according tlo the values of Table 5.1. The true thermal conductivity and heat capacity values are 0.341 W/mK and 642 J/kg K, respectively. Furthermore, other parameters of TFM, defined in the mesh independence studies for the hot bed, are kept the same.

The modeling studies were performed in real time for 105 s. In the simulation, it is impossible to define the temperature distributions in the bed before the cooling part of the experiment. Therefore, for the first 5 seconds of the simulation, a uniform temperature of 79 °C was defined in the spouted bed because the stable spout takes 5 seconds to occur, which can affect the cooling process. At t = 5 s of the simulation, the inlet gas temperature was adjusted to 24 °C, whereas the internal wall temperature was adjusted based on the values of Figure 5.9. The thermal results are also presented after 5 seconds of the simulation.

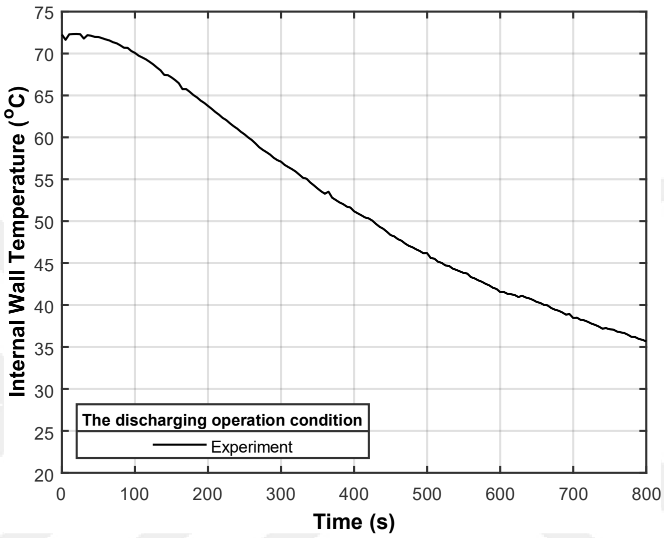

Figure 5.9 The variation of experimental internal wall temperature with time for the discharging operation condition [75].

Energy balance was also examined in the context of the thermal study. Figure 5.10 shows the system's heat loss variation related to time. The solid phase energy loss was observed to fluctuate with time and due to these fluctuations, the instantaneous energy balance is not observed. When the total energy balance is calculated for 100 s of the simulation, the difference between the energy loss of the wall and outlet and the solid phase energy change is about 19%. Not having achieved full mesh independence might be contributing to this discrepancy.

Moreover, the thermal simulation and the experimental data set results were compared. Figure 5.11 demonstrates the temperature distributions of the obtained from the simulations and experiments. As indicated before, three thermocouples were placed at the spout axis (z = 50 mm), in the annulus at the midpoint between the spout axis and the wall (z = 30 mm) and again in the annulus at the midpoint between the spout axis and the wall (z = 70 mm). It should be noted that the thermocouples in the bed contact both gas and solid phases while operating. Hence, they simultaneously measure the temperature of both phases, which is labeled as the mixture temperature is computed using volume fraction as the weighting parameter in the simulations (Equation 5.1) [75]:

$$T_m = \varepsilon_s T_s + (1 - \varepsilon_s) T_g \tag{5.1}$$

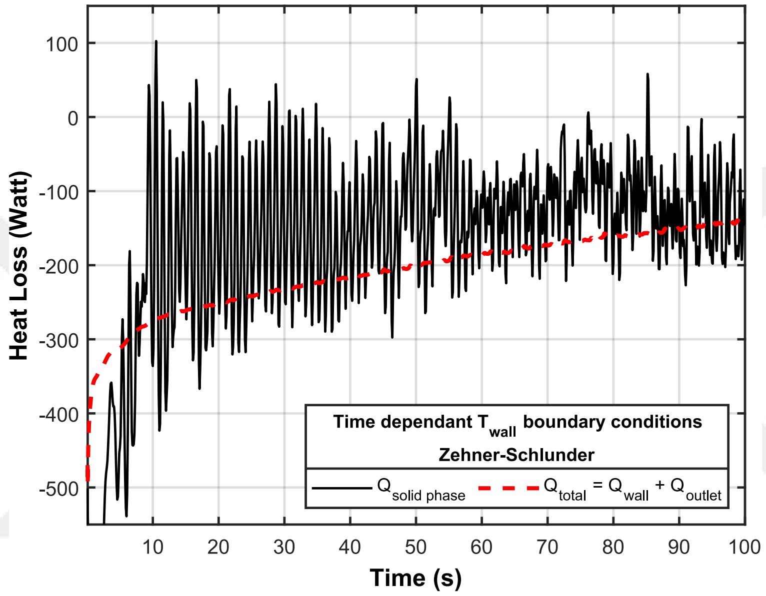

Figure 5.10 Heat losses of the system during discharging.

The solid volume fraction has a notable effect on the mixture temperature. As a result, in the annulus region, the solid phase temperature is more dominant than the gas phase in determining the mixture temperature. Meanwhile, in the spout region, the gas phase temperature is more dominant than the solid phase in determining the mixture temperature.

When Figure 5.11 is investigated, it seen that the simulations lead to a spout region which has a lower temperature than the annulus region similar to the experiments. The temperature variation between two measurement points in the annulus is larger in the experiments compared to simulations. The simulations result in more uniform temperature in the annulus. For the spout center measurement location (z = 50 mm), the difference in temperature values between the experimental and simulation results is about 5-6°C. Furthermore, the cooling rate is approximately 0.09 °C/s for 100 s, similar to the experimental results.

When annulus locations are considered, the largest discrepancy is for the z = 30 mm location close to 10 °C. In the upper zone of the annulus (z = 70 mm), simulation and experimental temperature difference is much smaller, around 4-5 °C. The simulated cooling rate at z = 30 mm is 0.16 °C/s, as well as at z = 70 mm is 0.18 °C/s for 100 s, respectively. On the other hand, the cooling rates obtained in the experiments at z = 30 mm is 0.11 °C/s, as well as at z = 70 mm is 0.15 °C/s. Differences in these cooling rates are a reason for increasing temperature differences between the experimental findings and simulation outcomes.

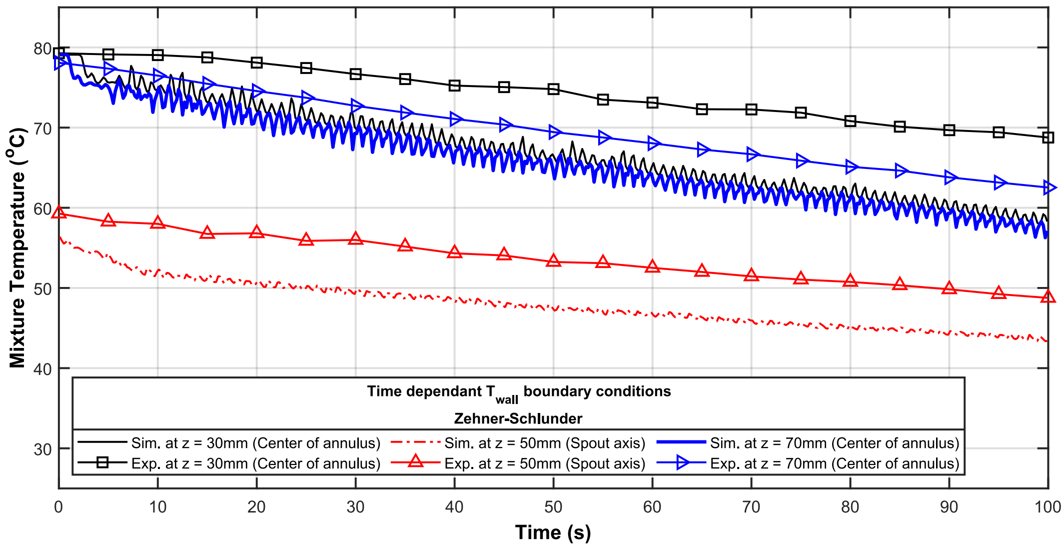

Figure 5.11 The variation of the mixture temperature at various bed heights with respect to time for the time dependent wall boundary conditions at 1.0 U_{ms}.

A massive proportion of the gas phase enters from the inlet to the spout region, whereas the remaining gas escapes to the annulus region. Therefore, in the spout and annulus regions, the temperature distribution of both phases with respect to time was evaluated to investigate the effects of the gas phase on the cooling of the solid phase. Figure 5.12 presents the results of the gas and particles temperatures at different heights: z = 30 mm, z = 50 mm, z = 70 mm, and z = 95 mm at the spout axis in the simulations. The temperature variation among both phases at z = 30 mm is approximately 24 ^{o}C at 10 s of the simulation. However, at the end of the simulation, the temperature difference is 16 ^{o}C resulting from the difference decreasing as colder particles enter the spout from the annulus as time passes. Similar trends at other heights can also be observed. Moreover, with the increasing height of the bed, the gas phase temperatures approach the solid phase, and they are equalized at z = 95 mm. As a result, in the spout region, the solid phase temperature decreases by approximately 2 ^{o}C, whereas the gas phase increases by approximately 20 ^{o}C throughout the simulation.

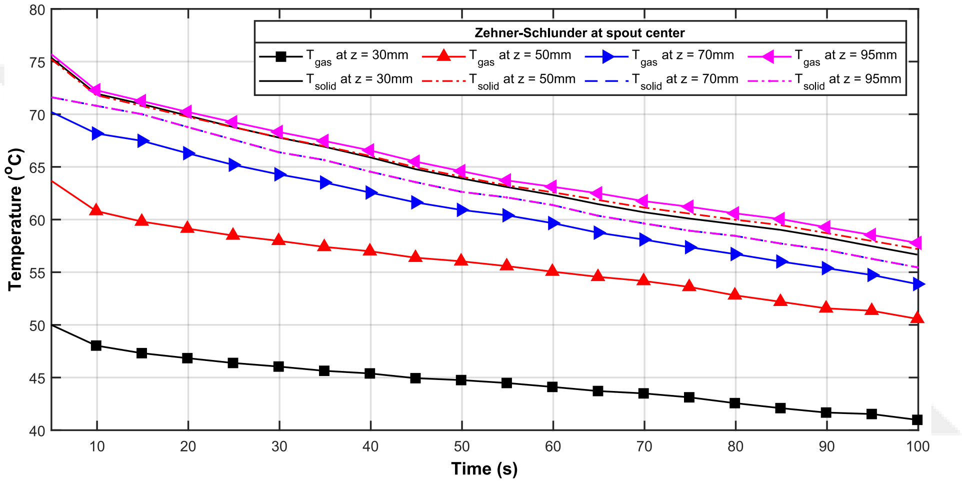

Figure 5.12 The variation of the temperature of the solid and gas phases temperature at the spout axis related to time at various bed heights for the time dependent wall boundary conditions at 1.0 U_{ms}.

Meanwhile, Figure 5.13 demonstrates the simulation outcomes of the solid and gas temperature in the annulus region at r = 15 mm for different heights; z = 30 mm, and z = 50 mm. Unlike the spout region, almost no temperature differences are observed in both phases. The main reasons are that only a small portion of the inlet gas enters the annulus, and the annulus region has a major solid volume fraction. Therefore, the gas phase does not have enough energy to cool the solid phase.

Figure 5.14a, Figure 5.14b, and Figure 5.14c present radial distributions of the mixture temperature with respect to different times at z = 30 mm, z = 50 mm, and z = 70 mm, respectively. At z = 30 mm, the difference of the temperature between the spout and annulus regions is approximately 40 °C at 10 s. At the end of the 90 s, this difference is approximately 25 °C. No significant difference in the mixture temperature is also observed to change over time in the spout region. Meanwhile, the mixture temperature decreases about 15 °C between 10 s and 90 s in the annulus region. Furthermore, similar temperature differences can also be detected at z = 50 mm and z = 70 mm for the annulus region. Additionally, the mixture temperature difference of the spout-annulus regions decreases when the bed height is increased.

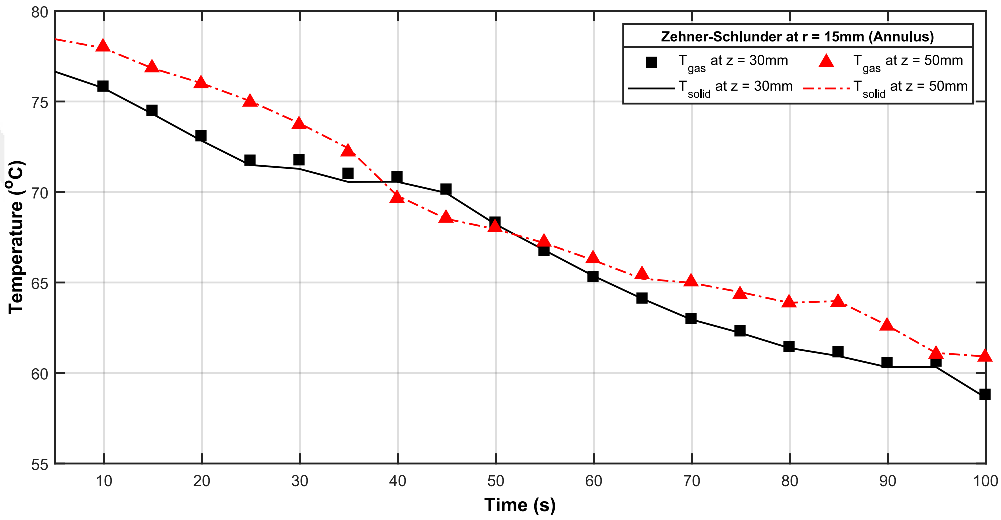

Figure 5.13 The variation of the temperature of the solid and gas phases at different bed heights in the annulus region (r = 15 mm) with respect to time for the time dependent wall boundary conditions at 1.0 U_{ms}.

Figure 5.15a presents the radial distribution of the heat transfer coefficient due to gas-solid interphase at z = 30 mm. These results presented are also the time-averaged values. Furthermore, the particle Reynolds and Nusselt numbers are given in Figure 5.15a. The interphase heat transfer coefficient indicates a profile similar with the axial part of gas velocity. Therefore, the peak heat transfer coefficient is almost 900 W/m^2K. As well as the highest particle Reynolds and Nusselt numbers are observed in the spout region. As presented in Figure 5.15b, a similar heat transfer coefficient for the spout region can also be seen at z = 50 mm and z = 70 mm. The interphase heat transfer coefficient decreases approximately by 20% in the spout region with an increase in bed height. On the other hand, in the annulus region, the lowest coefficient value of heat transfer is almost 200 W/m^2K because the axial gas velocity is observed to have the lowest value.

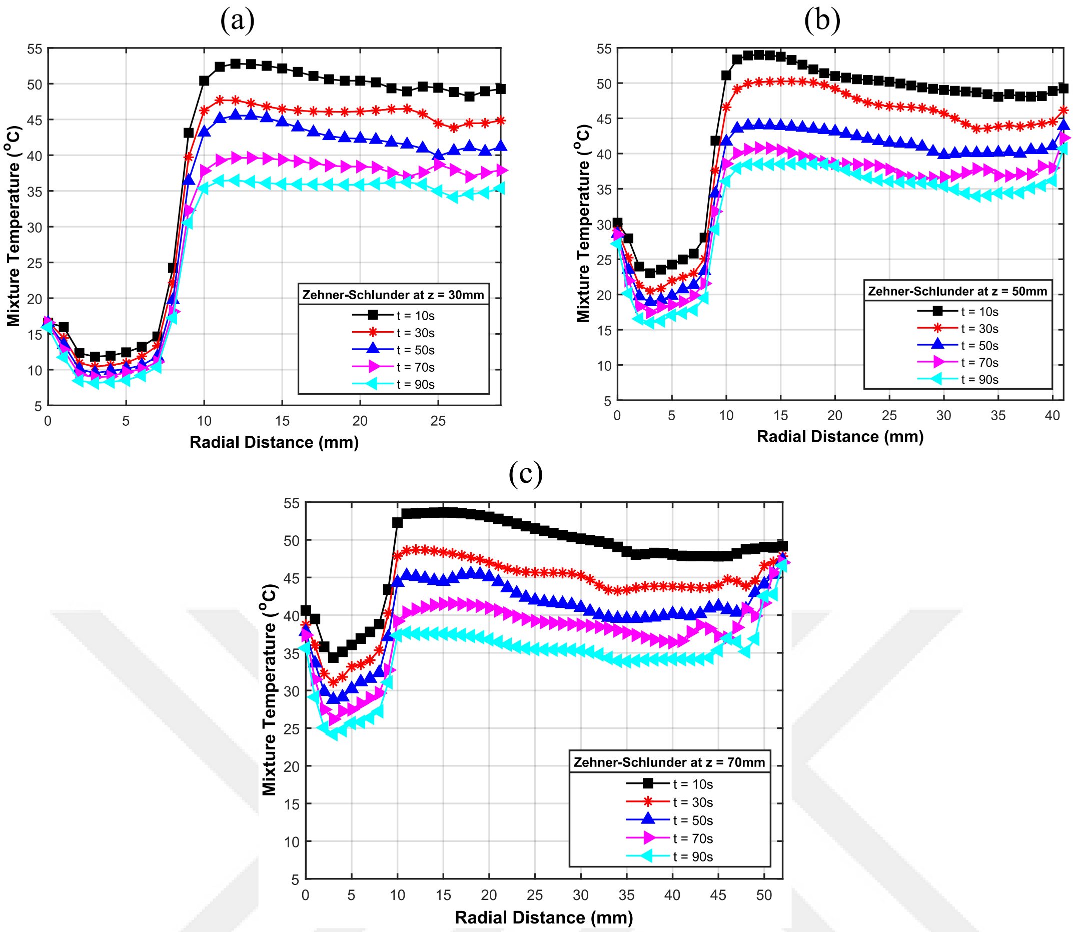

Figure 5.14 The radial variation of the mixture temperature at various times for the time dependent wall boundary conditions at 1.0 U_{ms} at a) z = 30 mm, b) z = 50 mm, and c) z = 70 mm.

According to these results, the particle cooling behavior starts in the spout region. Furthermore, the hot particles enter from the bottom of the annulus to the spout region laterally and move upward through the spout region as they contact cold gases that enter from the inlet. The particles lose energy, and their temperatures decrease until they reach the fountain region. The cooled particles fall through upper surface of the annulus, and they mix with the hot particles in the annulus. Therefore, the temperature cooling gradient in the annulus region is observed from the upper to the bottom parts of the annulus. On the other hand, the temperature cooling ratio is observed from the bottom to the upper parts of the spout in the spout region. The cooling gradients are seen in the contour images of the temperature distribution relating to the solid and gas phases at different times that are given in Figure 5.16 and Figure 5.17, respectively.

The radial distribution of the time-averaged effective solids phase thermal conductivity values obtained from Zehner-Schlunder's approach, and the true solid thermal conductivity are presented in Figure 5.18. The effective solid thermal conductivity obtained with Zehner-Schlunder's approach has no noticeable change with radial distance due to the difference in solid volume fraction between the spout and the annulus. Furthermore, it is almost half times the true value. On the other hand, it was almost one-fifth times the true value in Patil's validation study because the ratio between the true solid and the true gas thermal conductivity was higher four times than the hot spouted bed validation study.

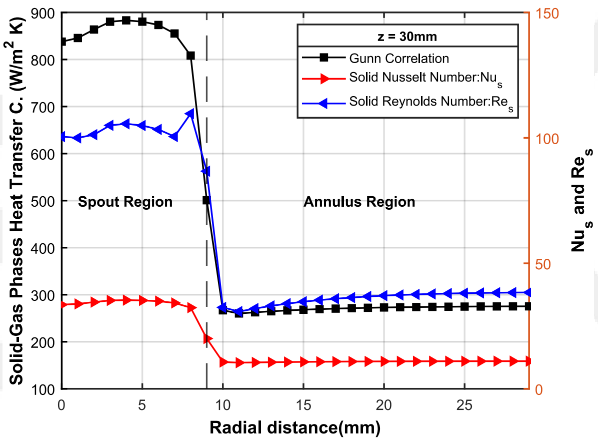

(a)

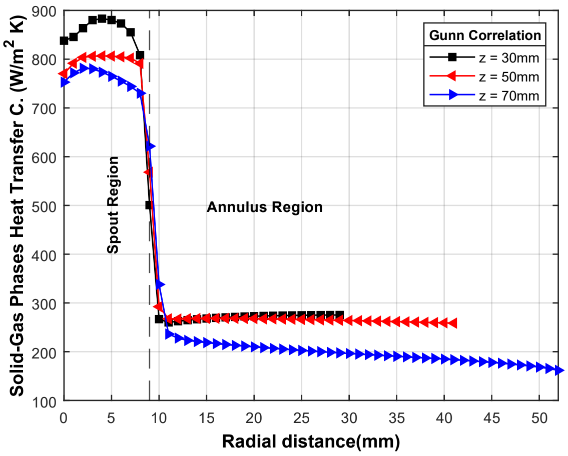

(b)

Figure 5.15 a)The radial variation of the time-averaged gas-solid interphase heat transfer, the particle Nusselt and Reynolds numbers at z= 30 mm, and b) the radial variation of the time-averaged gas-solid interphase heat transfer coefficient at different bed heights based on Gunn's correlation.

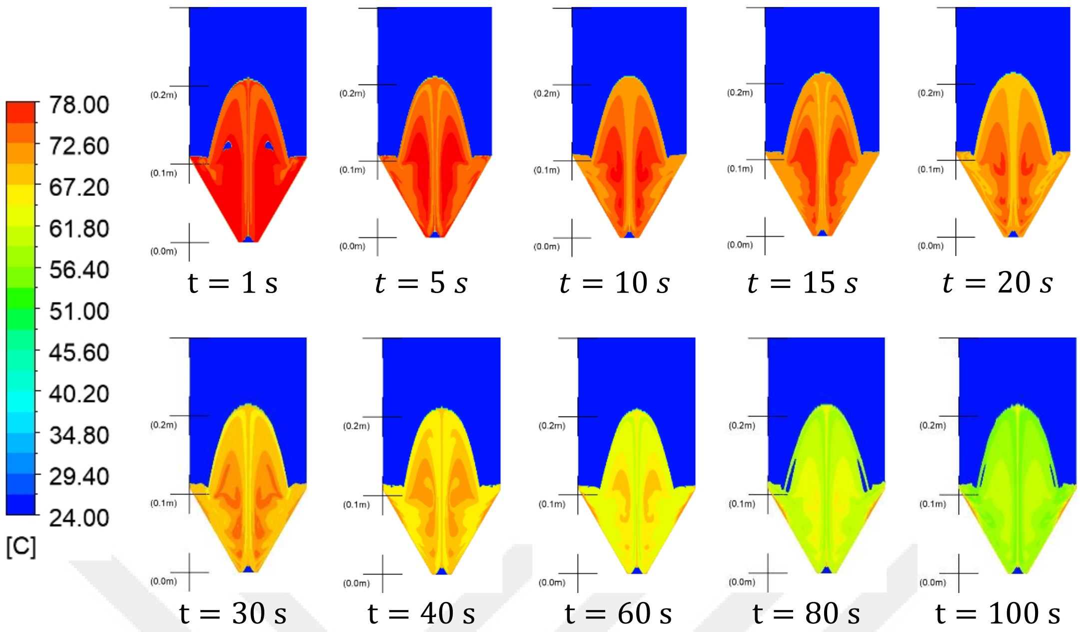

Figure 5.16 Contour images of the solid phase temperature distribution at different times.

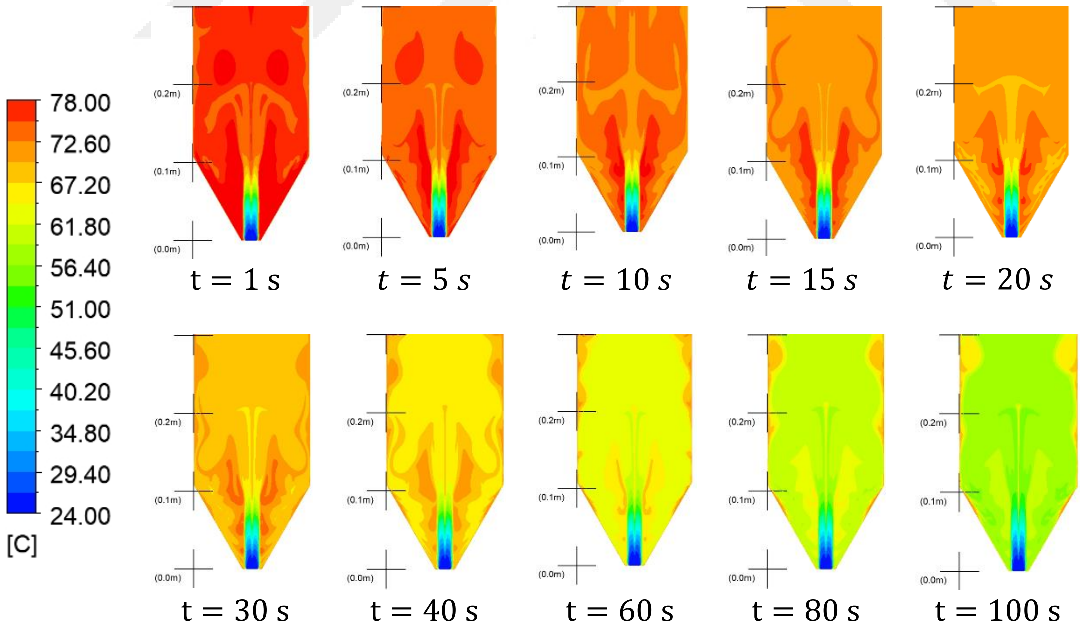

Figure 5.17 Contour images of the gas phase temperature distribution at different times.

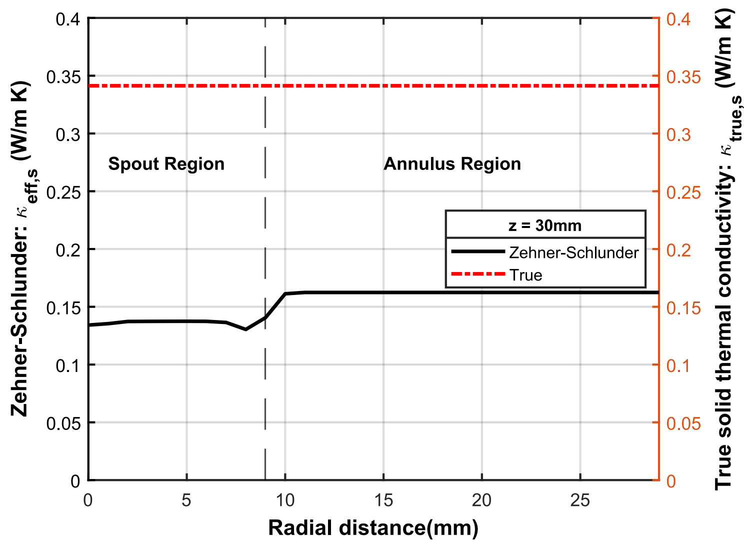

Figure 5.18 The radial variation of the time-averaged solid phase effective thermal conductivity at z=30 mm for Zehner-Schlunder's standard approach, and true value.

5.5. Conclusion for Hot Spouted Bed Validation Studies

The hot spouted bed validation study was modeled according to the outputs from the cold bed validation study (He *et al.*) and the hot bed fluidized bed study (Patil *et al.*). The interphase heat transfer coefficient was obtained according to the Gunn correlation. Furthermore, the effective thermal conductivities for both phases were calculated according to Zehner-Schlunder's approach. For the wall boundary conditions, experimentally measured internal wall temperatures were used. Furthermore, the drag model (Syamlal and O'Brien) and restitution coefficients in the cold bed verification study were kept the same for hot spouted bed study.

Before the cooling simulation of the hot spouted bed, a mesh independence study was completed. Mesh independence was achieved for the momentum equations; on the contrary, it could not be fully achieved for the energy equations. The number of elements in the simulation could be increased to obtain full mesh independence. However, the computer resource available could hardly afford to solve the simulation with larger element numbers.

After the mesh independence study, the hot spouted bed validation study was conducted for 100 seconds. The following results were obtained:

- The error in energy balance was lower than 19%, although the full mesh independence was not achieved for the energy equation.
- The ratio of cooling belonging to the mixture temperature in the spout region was consistent with the experimental data, and was approximately 0.09 °C/s for 100 s.
- In the annulus region, the ratio of cooling belonging to the mixture temperature was above the experimental result. The cooling rate at z = 30mm is 0.16 °C/s, and at z = 70 mm is 0.18 °C/s for 100 s. On the other hand, the cooling rates of the experiment at z = 30 mm is 0.11 °C/s, as well as at z = 70 mm is 0.15 °C/s.
- In the spout region, the solid particles were generally observed to cool.
- The cooling distribution of the solid phase in the annulus was found to be downward from top to bottom.
- The simulation's cooling gradient was similar to the experimental results in the annulus. However, the temperature differences were approximately 2 °C and less than the experimental results that were approximately 10 °C for 100 s.
- Based on the Gunn correlation, in the spout region, the interphase heat transfer coefficient was almost 900 W/m^2K. Therefore, the temperature differences among both phases were equivalent before exiting the spout region.

6. CONCLUSION

The particle receivers can be operated safely above 700 °C. Hence, they are recommended for integration into the next-generation concentrated solar power systems. Furthermore, directly irradiated fluidized/spouted particle receivers can store thermal energy at higher temperatures than 1100℃, and no other particle receivers can reach this temperature. So, the spouted/fluidized particle receivers are better candidates for the next-generation CSPs. Moreover, carbo and olivine particles have been suggested for particle receivers in CSP applications. They have high density and larger particle sizes, which suit them more suitably in a spouted bed than fluidized beds. So, experimental studies regarding laboratory-scale spouted beds have been gaining attention, and the results of these studies have been documented in open-access literatures.

On the other hand, the number of numerical modeling studies is still very limited in the literature. One commonly used modeling technique is the Eulerian-Eulerian approach (TFM). Most modeling studies using TFM are concentrated on either gas-solid flow dynamics or thermal aspects using a single experimental data set for comparison or validation. Furthermore, they present selective results of some best fitted parameters rather than investigating the effects of model parameters. A more comprehensive approach is required to investigate the performance of this modeling approach for the CSP application in spouted beds. Therefore, this thesis used three experimental data sets to assess the performance of the TFM approach for modelling CSP systems and research the impacts of heat transfer and gas-solid flow dynamics in detail for the ultimate aim of developing new CSP systems economically and effectively.

Notably, the particle volume fraction and axial velocity in the spout and annulus region, the bed's pressure drops, and the fountain height should be examined to fully understand the hydrodynamic behavior of a spouted bed. Therefore, in the spouted bed, He *et al.*'s data sets were selected as the first experimental data set and used to examine the comparative performance of the TFM approach for the gas-solid flow dynamics.

The following outcomes from the findings of the cold bed validation studies are given below:

- Among the drag models tested (Syamlal O'Brien, Wen-Yu and Gidaspow drag models), no external spout and fountain were observed when the Gidasow model was used. Gidaspow model could not produce satisfactory drag force at the given operating velocity. However, this finding is specific to He *et al*. data set and can not be generalized.
- Generally, Syamlal O'Brien drag model produced better predictions for the radial distribution belonging to the volume fraction of particle, the axial component of particle velocity and the spout diameter.
- A peculiar 'hook-like' shape was observed at the spout axis for the solids volume fraction, especially at higher bed heights. This shape was also observed in other TFM studies in the literature.
- One of the main inconsistent results of TFM is that the particle volume fraction is overestimated near the spout axis regardless of the drag model used. The problem is seen more clearly at the higher axial heights.
- The axial particle velocity and fountain height decrease with increasing coefficient of restitution.
- The wall specularity coefficient affects the particle velocities near the wall. However, it does not affect the overall gas-solid motion.

It should be noted that each spouted bed could have unique hydrodynamic characteristics, including different operating conditions, particle properties, inlet velocity, and spouted bed geometry. So, a hydrodynamic study is always required for each spouted bed before investigating thermal studies. Furthermore, amongst the restitution coefficient, the two fluid model parameters and the drag model are the most critical ones from hydrodynamics perspective to obtain reasonably accurate solutions.

Patil *et al*. experimentally investigated transient solid-phase cooling characteristics for a 2D pseudo-fluidized bed. They also provided an excessive data set about solid-phase cooling. Therefore, Patil *et al.*'s data sets were selected as the second experiment data set and used to understand how gas-solid interaction works and how material properties and boundary conditions affect thermal behavior in the solid phase.

The primary outcomes of the validation study of Patil's experiment are that calculating the heat transfer coefficient between gas-solid interphase, the effective thermal conductivity of solid phase, and the appropriate definition of the wall boundary conditions are essential to accurately modeling of the cooling or thermal energy discharge behavior of the bed. Therefore, the following suggestions are made based on Patil *et al.*'s. experimental data set:

- The hydrodynamic validations are critical before carrying out a thermal study.
- The overall energy balance must always be checked to ensure the reliability of the thermal simulations which are often overlooked in the literature.
- It is suggested that Zehner-Schlender's standard approach be used instead of kinetic approaches.
- Once the thickness and the material of the wall are known, a wall boundary condition with a fixed outer wall heat transfer coefficient (based on the ambient conditions) work fairly well.

Ozdemir [75] built an experimental setup that is a directly irradiated conical spouted bed receiver in the multiphase laboratory of Hacettepe University. They conducted different experiments with the setup using Carbo HSP and olivine particles. Therefore, in the spouted bed, Ozdemir’s data sets were selected as the third experiment data set and used to investigate the thermal energy discharge behavior.

Before the cooling study of the hot spouted bed, a mesh independence study was conducted. Mesh independence was achieved for the momentum equations; however, it could not be achieved fully for energy equation because the computer resource could hardly afford to solve the simulation with larger element numbers. However, the energy balance error did not exceed 19%, although the mesh independence was not fully achieved for energy equation. The hot spouted bed validation study was modeled according to the outputs from the cold bed validation study and the hot fluidized bed study.

The following outcomes of the validation study of Ozdemir's experiments are given below:

- The rate of cooling for the mixture temperature in the spout region was consistent with the experimental result.
- the cooling ratio of the mixture temperature was underestimated compared to the experimental result in the annulus region.
- In the spout region, the solid particles were generally observed to cool.
- The cooling distribution of the solid phase in the annulus was found to be downward from top to bottom.
- The simulation's cooling gradient was similar to the experimental results in the annulus. However, the temperature differences were underestimated compared to the experimental results.

Overall, the hot spouted bed validation study result could be coherently matched with the experimental data when the heat transfer coefficient due to gas-solid interphase was obtained with the Gunn correlation, and Zehner-Schlunder's approaches were applied to calculate the effective thermal conductivity. Overall, the Eulerian-Eulerian modeling can be be applied to the simulation of CSP thermal receivers with reasonable predictive capability.

The following items are suggested for investigation future work regarding TFM approach:

- The investigation of spouted/fluidized beds for charging operation using direct irradiation. For this study, the integration of radiation modelling needs to be studied.

- With more computational capacity, full mesh independence studies from thermal perspective can be carried out and energy balance can be evaluated.
- Effects of particle size can be investigated using Carbo and olivine particles.
- The different heating modeling techniques should be evaluated for charging the bed receiver. For example, the radiation model should be integrated for solar irradiation.

7. REFERENCES

[1] Y.-L. He, Y. Qiu, K. Wang, F. Yuan, W.-Q. Wang, M.-J. Li and J.-Q. Guo, "Perspective of concentrating solar power," *Energy,* vol. 198, p. 117373, 2020.

[2] "Champion Photovoltaic Module Efficiency Chart," National Renewable Energy Lab. (NREL), United States, 22 8 2024. [Online]. Available: https://www.nrel.gov/pv/module-efficiency.html. [Accessed 22 8 2024].

[3] IRENA, "Renewable capacity statistics 2023," International Renewable Energy Agency, Abu Dhabi, 2023a.

[4] J. Marti, A. Haselbacher and . A. Steinfeld, "A numerical investigation of gas-particle suspensions as heat transfer media for high-temperature concentrated solar power," *International Journal of Heat and Mass Transfer,* vol. 90, pp. 1056-1070, 2015.

[5] M. Mehos, C. Turchi, J. Vidal, M. Wagner, Z. Ma, C. Ho, W. Kolb, C. Andraka and A. Kruizenga, "Concentrating Solar Power Gen3 Demonstration Roadmap," National Renewable Energy Lab. (NREL), United States, 2017.

[6] W. Fuqiang, C. Ziming, T. Jianyu, Y. Yuan, S. Yong and L. Linhua, "Progress in concentrated solar power technology with parabolic trough collector system: A comprehensive review," vol. 79, no. , pp. 1314-1328, 2017.

[7] C. K. Ho, "Advances in central receivers for concentrating solar applications," *Solar Energy,* vol. 152, no. Concentrating Solar Power (CSP), pp. 38-56, 2017.

[8] A. Calderón, C. Barreneche, A. Palacios, M. Segarra, C. Prieto, A. Rodriguez-Sanchez and A. I. Fernández, "Review of solid particle materials for heat transfer fluid and thermal energy storage in solar thermal power plants," *Energy Storage,* vol. 1, no. 4, 2019.

[9] C. K. Ho, "A review of high-temperature particle receivers for concentrating solar power," *Applied Thermal Engineering,* vol. 109, pp. 958-969, 2016.

[10] C. Tregambi, M. Troiano, F. Montagnaro, R. Solimene and P. Salatino, "Fluidized Beds for Concentrated Solar Thermal Technologies—A Review," *Frontiers in Energy Research,* vol. 9, p. 618421, 2021.

[11] K. Jiang, X. Du, Y. Kong, C. Xu and X. Ju, "A comprehensive review on solid particle receivers of concentrated solar power," *Renewable and Sustainable Energy Reviews,* vol. 116, p. 109463, 2019.

[12] W. Wu, L. Amsbeck, R. Buck, N. Waibel, P. Langner and R. Pitz-Paal, "On the influence of rotation on thermal convection in a rotating cavity for solar receiver applications," *Applied Thermal Engineering,* vol. 70, pp. 694-704, 2014.

[13] T. Kodama, N. Gokon, H. S. Cho, K. Matsubara, T. Etori, A. Takeuchi, S.-n. Yokota and S. Ito, “Particles fluidized bed receiver/reactor with a beam-down solar concentrating optics: 30-kWth performance test using a big sun-simulator,” *AIP Conference Proceedings,* vol. 1734, no. 1, 2016.

[14] D. Kunii and O. Levenspiel, Fluidization Engineering, 2 ed., New York, NY: Wiley, 2005.

[15] P. Sahoo and A. Sahoo, “Fluidization and Spouting of Fine Particles: A Comparison,” *Advances in Materials Science and Engineering,* vol. 2013, pp. 369-380, 2013.

[16] N. Epstein and J. R. Grace, Spouted and Spout-Fluid Beds: Fundamentals and Applications, 1 ed., Cambridge University Press, 2011.

[17] Y. Yue, S. Wang and Y. Shen, “Spout deflection in spouted beds and countermeasures: A review,” *Powder Technology,* vol. 389, pp. 309-327, 2021.

[18] J. R. Grace, X. Bi and N. Ellis, Essentials of Fluidization Technology, Wiley-VCH, 2020.

[19] D. Góral, F. Kluza and K. Kozłowicz, “Spouted Bed and Jet Impingement Fluidization in Food Industry,” in *Heat Transfer - Models, Methods and Applications*, K. Volkov, Ed., IntechOpen, 2017.

[20] T. Kodama, N. Gokon, H. S. Cho, K. Matsubara, H. Kaneko, K. Senuma, S. Itoh and S.-n. Yokota, “Particles fluidized bed receiver/reactor tests with quartz sand particles using a 100-kWth beam-down solar concentrating system at Miyazaki,” *AIP Conference Proceedings,* vol. 1850, no. 1, p. 100012, 2017.

[21] C. Tregambi, R. Chirone, F. Montagnaro, P. Salatino and R. Solimene, “Heat transfer in directly irradiated fluidized beds,” *Solar Energy,* vol. 129, pp. 85-100, 2016.

[22] M. Díaz-Heras, J. Belmonte and J. Almendros-Ibáñez, “Experimental observations on directly irradiated conical spouted and spout-fluid beds,” *Experimental Thermal and Fluid Science,* vol. 130, p. 110488, 2022.

[23] M. Díaz-Heras, J. Moya, J. Belmonte, J. Córcoles-Tendero, A. Molina and J. Almendros-Ibáñez, “CSP on fluidized particles with a beam-down reflector: Comparative study of different fluidization technologies,” *Solar Energy,* vol. 200, pp. 76-88, 2020.

[24] H. Boujjat, S. Rodat, S. Chuayboon and S. Abanades, “Experimental and CFD investigation of inert bed materials effects in a high-temperature conical cavity-type reactor for continuous solar-driven steam gasification of biomass,” *Chemical Engineering Science,* vol. 228, p. 115970, 2020.

[25] Z. Ma, Y. Li, W. Zhang, Y. Wang, J. Zhao and Z. Wang, “Energy storage and attrition performance of limestone under fluidization during CaO/CaCO3 cycles,” *Energy,* vol. 207, p. 118291, 2020.

[26] Q. Bellouard, S. Abanades and S. Rodat, "Biomass Gasification in an Innovative Spouted-Bed Solar Reactor: Experimental Proof of Concept and Parametric Study," *Energy Fuels,* vol. 31, no. 10, pp. 10933-10945, 2017.

[27] S. Chuayboon and S. Abanades, "An overview of solar decarbonization processes, reacting oxide materials, and thermochemical reactors for hydrogen and syngas production," *International Journal of Hydrogen Energy,* vol. 45, no. 48, pp. 25783-25810, 2020.

[28] H. Boujjat, S. Rodat, S. Chuayboon and S. Abanades, "Numerical simulation of reactive gas-particle flow in a solar jet spouted bed reactor for continuous biomass gasification," *International Journal of Heat and Mass Transfer,* vol. 144, p. 118572, 2019.

[29] Q. Bellouard, S. Rodat, S. Abanades, S. Ravel and P.-É. Frayssines, "Design, simulation and experimental study of a directly-irradiated solar chemical reactor for hydrogen and syngas production from continuous solar-driven wood biomass gasification," *International Journal of Hydrogen Energy,* vol. 44, no. 35, pp. 19193-19205, 2019.

[30] K. Jiang, Q. Zhang, Y. Kong, C. Xu, X. Ju and X. Du, "Numerical Study of Parameters Effect on Thermo-flow Characteristics of up Bubbling Fluidized Bed Particle Solar Receiver," *ES Energy & Environment,* vol. 11, pp. 46-57, 2021.

[31] H. Benoit, R. Ansart, H. Neau, P. G. Triñanes, G. Flamant and O. Simonin, "Three-dimensional numerical simulation of upflow bubbling fluidized bed in opaque tube under high flux solar heating," *AIChE J,* vol. 64, no. 11, pp. 3857-3867, 2018.

[32] G. Baud, J. Bezian, M. El Hafi and G. Olalde, "A theoretical and experimental study of the time-dependent radiative properties of a solar bubbling fluidized bed receiver," *Solar Energy,* vol. 105, pp. 341-353, 2014.

[33] k. Matsubara, Y. Kazuma, A. Sakurai, T. Kodama, N. Gokon, H.-S. Cho and K. Yoshida, "Laboratory Experiment and Simulation of High-temperature Fluidized Bed Air Receiver for Concentrated Solar Power Generation," *Journal of the Japan Institute of Energy,* vol. 94, no. 11, pp. 1323-1329, 2015.

[34] J. Shen, X. Liu and W. H. Ho, "CFD simulation of a fluidized bed as a solar receiver," *AIP Conference Proceedings,* Vols. 0094-243X, no. 1, p. 030055, 2019.

[35] T. Tsuji, M. Miyauchi, S. Oh and T. Tanaka, "Simultaneous Measurement of Particle Motion and Temperature in Two-Dimensional Fluidized Bed with Heat Transfer," *KONA Powder and Particle Journal,* vol. 28, pp. 167-179, 2010.

[36] S. L. Brown, "Hydrodynamics and Transient Heat Transfer Characteristics," Master degree ,The Virginia Polytechnic Institute and State University, Virginia, 2012.

[37] M. Fattahi, S. H. Hosseini and G. Ahmadi, "CFD simulation of transient gas to particle heat transfer for fluidized and spouted regimes," *Applied Thermal Engineering,* vol. 105, pp. 385-396, 2016.

[38] S. H. Hosseini, M. Fattahi and G. Ahmadi, “CFD Study of hydrodynamic and heat transfer in a 2D spouted bed: Assessment of radial distribution function,” *Journal of the Taiwan Institute of Chemical Engineers,* vol. 58, pp. 107-116, 2016.

[39] A. Patil, E. Peters and J. Kuipers, “Comparison of CFD–DEM heat transfer simulations with infrared/visual measurements,” *Chemical Engineering Journal,* vol. 277, pp. 388-401, 2015.

[40] W. Du, X. Bao, J. Xu and W. Wei, “Computational fluid dynamics (CFD) modeling of spouted bed: Assessment of drag coefficient correlations,” *Chemical Engineering Science,* pp. 1401-1420, 2006a.

[41] M. Syamlal and T. J. O’Brien, “Computer Simulation of Bubbles in a Fluidized Bed,” *AIChE Symp. Series,* vol. 85, pp. 22-31, 1989.

[42] M. S. Alagha and P. Szentannai, “Analytical review of fluid-dynamic and thermal modeling aspects of fluidized beds for energy conversion devices,” *International Journal of Heat and Mass Transfer,* vol. 147, p. 118907, 2020.

[43] S. Ergun, “Fluid Flow through Packed Columns,” *Chem. Eng. Prog.,* vol. 48, no. 2, p. 1952, 89-94.

[44] S. Senturk-Lule, “Computational fluid dynamics studies for a spouted bed nuclear fuel coater,” PhD thesis, Hacettepe University, Ankara, 2012.

[45] C.-Y. Wen and Y. H. Yu, “Mechanics of Fluidization,” *Chem. Eng. Prog. Symp. Series.,* vol. 62, pp. 100-111, 1966.

[46] Ansys, Ansys Fluent Theory Guide 2022 R2, 2022.

[47] D. Gidaspow and J. Ding, “A Bubbling Fluidization Model Using Kinetic Theory of Granular Flow,” *AIChE J.,* vol. 36, no. 4, p. 523–538, 1990.

[48] S. H. Hosseini, G. Ahmadi and M. Olazar, “CFD simulation of cylindrical spouted beds by the kinetic theory of granular flow,” *Powder Technology,* vol. 246, pp. 303-316, 2013.

[49] K. K. Lun, S. B. Savage, D. J. Jeffrey and N. Chepurniy, “Kinetic Theories for Granular Flow: In-elastic Particles in Couette Flow and Slightly Inelastic Particles in a General Flow Field,” *J. Fluid Mech.,* vol. 140, p. 223–256, 1984.

[50] W. Du, X. Bao, J. Xu and W. Wei, “Computational fluid dynamics (CFD) modeling of spouted bed: Influence of frictional stress, maximum packing limit and coefficient of restitution of particles,” *Chemical Engineering Science,* vol. 61, no. 14, pp. 4558-4570, 2006b.

[51] M. Syamlal, W. Rogers and T. J. O’Brien, “MFIX Documentation: Volume1,” National Technical Information Service, Springfield, 1993.

[52] D. Gidaspow, R. Bezburuah and J. Ding, “Hydrodynamics of Circulating Fluidized Beds, Kinetic,” *In Fluidization VII, Proceedings of the 7th Engineering Foundation Conference,* p. 75–82, 1992.

[53] D. G. Schaeffer, "Particle velocity profiles and solid flow patterns in spouted beds," *The Canadian Journal of Chemical Engineering,* vol. 72, no. 4, pp. 561-568, 1994.

[54] M. Syamlal and D. Gidaspow, "Hydrodynamics of fluidization: Prediction of wall to bed heat transfer coefficients," *AIChE Journal,* vol. 32, no. 1, pp. 127-135, 1985.

[55] J. A. M. Kuipers, W. Prins and W. P. M. Van Swaaij, "Numerical calculation of wall-to-bed heat-transfer coefficients in gas-fluidized beds," *AIChE Journal,* vol. 38, no. 7, pp. 1079-1091, 1992.

[56] A. Schmidt and U. Renz, "Eulerian computation of heat transfer in fluidized beds," *Chemical Engineering Science,* vol. 54, no. 22, pp. 5515-5522, 1999.

[57] A. Schmidt and U. Renz, "Numerical prediction of heat transfer in fluidized beds by a kinetic theory of granular flows," *International Journal of Thermal Sciences,* vol. 39, no. 9, pp. 871-885, 2000.

[58] D. J. Patil, J. Smit, M. van Sint Annaland and J. A. M. Kuipers, "Wall-to-bed heat transfer in gas–solid bubbling fluidized beds," *AIChE Journal,* vol. 52, no. 1, pp. 58-74, 2006.

[59] L. Armstrong, S. Gu and K. Luo, "Study of wall-to-bed heat transfer in a bubbling fluidised bed using the kinetic theory of granular flow," *International Journal of Heat and Mass Transfer,* vol. 53, no. 21, pp. 4949-4959, 2010.

[60] R. Yusuf, B. Halvorsen and M. C. Melaaen, "Eulerian–Eulerian simulation of heat transfer between a gas–solid fluidized bed and an immersed tube-bank with horizontal tubes," *Chemical Engineering Science,* vol. 66, no. 8, pp. 1550-1564, 2011.

[61] P. Zehner and E. Schlunder, "Thermal conductivity of packings at moderate temperatures," *Chemie Ingenieur Technik,* vol. 42, no. 14, p. 933, 1970.

[62] D. J. Gunn, "Transfer of heat or mass to particles in fixed and fluidised beds," *Int J Heat Mass Transfer,* vol. 21, no. 4, pp. 467-476, 1978.

[63] Y.-L. He, C. J. Lim, J. R. Grace and S.-Z. Zhu, "Measurements of voidage profiles in spouted beds," *The Canadian Journal of Chemical Engineering,* vol. 72, no. 2, pp. 229-234, 1994a.

[64] Y.-L. He, S.-Z. Qin, C. J. Lim and J. R. Grace, "Particle velocity profiles and solid flow patterns in spouted beds," *The Canadian Journal of Chemical Engineering,* vol. 72, no. 4, pp. 561-568, 1994b.

[65] Z. Wang, "Experimental studies and CFD simulations of conical spouted bed hydrodynamics," PhD thesis, University of British Columbia, Vancouver, 2006.

[66] W. Zhonghua and A. S. Mujumdar, "Simulation of the Hydrodynamics and Drying in a Spouted Bed Dryer," *Drying Technology,* vol. 25, no. 1, pp. 59-74, 2007.

[67] W. Zhonghua and A. S. Mujumdar, "CFD modeling of the gas–particle flow behavior in spouted beds," *Powder Technology,* vol. 183, no. 2, pp. 260-272, 2008.

[68] R. Béttega, R. Corrêa and J. Freire, “Scale-up study of spouted beds using computational fluid dynamics,” *The Canadian Journal of Chemical Engineering,* vol. 87, pp. 193-203, 2009.

[69] X. Lan, C. Xu, J. Gao and M. Al-Dahhan, “Influence of solid-phase wall boundary condition on CFD simulation of spouted beds,” *Chemical Engineering Science,* vol. 69, no. 1, pp. 419-430, 2012.

[70] M. O. Reza, A. Laugwitz and P. Nikrityuk, “Cylindrical-conical spouted bed dynamics: Laminar and turbulent flow predictions,” *The Canadian Journal of Chemical Engineering,* vol. 95, no. 4, pp. 783-795, 2017.

[71] F. Wu, C. Yang, X. Che, X. Ma, Y. Yan and W. Zhou, “Numerical and experimental study of integral multi-jet structure impact on gas-solid flow in a 3D spout-fluidized bed,” *Chemical Engineering Journal,* vol. 393, p. 124737, 2020.

[72] H. Shi, M. O. Reza and P. A. Nikrityuk, “The impact of swirling on the dynamics of a spouted bed,” *Powder Technology,* vol. 380, pp. 143-151, 2021.

[73] P. Wang and Y. Li, “Numerical investigation of flow, heat transfer characteristics and structure improvement in a fluidized bed solar particle receiver,” *International Journal of Thermal Sciences,* vol. 205, pp. 109294,, 2024.

[74] L. Hao, W. Xiaobao, W. Xiaoqin, N. Lukasz, P.-K. Halina, L. Xinyan and X. Qingang, “Multi-fluid modeling of heat transfer in bubbling fluidized bed with thermally-thick particles featuring intra-particle temperature inhomogeneity,” *Chemical Engineering Journal,* vol. 460, p. 141813, 2023.

[75] A. E. Özdemir, “Experimental and Numerical Investigation of Spouted Bed Solar Receivers,” M.S. thesis, Hacettepe University, Ankara, 2024.

[76] A. E. Özdemir, G. Külah and M. Köksal, “CFD-DEM Modelling of Conical Spouted Bed Solar Thermal,” in *14th International Conference on Fluidized Bed Technology (CFB-14)*, Taiyuan, 2024.

[77] A. E. Özdemir, C. Akıcı, M. Köksal and G. Külah, “Experimental Investigation of Conical Spouted Bed Themal Solar Recievers,” in *14th International Conference on Fluidized Bed Technology (CFB-14)*, Taiyuan, 2024.

APPENDICES

Appendix-1. Ansys Fluent User Defined Function (UDF)

```
/* UDF file must have .c extension*/

/*This UDF can be used only in the simulation model of Chapter 4. If it is applied in different models,
material properties in the model must be control or change. */

#include "udf.h"

/* The true fluid thermal conductivity,it is related to the gas phase */

#define K_f_o 0.025

/* The true solid thermal conductivity,it is related to the solid phase */

#define K_s_o 1.4

/* The ratio of the particle contact area to the total particle surface area */

#define w 0.00726

/* Fluid phase effective thermal conductivity calculation according to Zehner-Schlunder approach */

DEFINE_PROPERTY(thermal_fluid_bulk_eff, c, t)

{

	real e_fluid;

	real K_b_f;

	real K_b_f_eff;

/*Calling value of fluid volume fraction  at cell center */

	e_fluid = C_VOF(c, t);

/*Note that comment of  C_VOF calls only related material property in GUI. For exmaple, if this UDF is
selected in solid phase section, it calls solid phase volume fraction. */

/*Calculation of bulk fluid thermal conductiviy according to Zehner-Schlunder approach */

	K_b_f = (1. - pow(1. - e_fluid, 0.5)) * K_f_o;

/*Calculation of effective fluid thermal conductiviy according to  bulk fluid thermal conductiviy */

K_b_f_eff = K_b_f / e_fluid;

/*Each  is calculated separately*/

	return K_b_f_eff;

}

/* Solid phase effective thermal conductivity calculation according to Zehner-Schlunder approach*/

DEFINE_PROPERTY(thermal_solid_bulk_eff, c, t)

{
```

```
        real e_fluid;
        real e_solid;
        real K_b_s;
        real K_b_s_eff;
        real A;
        real B;
/*The first term of GAMMA equation according to Zehner-Schlunder approach*/
        real R_1;
/*The second term of GAMMA equation according to Zehner-Schlunder approach*/
        real R_2;
/*The third term of GAMMA equation according to Zehner-Schlunder approach*/
        real R_3;
/*The forth term of GAMMA equation according to Zehner-Schlunder approach*/
        real R_4;
/*The full GAMMA equation according to Zehner-Schlunder approach*/
        real R;
/* Calling value of solid volume fraction at cell center*/
        e_solid = C_VOF(c, t);
        e_fluid = 1 - e_solid;
/* In Ansys Fluent, volume fraction is not equalt to 0. So, it must be defined a too small number*/
        if (e_solid < 0.01)
        {
                K_b_s_eff = 0.001;
        }
        else if (e_solid > 0.01)
        {
                A = K_s_o / K_f_o;
                B = 1.25 * pow(((1. - e_fluid) / e_fluid), (10.0 / 9.0));
                R_1 = 2.0 / (1 - (B / A));
                R_2 = (A - 1) * B * (double)log((double)(A / B)) / A / pow((1 - (B / A)), 2.0);
                R_3 = (B - 1) / (1 - (B / A));
                R_4 = (B + 1) / 2;
                R = R_1 * (R_2 - R_3 - R_4);
/*Calculation of bulk solid thermal conductiviy according to Zehner-Schlunder approach */
                K_b_s = pow(1. - e_fluid, 0.5) * (w * A + (1 - w) * R) * K_f_o;
/*Calculation of effective solid thermal conductiviy according to  bulk solid thermal conductiviy */
```

```
            K_b_s_eff = K_b_s / e_solid;
        }
        return K_b_s_eff;
}

/* Solid phase effective thermal conductivity calculation according to Hunt approach*/
DEFINE_PROPERTY(kinetic_theory_hunt, c, t)
{
        real granular_temp;
        real e_solid;
        real radial_distribution_function;
        real K_b_s;
        real K_b_s_eff;
        real d_solid = 0.001;
        real cp_solid = 840;
        real density_solid = 2500;
/* Calling value of granular temperature  at cell center*/
        granular_temp = C_GT(c, t);
/* Calling value of solid volume fraction  at cell center*/
        e_solid = C_VOF(c, t) ;
        radial_distribution_function = (16.0 - 7.0 * e_solid) / pow((1 - e_solid), 2.0) / 16.0;
/*Calculation of effective solid thermal conductiviy according to  Hunt approach*/
        K_b_s_eff = 5.56832 * pow(granular_temp, 0.5) / 32 / radial_distribution_function * density_solid
* cp_solid * d_solid;
        return K_b_s_eff;
}
}

/* Gunn correlation for gas-solid interphase heat transfer*/
#include "udf.h")
DEFINE_EXCHANGE_PROPERTY(heat_gunn, c, t, i, j)
{
/* Defined gas phase (first phase in Fluent)*/
        Thread* ti = THREAD_SUB_THREAD(t, i);
/* Defined solid phase (Second phase in Fluent)*/
        Thread* tj = THREAD_SUB_THREAD(t, j);
```

```
    real h;
    real NV_VEC(v), vel, Re, Pr, Nu;
/* Calculation of velocity differences between the gas and solid phases for each direction.*/
    NV_DD(v, =, C_U(c, tj), C_V(c, tj), C_W(c, tj), -, C_U(c, ti), C_V(c, ti), C_W(c, ti));
/* Calculation of absolute velocity differences between the gas and solid phases for each direction.*/
    vel = NV_MAG(v);
/* Calculation of Reynold number*/
    Re = C_VOF(c, ti) * 1.225 * vel * 0.001 / 0.00002;
/* Calculation Prandtl number*/
    Pr = 840 * 0.00002 / 0.025;
/* Calculation Particle Nusselt number*/
    Nu = (7 - 10 * C_VOF(c, ti) + 5 * pow(C_VOF(c, ti), 2. / 1.)) * (1 + 0.7 * pow(Re, 2. / 10.) *
pow(Pr, 1. / 3.)) + (1.33 - 2.4 * C_VOF(c, ti) + 1.2 * pow(C_VOF(c, ti), 2. / 1.)) * pow(Re, 7. / 10.) *
pow(Pr, 1. / 3.);
/* heat transfer coefficient due to solid - gas interaction*/
    h = 0.025 * Nu / 0.001;
    return h;
}
```